Medical imaging with a laser–driven undulator x–ray source

Monte Carlo simulation of the image formation and dose deposition in mammography

Bernhard H. Müller

München 2012

Medical imaging with a laser–driven undulator x–ray source

Monte Carlo simulation of the image formation and dose deposition in mammography

Bernhard H. Müller

Dissertation
an der Fakultät für Physik
der Ludwig–Maximilians–Universität
München

vorgelegt von
Bernhard H. Müller
aus Erlangen

München, den 9.11.2012

Erstgutachter: Prof. Dr. Florian Grüner
Zweitgutachter: Prof. Dr. Christoph Hoeschen
Tag der mündlichen Prüfung: 18.2.2013

Zusammenfassung

Die Entwicklung von kompakten, auf der Laser-Plasma-Beschleunigung von Elektronen basierenden, lasergetriebenen Röntgenquellen erlauben es energieverstimmbare Röntgenstrahlung zu erzeugen und haben das Potential in der medizinischen Bildgebung Anwendung zu finden. Die durch diese Quellen erzeugte Röntgenstrahlung bietet eine Reihe von Vorteilen in diesem Bereich gegenüber der durch Röntgenröhren erzeugten Strahlung. Der Hauptvorteil ist das energieverstimmbare, nahezu monochromatische Spektrum, das es erlaubt für die jeweilige Anwendung in der Bildgebung die optimale Energie der Röntgenstrahlung auszuwählen. Zusammen mit der Eigenschaft der Fokussierbarkeit des Strahls und der geringen Divergenz bietet sich damit die Möglichkeit in der Röntgenabsorptionsbildgebung eine signifikant höheres Bildqualität-zu-Dosis Verhältnis zu erreichen im Vergleich zu polychromatischen Röntgenröhren.

Das Ziel dieser Arbeit ist es die Anwendung dieser neuen Röntgenquellen in der medizinischen Bildgebung zu untersuchen und deren Leistungsfähigkeit mit der von Röntgenröhren zu vergleichen. Der Fokus liegt dabei in dieser Arbeit auf der Mammographie, da mit steigender verfügbarer Leistung des treibenden Lasers und damit steigender Energie der Röntgenstrahlung dies eine der ersten möglichen Anwendungn wäre. Nachdem derzeit die durch diese lasergetriebenen Röntgenquellen erreichte Energie noch nicht die Schwelle der weichen Röntgenstrahlung überschreitet, basieren die Untersuchungen in dieser Arbeit auf der Berechnung der Erzeugung der Röntgenstrahlung und auf Simulationsrechnungen des Bild- und Dosisentstehungsprozesses um zu quantitativen Ergebnissen zu gelangen.

Die Berechnung der Dynamik der laserbeschleunigten Elektronen und die darauf aufbauende Berechnung der Erzeugung von, auf die Anwendung in der medizinischen Bildgebung optimierten Röntgenstrahlung, zeigt, dass es möglich ist, einen dafür geeigneten quasi-monochromatischen, laminaren Strahl mit niedriger Divergenz zu erzeugen. Die erforderlichen Parameter der Röntgenquelle die zu einem laminaren Strahl führen, der für eine Abtastgeometrie geeignet ist, werden bestimmt und der Einfluss dieser Parameter auf die Strahleigenschaften wird diskutiert. Um eine möglichst realistische Simulation der Mammographie zu erstellen wurden zwei anatomische Präparate der weiblichen Brust in einem hochauflösenden CT aufgenommen und aus den dadurch erzeugten Daten mehrere Voxelmodelle erstellt, die die in der Brust vorkommenden charakteristischen Gewebestrukturen enthalten. Basierend auf den Berechnungen der Röntgenstrahlung und den erstellten Voxelmodellen der Brust wurde eine Monte Carlo Simulation der Absorptions- und Streuprozesse erstellt um die Möglichkeit von Mammographieaufnahmen mit einer lasergetriebenen Röntgenquelle möglichst genau zu untersuchen. Diese Simulation berücksichtigt alle relevanten Eigenschaften der Röntgen-

quelle wie die spektrale Winkelverteilung und die Quellgröße der Röntgenstrahlung und stellt ein Modell der Bildgebung mit einer streustrahlungsreduzierenden Abtastgeometrie dar. Unter Verwendung dieser Simulation wird gezeigt, dass die für eine bestimmte Bildqualität erforderliche Strahlendosis in der Mammographie im Vergleich zu der mit Röntgenröhren erforderlichen Strahlendosis signifikant reduziert werden kann und die Abhängikeit dieser Dosisreduktion von den relevanten Parametern der lasergetriebenen Röntgenquelle wird quantifiziert. Darüber hinaus wird auch ein einfaches analytisches Modell der Abhängigkeit des Bildqualität-zu-Dosis Verhältnisses von der Energie der Röntgenstrahlung vorgestellt, um die Simulationsrechnungen zu interpretieren. Die in dieser Arbeit mit Bezug auf die Anwendung in der Mammographie erstellten Methoden und Simulationswerkzeuge bieten außerdem eine Basis für die Untersuchung weitergehender Bildgebungstechniken, die durch lasergetriebene Röntgenquellen erst ermöglicht werden.

Summary

In recent years table-top sized laser-driven x-ray sources based on a laser-plasma acceleration scheme have been developed that allow the generation of tunable quasi-monochromatic x-rays and have the potential to produce a beam profile suitable for medical imaging applications. The radiation produced by these sources has a number of advantages over the radiation produced by conventional x-ray tubes. The main advantage is the tunable nearly monochromatic x-ray spectrum that allows the selection of the optimal x-ray energy depending on the imaging setting. Together with the focusable low divergent beam this provides the opportunity to achieve a significantly higher image quality per dose in x-ray imaging when compared to polychromatic x-ray sources.

The aim of this work is to investigate the application of this type of x-ray source to medical imaging and to compare its performance to that of conventional x-ray tubes. The focus here lies on mammography as one of the first feasible imaging modalities, as the lower energetic x-rays would be the first to be achieved with increasing laser power. As currently the output of this type of laser-based x-ray source still not exceeds the soft x-ray energy range this work relies on the calculation of the x-ray production and subsequently on the simulation of the image formation process in order to obtain a quantitative analysis. Together with that also an analytical model of the relationship between the image-quality-to-dose ratio and the x-ray energy is developed. The calculation of the dynamics of the laser-accelerated electrons and the subsequent calculation of the x-ray production in the context of an x-ray imaging setup shows that it is possible to create a quasi-monochromatic, low-divergent, laminar beam suitable for medical imaging applications. The specific source parameters needed for the creation of a laminar beam suitable for a scanning geometry are determined and the influence of the various source parameters is discussed. In order to develop an accurate model for the simulation of mammography two specimens of the female breast from anatomical courses were scanned in a high-resolution CT. From this data then several voxel models were created containing the characteristic tissue structures found in the breast. Based on the calculation of the x-ray generation and on the created high-resolution voxel models of the breast a Monte Carlo simulation of the absorption and scattering processes was developed for the accurate simulation of mammography with laser-based x-ray sources. This simulation takes into account all relevant properties of the source, such as the spatio-spectral x-ray distribution in the beam and models the image formation and dose deposition process of an imaging procedure with a scatter reducing scanning geometry. Using that simulation it is shown that a significant reduction of the dose necessary to achieve a certain image quality can be achieved in mammography when compared to conventional x-ray tubes and the influence of the different source parameters on the dose reduction potential is quantified and discussed. The methods and tools developed in this work in the context of mammography also provide a basis for the future investigation of more advanced imaging modalities using compact laser-driven x-ray sources.

Contents

1 Introduction

Breast cancer is globally the most common type of cancer in women (excluding non-melanoma skin cancer) and is the leading cause of death from cancer in the developed countries [WHO08, FSB10]. Depending on the specific information source and modeling methods the number of new cases globally is estimated (for both sexes) to be in the range of about 1.1 millions [WHO08] (estimated for 2004) up to 1.38 millions [FSB10] (estimated for 2008) each year causing a mortality rate of about 459,000 deaths [FSB10] (estimated for 2008) up to 519,000 deaths [WHO08] (estimated for 2004) per year.

Mammography is the most widely used breast imaging modality for the detection of early breast cancer in women and its diagnostic performance and suitability as a screening tool has been steadily improved by technological advances in recent times [PGH05]. By now, several studies have attributed the reduction in mortality from breast cancer in the last decades at least in elderly women partly to the introduction of breast screening programs using mammography [FE03]. However the long lasting debate about whether the benefits of screening mammography outweigh its risks [Wel10, PW09] connected to the still unsatisfactory sensitivity and especially the specificity being too low, indicates that mammography and especially mammography screening as done today still leaves much room for improvement.

1.1 Importance of dose reduction in mammography

It is well known that ionizing radiation can have a number of short term as well as long term biological effects (see [Tur08], chapter 13 and references therein). These effects can be classified as deterministic or stochastic depending on whether they occur in a direct causal relationship with the irradiation or only in a statistical manner in combination with other influences. Radiation is a known carcinogen and the occurrence of cancer as a result from an exposure to radiation is a prime example of such a stochastic effect. While deterministic effects usually can not be observed below a certain dose threshold the situation for stochastic effects is not so clear. Although it is known that at higher doses the life-time attributable risk of induced cancer caused by radiation exposure is increased [MR94, SBD04] for low radiation doses the dose-response relationship is still subject of ongoing research [BS89, BEI06, SSA92].

While the potential increase in the life-time attributable risks of induced cancer from relatively low radiation doses is not yet fully understood there is consensus that the

so called linear-no-threshold hypothesis [WKE06], which extrapolates the excess cancer risk linearly down from higher doses, where the risks are statistically significant, should be used for radiation protection considerations [HRS11, Bre10]. This led to the recommendation of the ICRP (International Commission on Radiological Protection) and the BfS (Bundesamt für Strahlenschutz) to keep the patient dose as low as reasonable achievable, which is the so-called ALARA principle [ICR77, ICR07, PH01].

Especially for mammography as a screening tool where the radiation dose accumulates over time and as the examinations are performed on healthy patients there is a trade-off to be made between the diagnostic accuracy and the potential induction of breast cancer by the radiation exposure during mammography itself. Therefore it is imperative to optimize every mammography procedure with respect to the provided diagnostic performance and the radiation dose deposited in the radiation sensitive glandular breast tissue. In the light of an ever increasing number of radiological examinations the importance of dose reduction in x-ray imaging has been repeatedly expressed [Bre10].

A reduction of the radiation dose translates directly into a reduction of the risk of induced cancer. In a recent study a model was developed for estimating the risk of radiation-induced breast cancer in a cohort of 100,000 Canadian women receiving digital mammography with two views per breast, at a total dose of 3,7 mGy [YM11]. Based on this model and the linear-no-threshold hypothesis it can be estimated that for annual screening from 40-55 years and biennial screening until 74 years, a reduction of the radiation dose by a factor of 3 in this cohort avoids another 57 cases of breast cancer. Assuming present curing rates and life-expectancies this translates to saving 7 deaths from breast cancer just in the considered cohort and allowing for 91 more years of life. Radiation-induced breast cancer also incurs high health care costs: For the U.S. in 2010, a recent study estimated the cost in the last year of life to range between 94,284 US$ (age $<$65) and 62,856 (age 65+) [MYS11]. Avoiding radiation-induced breast cancer increases survival and quality of life, lowers health care cost, and improves the cost-effectiveness of mammography screening. This may make screening more attractive to patients and payers, and may lead to an extension of target groups eligible for screening programs.

1.2 Limitations of x-ray tubes

Todays radiological practice is based fundamentally on the use of x-ray tubes whose basic working principle has not changed since their invention at the turn of the nineteenth century and which have some inherent deficiencies that are difficult to overcome. First and foremost even with modern highly optimized x-ray tubes with K-edge filtration techniques the spectrum of the generated radiation still remains polychromatic, which

reduces the image contrast due to high energetic x-rays and leads to an increased dose due to the lower energetic x-rays being absorbed entirely [Ang04]. Furthermore the spatial resolution properties are limited by the finite focal-spot size and divergence of the x-ray beam generated by x-ray tubes. While there also have been attempts at filtering the polychromatic tube spectrum using monochromators based on Bragg reflection on crystal surfaces [LADK05, DDR04] this leads to unacceptable exposure times due to almost all parts of the spectrum being rejected.

Therefore new ways of generating x-rays suitable for the clinical application have to be considered in order to improve the relation of the diagnostic accuracy to the applied radiation dose in medical imaging. At large kilometer-scale brilliant synchrotron facilities the use of synchrotron radiation in medical imaging has been investigated and the advantages have been shown already in studies with humans for mammography [BCDM95, MVF03, MVF00, CTA11] and angiography [DEG92] amongst others. However in order to get those advantages into the clinical practice, more compact and less costly, table-top sized brilliant x-ray sources have to be developed.

1.3 Development of laser-driven x-ray sources

In 1979 Tajima and Dawson proposed a much more compact method to accelerate electrons on a cm-scale which is called laser wake field acceleration [TD79]. It is based on using an intense laser pulse, which ionizes the atoms of a gas target and produces a plasma wave that generates large longitudinal electrical fields by which the electrons get accelerated to relativistic energies [PMtV02]. Since then advances in the development of laser technology reaching increased intensities and shorter pulse lengths have enabled successive advances in the field of laser wake field acceleration leading to higher electron energies [F04, G04, H08, OPM08, M04] up to 1 GeV [LNG06].

There exist different methods of generating x-rays from laser-accelerated electrons. One possibility is to use Thomson backscattering of another laser pulse with the accelerated electrons [STEF92, KCS94, CMT03, OGS09]. However these sources have shown to deliver only a very narrow beam of a few mrad which together with a low flux would make it difficult to image larger areas.

Another recently developed type of table-top sized laser-driven x-ray source that allows the generation of tunable quasi-monochromatic x-rays is based on the creation of x-rays in an undulator [FWP09]. These sources consist of a laser-driven electron accelerator and an undulator [OMR10] which is a periodic arrangement of magnets, that results in an oscillating electron motion which makes them spontaneously emit synchrotron radiation. It has been shown in experiments that these sources are already capable of

generating pulses of soft x-rays with low shot to shot fluctuations [FWP09]. With further advances in laser technology it is reasonable to assume that in the near future higher x-ray energies can be reached which would open up many opportunities in medical imaging. The basic output from this type of source are spontaneous x-rays but ultimately also much brighter and coherent x-ray beams could be produced by a table-top sized free electron laser whose concept has been developed based on a similar design [GBS07].

1.4 Mammography with laser-driven quasi-monochromatic x-ray sources

As in the future higher x-ray energies could be reached by laser-driven x-ray sources one of the first imaging modalities that are feasible is mammography. The radiation produced by these sources would have a number of advantages over the radiation produced by conventional x-ray tubes. The main advantage is the tunable nearly monochromatic x-ray spectrum that allows the selection of the optimal x-ray energy [SH10] depending on the breast thickness, composition and other parameters of the chosen mammography setup. As shown in this work this would lead to a significantly higher contrast-to-noise ratio per dose in the mammograms when compared to polychromatic x-ray tubes that can only be tuned by selecting an anode material and voltage together with a combination of filters. Furthermore these radiation sources operate in a pulsed way thereby eliminating motion artifacts for smaller details due to the extremely short exposure times per shot. Because of the naturally collimated beam it is also possible to image the breast with a scanning geometry which leads to the almost complete avoidance of influences due to scattered radiation usually degrading the image quality in standard mammography. Moreover the low divergence of the x-ray beam leads to less blur in the mammogram, especially for magnification settings, and hence better spatial resolution which is the crucial factor for the detection of microcalcifications. Some of these advantages already have been demonstrated at synchrotron facilities which are the only x-ray sources with a comparable beam quality [BCDM95, MVF00, MVF03].

1.5 Purpose and structure of this work

The aim of this work is to investigate the application of a laser-driven undulator x-ray source to medical imaging and to compare its performance to that of conventional x-ray tubes. The focus here lies on mammography as one of the first feasible imaging modalities, as the lower energetic x-rays would be the first to be achieved with increasing laser power. As currently the output of this type of laser-based x-ray source still not

exceeds the soft x-ray energy range this work relies on the calculation of the x-ray production and subsequently on the simulation of the image formation process in order to obtain a quantitative analysis. These calculations and simulation methods developed in this work also should provide a basis for future investigation of more advanced imaging techniques using laser-driven x-ray sources.

At first the basic theory of the creation of spontaneous undulator radiation is reviewed in chapter 2. There also a concise description of the interactions of x-rays with matter is given in the context of medical imaging and a simple analytical model of the relationship between the image-quality-to-dose ratio and the x-ray energy is developed. This model provides a basic understanding of the more specific calculations done in later chapters and gives an estimate of the optimal x-ray energy for different imaging modalities as well as an estimate of the dose reduction opportunity when using optimized mono-energetic x-rays.

In chapter 3 the calculation of the dynamics of the laser-accelerated electrons and the subsequent calculation of the x-ray production in the context of an x-ray imaging setup is presented which shows that it is possible to create a quasi-monochromatic, low-divergent, laminar beam suitable for medical imaging applications. The specific parameters of the source needed for the creation of a laminar beam suitable for a scanning geometry are determined and the influence of those parameters on the beam geometry is discussed.

In order to develop an accurate model for the simulation of mammography two specimens of the female breast from anatomical courses were scanned in a high-resolution CT. From this data then several voxel models were created containing the characteristic tissue structures found in the breast which is described in chapter 4.

Based on the calculation of the x-ray generation and on the created high-resolution voxel models of the breast a Monte Carlo simulation of the absorption and scattering processes was developed for the accurate simulation of mammography with laser-based x-ray sources which is described in chapter 5. This simulation takes into account all relevant source parameters, such as the spatio-spectral x-ray distribution in the beam and models the image formation and dose deposition process of an imaging procedure with a scanning geometry.

Using that simulation it is shown in chapter 6 that a significant reduction of the dose necessary to achieve a certain image quality can be achieved when compared to conventional x-ray tubes and the influence of the different source parameters on the dose reduction potential is quantified and discussed. Finally using the simulation methods developed in this work a method of filtering the higher energetic x-rays is presented which would be necessary for an optimized application of the laser-driven undulator x-ray source in medical imaging.

2 Theory

This chapter gives an overview of the theory which serves as foundation for the work presented in later chapters. At first, the basic physics of the creation of spontaneous undulator radiation is discussed and the basic equations describing its spectral properties, angular distribution and flux are derived. This is needed in order to understand the more detailed numerical calculations of the creation of undulator radiation given in chapter 3. In the second section of this chapter the interactions of x-rays with matter in the context of x-ray imaging are discussed. Finally in the last section of this chapter the image formation process is discussed and a simple analytical model of x-ray absorption imaging is presented.

2.1 Undulator radiation

Undulators are devices consisting of a periodic arrangement of magnets and are typically used in accelerator physics in order to produce highly intense and narrow banded x-ray radiation. While the electron acceleration can be achieved by various means the basic principles of the x-ray generation with undulators are shared between the different types of sources. The purpose of this section is to derive the fundamental equations describing the creation of x-rays in an undulator and investigate the influence that different parameters of the undulator have on the resulting x-ray beam. The discussion of the theory in this section is limited to the derivation of the equations needed for the investigation of x-ray imaging done in later chapters and the reader is referred to the textbooks [Cla04], [Wil96] and [ÖE03] for a more detailed review of the subject.

The generation of undulator radiation is based on the coupling of electrons to the radiation field and on the periodic structure of the magnetic field created by the undulator. Electrons that pass through the undulator are forced by its periodic magnetic field onto a periodic trajectory leading to the emission of electromagnetic radiation of the accelerated electrons. Therefore the derivation begins with a general description of the electromagnetic field generated by a moving point charge.

2.1.1 Electromagnetic field of a moving point charge

Following [Jac75] (chapter 14) and [TH03] (chapter 8.3) the so called Liénard-Wichert potentials consisting of the scalar potential Φ and the vector potential $\mathbf{A}$ of a point charge at the position $\mathbf{r}$ moving with the velocity $c\boldsymbol{\beta}$ are given by

$$\Phi\left(\mathbf{x}, t\right) = e \left.\frac{1}{\kappa R}\right|_{\mathrm{ret}} \tag{2.1}$$

and

$$\mathbf{A}\left(\mathbf{x},t\right)=e\left.\frac{\beta}{\kappa R}\right|_{\mathrm{ret}} \tag{2.2}$$

where

$$R=\left|\mathbf{x}-\mathbf{r}\right|$$

is the distance between the electron position $\mathbf{r}$ and the observer position $\mathbf{x}$ while κ is defined as

$$\kappa=1-\mathbf{n}\cdot\boldsymbol{\beta}$$

where

$$\mathbf{n}=\frac{\mathbf{x}-\mathbf{r}}{\left|\mathbf{x}-\mathbf{r}\right|}$$

is the unit vector pointing from $\mathbf{r}$ to $\mathbf{x}$. The subscript "ret" indicates that the expressions are to be evaluated at the so called "retarded" time

$$t_{\mathrm{ret}}=t-\frac{R\left(t_{\mathrm{ret}}\right)}{c}$$

which accounts for the fact that the position and motion of the charge at the time t_{ret} contributes to the fields seen by the observer at the later time $t=t_{\mathrm{ret}}+\frac{R(t_{\mathrm{ret}})}{c}$. In figure 2.1 a sketch of the situation containing the positions of the electron and of the observer is shown.

By definition the electric field $\mathbf{E}$ is given by

$$\mathbf{E}=-\nabla\Phi-\frac{1}{c}\frac{\partial}{\partial t}\mathbf{A} \tag{2.3}$$

whereas the magnetic field $\mathbf{B}$ is given by

$$\mathbf{B}=\nabla\times\mathbf{A} \tag{2.4}$$

Substituting equation 2.1 and 2.2 in equation 2.3 and 2.4 respectively and evaluating these expressions one finds that the electric field of a moving point charge can be written as

$$\mathbf{E}\left(\mathbf{x},t\right)=e\left[\left(\frac{\left(\mathbf{n}-\boldsymbol{\beta}\right)\left(1-\boldsymbol{\beta}^{2}\right)}{\kappa^{2}R^{2}}\right)\right]_{\mathrm{ret}}+\frac{e}{c}\left[\frac{\mathbf{n}}{\kappa^{2}R}\times\left(\left(\mathbf{n}-\boldsymbol{\beta}\right)\times\frac{\mathrm{d}}{\mathrm{d}t}\boldsymbol{\beta}\right)\right]_{\mathrm{ret}} \tag{2.5}$$

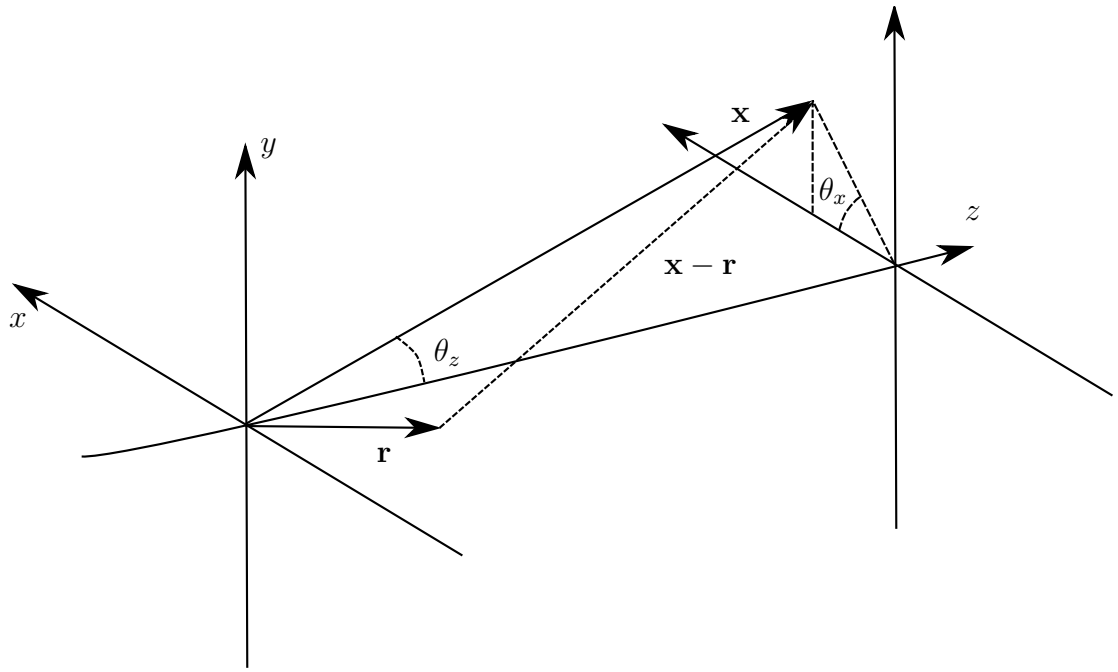

Figure 2.1: Sketch of the electron position $\mathbf{r}$, of the observer position $\mathbf{x}$ and of the observation angles θ_x and θ_z at a specific time. The distance vector $\mathbf{x}-\mathbf{r}$ pointing from the electron position to the observer position is indicated by a dashed line.

The magnetic field is then simply given by

$$\mathbf{B} = \mathbf{n} \times \mathbf{E} \tag{2.6}$$

Equation 2.5 together with equation 2.6 provide an accurate description of the so called "near field" of the electromagnetic field around a moving point charge. If the electric field is observed at a large distance from the charge then $\mathbf{n}$ approximately becomes constant and the first summand of equation 2.5 depending on the velocity falls off as $1/R^2$ and can therefore be neglected in this limit. The resulting equation that depends on the acceleration of the moving charge can be written as

$$\mathbf{E}_{\text{farfield}}\left(\mathbf{x}, t\right) = \frac{e}{c}\left[\frac{\mathbf{n}}{\kappa^2 R} \times \left((\mathbf{n} - \boldsymbol{\beta}) \times \frac{\mathrm{d}}{\mathrm{d}t}\boldsymbol{\beta}\right)\right]_{\text{ret}} \tag{2.7}$$

and is called "far field approximation".

2.1.2 Electron motion in an undulator

The periodic arrangement of dipole magnets forming an undulator generates a sinusoidal magnetic field with a field strength in the y-direction of

$$B_y(z) = -B_0 \sin(k_u z) \tag{2.8}$$

where k_u is given by $k_u = \frac{2\pi}{\lambda_u}$ and λ_u is the undulator period length. This magnetic field leads to a sinusoidal motion of the electrons as these are accelerated by the Lorentz force

$$\mathbf{F} = -ec\boldsymbol{\beta} \times \mathbf{B}$$

which leads to a coupled second order differential equation for the electron coordinates

$$x'' = -\frac{e}{\gamma m_e} B_y z' \tag{2.9}$$

$$z'' = -\frac{e}{\gamma m_e} B_y x' \tag{2.10}$$

where γ is the Lorentz factor which is defined as

$$\gamma = \frac{1}{\sqrt{1 - \frac{v^2}{c^2}}}$$

If the deflection of the electrons from the z-axis is small it can safely be assumed that $\beta_x \ll \beta_z$ and $z'' = 0$. Using this approximation and substituting equation 2.8 into the equations of motion 2.9 and 2.10 these can be solved and the time dependent transversal and longitudinal position can be obtained as

$$x(t) = \frac{eB_0}{\gamma m_e \beta c k_u^2} \sin(k_u \beta c) \tag{2.11}$$

and

$$z(t) = \beta c t \tag{2.12}$$

The dimensionless parameter K defined as

$$K = \frac{eB_0}{\gamma m_e \beta c k_u^2} = \frac{eB_0 \lambda_u}{2\pi m_e c} \approx 0.934 B_0 \lambda_u \,[\mathrm{T} \cdot \mathrm{cm}]$$

is called "deflection parameter" since K/γ gives the peak angular deflection of the electron, as can be seen in the equation for the electron trajectory which is obtained by

substituting K in equation 2.11 and using equation 2.12 resulting in

$$x(z) = \frac{K}{\beta\gamma k_u} \sin(k_u z) \tag{2.13}$$

Consequently the velocity in the x-direction is given by

$$x'(z) = \frac{Kc}{\gamma} \cos(k_u z) \tag{2.14}$$

The electron motion can therefore be described as an oscillating motion whose amplitude is proportional to the deflection parameter K. However the equations 2.13 and 2.14 describing the electron trajectory are only valid in the limit of $\beta_x \ll \beta_z$ which is fulfilled for a reasonably small deflection parameter K. Without this approximation the electron velocity in the z-direction reads

$$z'(t) = \sqrt{(c\beta)^2 - x'(t)^2} \approx c\left(1 - \frac{1}{2\gamma^2}\left(1 + \frac{\gamma^2 x'^2}{c^2}\right)\right)$$

where higher orders of γ have been neglected. Using equation 2.14 and averaging over one period gives

$$\overline{z'} = c\left(1 - \frac{1}{2\gamma^2}\left(1 + \frac{K^2}{2}\right)\right) = \overline{\beta}c \tag{2.15}$$

This leads to two equations for the transverse and longitudinal electron motion

$$x(t) = \frac{K}{\gamma k_u} \sin\left(\overline{\beta} c k_u t\right) \tag{2.16}$$

and

$$z(t) = \overline{z'} - \frac{K^2}{8\gamma^2 k_u} \sin\left(2\overline{\beta} c k_u t\right) \tag{2.17}$$

Here one can see that the electron exhibits both a transverse oscillation as well as a longitudinal oscillation.

2.1.3 Fundamental wavelength of the undulator radiation

A Lorentz-transformation in the frame of reference moving along with the electron leads to an electron motion that is given by

$$x^*(t^*) = \frac{K}{\gamma k_u} \sin(\omega^* t^*) \tag{2.18}$$

and

$$z^*(t^*) = -\frac{K^2}{8\gamma k_u \sqrt{1+\frac{K^2}{2}}} \sin(2\omega^* t^*) \tag{2.19}$$

where ω^* is defined as

$$\omega^* = \gamma^* \overline{\beta} c k_u$$

and the the Lorentz-factor γ^* in this frame of reference is given by

$$\gamma^* = \frac{1}{\sqrt{1-\overline{\beta}^2}}$$

Using equation 2.15 ω^* can be approximated by

$$\omega^* \approx \frac{\gamma c k_u}{\sqrt{1+\frac{K^2}{2}}}$$

The radiation field resulting from the electrons motion corresponds to the emission of photons which are described in quantum mechanics as quantized excitations of the radiation field with an energy of $E_{\text{phot}} = \hbar\omega$ where $\hbar = h/(2\pi)$ and h is the Planck constant [GP91]. Considering a photon which is emitted in forward direction under the angle θ_z its energy in the co-moving frame of reference is given by

$$E^*_{\text{phot}} = \hbar\omega^* = \gamma^* \left(E_{\text{phot}} - \bar{\beta}\hbar\omega\cos\theta_z\right) = \gamma^*\hbar\omega\left(1-\overline{\beta}\cos\theta_z\right)$$

In the laboratory frame of reference the frequency of the oscillation then reads

$$\omega = \frac{\omega^*}{\gamma^*\left(1-\overline{\beta}\cos\theta_z\right)}$$

Again using equation 2.15 and using $\cos\theta \approx 1 - \frac{\theta^2}{2}$ thereby discarding higher orders of the cosine the wavelength of the photon in the laboratory frame of reference can be written as

$$\lambda = \frac{\lambda_u}{2\gamma^2}\left(1+\frac{K^2}{2}+\gamma^2\theta_z^2\right) \tag{2.20}$$

The same arguments can be used in order to calculate the wavelength of the higher harmonics which results in the n-th harmonic wavelength given by

$$\lambda_n = \frac{\lambda}{n}$$

As one can see in equation 2.20 the photon energy $E_{\text{phot}} = \hbar 2\pi c/\lambda$ is proportional to the square of the electron energy which itself is proportional to γ. Also the photon energy is inversely proportional to the undulator period length λ_u. Moreover because of the relativistic Doppler effect it has a characteristic dependence on the observation angle θ and falls off inversely with θ^2. This dependence of the photon energy is shown in figure 3.12 in the following chapter, where more detailed calculations of the spectral properties are presented.

2.1.4 On-axis spectral bandwidth of the fundamental

It is interesting to take a closer look at the shape of the spectrum around the fundamental wavelength as in that region most of the x-rays are produced. One can use a simple argument in order to estimate the bandwidth around the fundamental wavelength. As the electrons pass through the undulator they emit radiation in the form of waves. The time the electrons need to pass the undulator is given by $T = \frac{N_u}{\lambda_1 c}$. The wave can therefore be described by

$$E(t) = \begin{cases} E_0 e^{-\mathrm{i}\omega_1 t} & \text{for } t \in [-T/2, T/2] \\ 0 & \text{else} \end{cases}$$

A Fourier transformation into the frequency space leads to

$$\tilde{E}(\omega) = E_0 \int_{.-T/2}^{T/2} e^{-\mathrm{i}(\omega_1-\omega)t} \mathrm{d}t = 2E_0 \frac{\sin\left(T/2\left(\omega_1-\omega\right)\right)}{\omega_1-\omega}$$

The photon flux I is proportional to $|E|^2$ and one obtains

$$I(\omega) \propto \left(\frac{\sin\left(T/2\left(\omega_1-\omega\right)\right)}{\omega_1-\omega}\right)^2$$

and with $T = 2\pi N_u/\omega_1$ and $\chi = \pi N_u\left(\omega_1-\omega\right)/\omega_1$ the flux can be written as

$$I(\omega) \propto \left(\frac{\sin(\chi)}{\chi}\right)^2$$

The line width can be defined as the full width at half maximum χ_{FWHM} of this spectral distribution, determined by $\left(\frac{\sin(\chi_{\text{FWHM}})}{\chi_{\text{FWHM}}}\right)^2 = \frac{1}{2}$. Therefore the photon energy $E_{\text{phot}} = \hbar\omega$ around the fundamental energy $E_{\text{phot},1}$ has a line width of

$$\frac{\Delta E_{\text{phot}}}{E_{\text{phot},1}} = \frac{\chi_{\text{FWHM}}}{\pi N_u} \approx \frac{1}{N_u} \tag{2.21}$$

This estimate of the spectral bandwidth of the fundamental shows that with a reasonably high number of undulator periods the spectrum is sharply peaked around the fundamental photon energy $\hbar 2\pi/\lambda_l$. Note however that in this chapter only single electrons have been considered, leading to a filament electron beam. Also only the on-axis properties have been investigated. For thick electron beams encountered in experiments the total spectrum has the following characteristic: because of the angular dependence in the undulator equation the spectral bandwidth widens and the mean x-ray energy decreases because of the lower-energetic higher-angle contribution from off-axis electrons. In section 3.3 detailed calculations of undulator spectra for thick electron beams are presented and the influence of the number of undulator periods is shown in figure 3.8.

2.1.5 Angular spread of the undulator radiation

As shown in the equation 2.20 the fundamental wavelength has an angular dependence leading to an increased off-axis wavelength. However also the photon flux of the undulator radiation shows an angular dependence. At first the relativistic motion of the electrons has to be taken into account. As the photons are emitted tangential to the electron trajectory one has to look at equation 2.13. There it can be see that the electron oscillates within an opening angle θ_e limited by

$$\theta_{e,\max} = \arctan\left(\left.\frac{\mathrm{d}x}{\mathrm{d}z}\right|_{\max}\right) \approx \frac{K}{\beta\gamma} \approx \frac{K}{\gamma}$$

This means that for electrons accelerated at relativistic velocities the radiation is emitted in small cones in forward direction. Consequently a higher electron energy leads to a smaller opening angle of the cone in which the photons are emitted. However these radiation cones also interfere with each other leading to the angular dependence being reduced even further. This can be estimated by a simple argument using an interference condition as described in [Cla04]. Given two waves that are emitted by an electron at an angle θ at two points separated by a distance equal to the undulator period λ_u. As the electron needs a time equal to $\lambda_u/c\beta$ for this distance the first wave travels a distance of λ_u/β Consequently the distance d between these wavefronts then is given by

$$d = \frac{\lambda_u}{\beta} - \lambda_u \cos\theta$$

The condition for the constructive interference of these two waves is fulfilled if the distance is equal to an integer number of wavelengths

$$d = n\lambda_1$$

If this is to hold along the whole length of the undulator and for waves that are radiated from points that are separated by a distance greater than one wavelength the following condition has to be met

$$\frac{\lambda_u}{\beta} - \lambda_u \cos\theta = N_u n \lambda_1 \tag{2.22}$$

Since the angular dependence is of interest here one has to check at which angle θ' destructive interference occurs. This is the case if the distance is longer by an additional distance of $\lambda_l\,(1 + 1/N_u)$ which leads to

$$\frac{\lambda_u}{\beta} - \lambda_u \cos\theta' = N_u n \lambda_1 + \lambda_1 \tag{2.23}$$

Expanding the cosine only to the second order which is acceptable for small angles and equating the equations 2.22 and 2.23 it follows that

$$\theta'^2 - \theta^2 = \frac{2\lambda_1}{N_u \lambda_u}$$

From this the angle at which the intensity falls to zero is estimated to be

$$\Delta\theta = \sqrt{\frac{2\lambda_1}{N_u\lambda_u}} = \frac{1}{\gamma}\sqrt{\frac{1 + K^2/2}{N_u}} = \frac{1}{\gamma^*\sqrt{N_u}} \tag{2.24}$$

Here one can see that the angle at which the photons are radiated is even further reduced by the interference effects inside the undulator which increase with a higher number of undulator periods. Again in this calculation only single electrons have been considered and the effects of the divergence and spatial spread of a realistic electron beam has been neglected.

2.1.6 Spectral-angular flux distribution of the undulator radiation

In the last subsections the electron motion has been approximated in order to estimate the fundamental wavelength as well as the bandwidth of the fundamental and of the angular spread. A more rigorous derivation of the spectral properties of the radiation emitted by electrons moving in an undulator can be done based on the far field approximation given by equation 2.7. A Fourier transform of this equation gives the electric field in the frequency domain

$$\mathbf{E}\,(\mathbf{x}, \omega) = \frac{-\mathrm{i}e}{2\pi c\kappa^2 R} \exp\left(\mathrm{i}\frac{\omega}{c}\mathbf{n}\cdot\mathbf{x}\right) \mathbf{H}\,(\mathbf{n}, \omega) \tag{2.25}$$

where for the oscillatory motion of the electron in the undulator $\mathbf{H}$ is given by

$$\mathbf{H}(\mathbf{n},\omega) = \frac{\omega}{2\pi}\int_{-\infty}^{\infty}\left((\mathbf{n}-\boldsymbol{\beta})\exp\left[\mathrm{i}\omega\left(t'+\frac{R}{c}\right)\right]\right)\mathrm{d}t' \tag{2.26}$$

As the magnetic field of an undulator in the limit of an infinitely long undulator is periodic on the whole longitudinal axis the electron motion described by equation 2.16 and 2.17 is also periodic. Consequently the integral in the far field equation 2.26 reduces to a series. Following [ŌE03] and after evaluating all terms in the integral this series can be written as

$$\mathbf{H}(\theta_x,\theta_z,\omega) \approx N_u\sum_{n=1}^{\infty}(-1)^{n(N_u-1)}\,\mathbf{h}_n(\theta_x,\theta_z)\,\mathrm{sinc}\left[\pi\mathrm{N_u}\left(\frac{\omega}{\omega_1}-\mathrm{n}\right)\right] \tag{2.27}$$

where ω_1 is the previously defined frequency of the first harmonic and $\mathbf{h}_n$ is given by

$$\begin{aligned}\mathbf{h}_n(\theta_x,\theta_z) = \frac{n}{\lambda_1}\int_0^{\lambda_u}&\begin{pmatrix} K/\gamma\cos(2\pi s/\lambda_u)-\theta_x \\ -\theta_z\end{pmatrix}\\ &\exp\left[in2\pi\left(\frac{s}{\lambda_u}+\frac{-2\gamma\theta_x K\sin(2\pi s/\lambda_u)+K^2/4\sin(4\pi s/\lambda_u)}{2\pi\left(1+K^2/2+\gamma^2\left(\theta_x^2+\theta_z^2\right)\right)}\right)\right]\mathrm{d}s\end{aligned} \tag{2.28}$$

As one can see already in equations 2.16 and 2.17 the longitudinal oscillation of the electrons is twice as fast as the transverse oscillation therefore in the electron rest frame these two oscillations lead to a so-called figure-8 motion described by equation 2.18 and 2.19. For a small deflection parameter $K \ll 1$ the longitudinal oscillation can be neglected and the electric field seen by an observer on-axis ($\theta = 0$) is of continuous sinusoidal shape. This means that after a Fourier transformation into the frequency domain the spectrum of the emitted radiation only consists of one peak at the first harmonic frequency. As K increases the on-axis observer does not see the emitted radiation continuously as the electron radiates also at higher angles. However as the radiation peaks emitted on-axis are still observed at equally spaced points in time and the electric field as a function of the time is point symmetric the spectrum only consists of odd harmonics. At higher observation angles, this is no longer true and the peaks of the electric field are no longer equally spaced in time and consequently higher harmonic frequencies are observed. The lack of even harmonics in the on-axis spectrum of a filament electron beam can be seen in figure 3.7 in chapter 3.

The angular spectral flux can be calculated from equation 2.25 for the electric field

resulting in

$$\frac{\mathrm{d}W}{\mathrm{d}\omega}\left(\theta_x,\theta_z,\omega\right)=8\pi\varepsilon_0 cR^2\left|E\left(\theta_x,\theta_z,\omega\right)\right|^2=\alpha\frac{I}{e}\left|\mathbf{H}\left(\theta_x,\theta_z,\omega\right)\right|^2$$

where I is the electron current and $\alpha\approx 1/137$ is the fine structure constant. As shown in [ŌE03] the square of the absolute value of $\mathbf{H}$ given by the sum in equation 2.27 reduces to

$$\begin{aligned}\frac{\mathrm{d}W}{\mathrm{d}\omega}\left(\theta_x,\theta_z,\omega\right)&=\sum_{n=1}^{\infty}\frac{\mathrm{d}W_n}{\mathrm{d}\omega}\left(\theta_x,\theta_z,\omega\right)\\&=\sum_{n=1}^{\infty}\alpha\frac{I}{e}N_u^2\left|\mathbf{h}_n\left(\theta_x,\theta_z\right)\right|^2\operatorname{sinc}^2\left[\pi\mathrm{N_u}\left(\frac{\omega}{\omega_1\left(\theta_\mathrm{x},\theta_\mathrm{z}\right)}-\mathrm{n}\right)\right]\end{aligned}\tag{2.29}$$

The sinc^2 terms only give a contribution to the flux if $\omega\left(\theta_x,\theta_z\right)$ and therefore $\lambda=2\pi c/\omega$ fulfills the resonance condition given by equation 2.20. If the electron moves along the z-axis, equation 2.29 describing the angular flux and the fundamental undulator equation 2.20 describing the resonance condition only depend on θ_z and the flux distribution at certain energy is rotation symmetric to the z-axis and is of circular shape. This can be seen in figure 3.19 b) where the photon flux density for a filament electron beam is plotted for a certain energy interval. As the resonance frequency given by the fundamental undulator equation 2.20 falls off for larger angles the radius of these circular patterns increases. The $\left|\mathbf{h}_n\left(\theta_x,\theta_z\right)\right|^2$ term is then responsible for the angular intensity distribution along these circular patterns for each harmonic.

A thorough evaluation of the series in equation 2.29 is done in [Cla04] and gives

$$\begin{aligned}\frac{\mathrm{d}W_n}{\mathrm{d}\omega}\left(\theta_x,\theta_z,\omega\right)=\alpha\frac{I}{e}N_u^2\gamma^2 L\left(\frac{N_u\Delta\omega}{\omega_1}\right)\Bigg|&2\gamma\theta_z\cos\theta_x\sum_{p=-\infty}^{\infty}J_{n+2p}\left(X\right)J_p\left(Y\right)\\&-K\left(\sum_{p=-\infty}^{\infty}J_{n+2p-1}\left(X\right)J_p\left(Y\right)+\sum_{p=-\infty}^{\infty}J_{n+2p+1}\left(X\right)J_p\left(Y\right)\right)\Bigg|^2\end{aligned}\tag{2.30}$$

where J_n is the n-th Bessel function and

$$X=\frac{2n\gamma\theta_z K\cos\theta_x}{A},\ Y=\frac{nK^2}{4A},\ L\left(x\right)=\frac{\sin^2\left(\pi x\right)}{N_u^2\sin^2\left(\frac{\pi}{N_u}x\right)}$$

In the on-axis case where $\theta_z = 0$ this leads to

$$X = 0,\ Y = \frac{nK^2}{4\left(1 + K^2/2\right)}$$

Because $J_k\left(0\right)$ is only non-zero for $k = 0$ the expression for $\frac{\mathrm{d}W_n}{\mathrm{d}\omega}$ reduces to

$$\left.\frac{\mathrm{d}W_n\left(\theta_z = 0, \theta_x = 0, \omega\right)}{\mathrm{d}\omega}\right|_{\theta_z=0} = \alpha\frac{I}{e}N_u^2\gamma^2 L\left(\frac{N_u\Delta\omega}{\omega_1}\right)F_n\left(K\right) \tag{2.31}$$

where F_n is defined by

$$F_n\left(K\right) = \frac{n^2K^2}{\left(1 + K^2/2\right)}\left(J_{(n+1)/2}\left(Y\right) - J_{(n-1)/2}\left(Y\right)\right)^2 \approx \frac{K^2}{1 + K^2/2}$$

The photon flux given by $N = W/\left(\hbar\omega\right)$ and following [Cla04] the on-axis, spectral, angular photon flux per bandwidth $\left(dN'/\mathrm{d}\Omega\right)|_{\theta_z=0}$ can be calculated leading to the estimate

$$\left.\frac{\mathrm{d}N'}{\mathrm{d}\Omega}\right|_{\theta_z=0} \approx 1.744 \times 10^{14} N_u^2 E^2 I F_n\left(K\right) \tag{2.32}$$

where the electron energy is given in the unit [GeV] and the electron current in the unit [A].

2.1.7 Total flux in the fundamental and the higher harmonics

The angular spread of the undulator radiation has already been given in equation 2.24. Approximating the on-axis flux by a Gaussian with a standard deviation $\sigma_\theta = \sqrt{\lambda_1/\left(N_u\lambda_u\right)}$ as given in equation 2.24 the spectral on-axis flux per bandwidth can be estimated by

$$\frac{\mathrm{d}N'}{\mathrm{d}\Omega} = \left.\frac{\mathrm{d}N'}{\mathrm{d}\Omega}\right|_{\theta_z=0}\exp\left(-\frac{\theta_z^2}{2\sigma_\theta^2}\right)$$

Now integrating over all angles results in

$$N' = 2\pi\sigma_\theta^2\left.\frac{\mathrm{d}N'}{\mathrm{d}\Omega}\right|_{\theta_z=0} = \alpha\pi\frac{I}{e}N_u\frac{\Delta\omega}{\omega}Q_n\left(K\right)$$

where

$$Q_n\left(K\right) = \frac{K^2}{1 + K^2/2}F_n\left(K\right)$$

Using SI-units the number of photons per second and per 0.1% bandwidth in the central cone can be written as

$$N' \approx 1.431 \times 10^{14} N_u I Q_n\left(K\right) \tag{2.33}$$

2.2 Interactions of x-rays with matter in x-ray imaging

The purpose of this section is to provide a short overview of the interaction of x-rays with matter in the energy range typically used in x-ray imaging and of the physics effects in this context. The quantum-mechanical description of the interaction of the radiation field with charged particles is the subject of quantum field theory which provides an accurate description of the matter-radiation system and can be used to calculate the cross sections of absorption an scattering processes of photons with matter. For an introduction into the quantum-mechanical description of the interaction of radiation with matter the reader is referred to [GP91] (chapter 15.5) as well as [DD07] and [Wei96], while a less theoretical discussion of the interaction of photons with matter in the context of x-ray imaging and dosimetry can be found in [Tur08].

As in this work the considered photon energies are in the range of several keV and well below 1 MeV the interaction of the photons with matter are either absorption or scattering processes of which certain limiting cases are described in the following subsections.

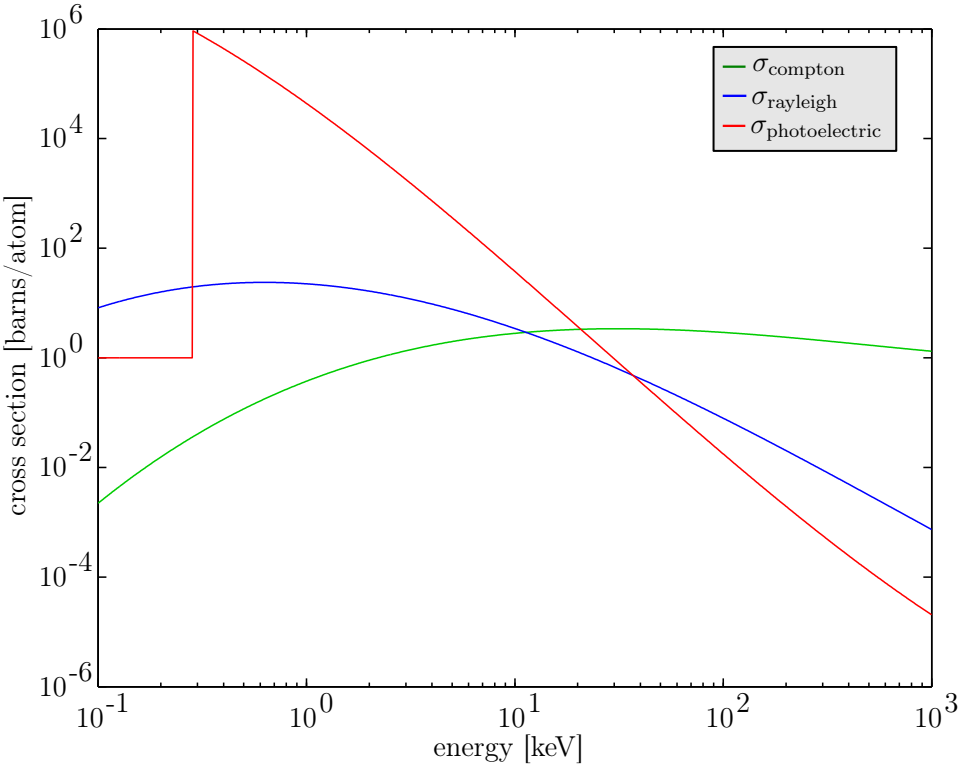

Figure 2.2: Logarithmic plot of the cross sections corresponding to the interactions of x-rays with carbon in the energy range relevant in medical imaging. The data published in [MGMH69] has been used for generating the plot.

2.2.1 The Photoelectric effect

The absorption of photons in matter occurs in the photoelectric effect where x-rays are absorbed leading to an emission of electrons. It is the dominant effect for lower photon energies E_p and rapidly decreases for higher photon energies approximately as E_p^{-3} as can be seen in figure 2.2. The energy dependence of the cross section shows a characteristic edge structure which depends on the atomic number of the material involved in the absorption process and results from the electronic structure of the atoms involved in the absorption process. The cross section of the photoelectric effect strongly depends on the effective atomic number Z of the material and is approximately proportional to Z^4.

2.2.2 Compton scattering

The incoherent scattering of photons in matter is called Compton scattering and its cross section can be calculated in the context of quantum electrodynamics [DD07, Wei96]. In this inelastic scattering process the photons loose some of their energy which is transferred to the charged particle that is involved in the scattering process. The energy shift of the photon follows from the conservation of energy and momentum and is proportional to $1 - \cos\theta$ where θ is the scattering angle. As can be seen in figure 2.2 it becomes the prevalent effect for higher photon energies. The Compton scattering cross section shows a linear dependence on the atomic number of the material.

2.2.3 Rayleigh scattering

The coherent scattering of a photon with a whole atomic system is called Rayleigh scattering. The scattering is elastic in the sense that the photon retains its energy but is scattered at certain angle which in the context of x-ray imaging is predominantly low. As Rayleigh scattering is a type of coherent scattering the structure of the material the photon is scattered from influences the angular distribution of the scattering. For higher photon energies the cross section of Rayleigh scattering quickly decreases as can be seen in figure 2.2.

2.3 Model of the image formation process in x-ray absorption imaging

Before studying the image formation process in x-ray absorption imaging on a more detailed level it is helpful to consider a simplified analytical model in order to understand and interpret more complex calculations. Therefore a model of the basic problem of optimizing the image quality to dose ratio in x-ray absorption imaging is presented in this section. In x-ray absorption imaging contrast is generated by the inhomogeneous absorption of x-rays throughout the imaged object. Depending on the beam geometry of

the considered x-ray source each x-ray traverses the imaged object along a certain path and the photon corresponding to this x-ray is then either being absorbed in the object, being scattered or being transmitted and hitting the detector. Associated to each path there is an absorption probability which depends on the specific material composition and density of the object along this path. These absorption probabilities and their associated realizations for a certain number of x-rays manifest themselves as a spatial intensity distribution at the detector. Assuming that the probability of one photon being transmitted through an object with a certain material, density and infinitesimal thickness $\mathrm{d}x$ is given by

$$p\left(E\right)\mathrm{d}x = 1 - \mu\left(E\right)\mathrm{d}x$$

where $\mu\left(E\right)$ is the so called attenuation coefficient, depending on the x-ray energy E. The continuous limit for the transmission probability of a composite object with spatially dependent attenuation coefficient $\mu\left(E,x\right)$ is then given by

$$p\left(E\right) = \exp\left(-\int\limits_{C}\mu\left(E,x\right)\mathrm{d}x\right)$$

where C denotes the path of the photon. The attenuation coefficient $\mu\left(E,x\right)$ depends on the material composition and density present at the position x and is given by

$$\mu\left(E,x\right) = N_A\rho\left(x\right)\sum_i\sum_j\frac{c_i\left(x\right)}{M_i}\sigma_{i,j}\left(Z_i,E\right) \tag{2.34}$$

where N_A is the Avogadro constant, $\rho\left(x\right)$ is the density of the material at position x, i is the index corresponding to the i-th element in the material, j is the index corresponding to the j-th physics process, while $c_i\left(x\right)$, M_i, $\sigma_{i,j}$ and Z_i are the mass fractions, the molar masses, the cross sections of the photoelectric effect per atom and the atomic number of the i-th element respectively.

For n incident photons the probability P that k photons are transmitted (including scattering) is then given by the binomial distribution

$$P\left(k;n,p\left(E\right)\right) = \left(\begin{array}{c} n \\ k \end{array}\right)p\left(E\right)^k\left(1-p\left(E\right)\right)^{n-k} \tag{2.35}$$

As the limit of a large number of photons is of interest here one can make use of a special case of the central limit theorem called DeMoivre-Laplace limit theorem [Fel68] which in this context states that the probability distribution P approaches a normal distribution with mean value np and variance $np\left(1-p\right)$ in the limit $n\to\infty$. Explicit estimation of the rate of convergence [Fel68] (chapter VII.4, table 2) shows that the error

is very small for those large numbers of photons considered in this work. This justifies the approximation of P by a continuous probability density given by

$$P\left(k; n, p\left(E\right)\right) \approx \mathcal{N}\left(np, n\left(1-p\right)\right)$$

where $\mathcal{N}\left(\mu, \sigma^2\right)$ is the normal distribution with a mean value μ and variance σ^2 defined by

$$\mathcal{N}\left(\mu, \sigma^2\right) = \frac{1}{\sqrt{2\pi\sigma^2}} \exp\left(-\frac{\left(x-\mu\right)^2}{2\sigma^2}\right)$$

As in medical applications of x-ray absorption imaging one is interested in the signal modulation on the x-ray detector as well as in the radiation dose deposited during the x-ray exposure it is convenient to introduce a figure of merit for certain imaging tasks. This figure of merit should capture the desire to achieve a high detector signal modulation at a low level of statistical fluctuations together with a low dose level. Following [Bur99, ICR95] and considering a region of interest on the detector containing a certain detail of the image a simple estimate of the visibility of this detail is given by the signal-difference-to-noise ratio (SDNR) which can be defined according to

$$\mathrm{SDNR} = \frac{S_b - S}{\sigma_b} \tag{2.36}$$

where S_b is the detector signal of the background area surrounding the detail S is the detector signal of the region of interest containing the detail and σ_b is the standard deviation of the pixel values of the background area.

As in this work mammography has been chosen as prime imaging application the appropriate estimate of the radiation dose is given by the average glandular dose (AGD) which is the average radiation dose deposited in the radiation sensitive glandular tissue of the breast. Using these definitions the following figure of merit for mammography is chosen

$$\mathrm{SDNR}^2/\mathrm{AGD} = \left(\frac{S_b - S}{\sigma_b}\right)^2 /\mathrm{AGD} \tag{2.37}$$

This figure of merit is suitable for the model considered here as for a reasonably large number of x-rays the value of this expression becomes independent from the number of photons as both AGD and SDNR^2 scale linearly with the number of photons. Meaningful values of $\mathrm{SDNR}^2/\mathrm{AGD}$ therefore have to be understood in the limit of a large number of photons. In the limit of an infinite number of incident photons $n \to \infty$ the associated

probability distributions corresponding to this figure of merit are then given by

$$P\left(S_b; E, n\right) = \mathcal{N}\left(np_b\left(E\right), np_b\left(1 - p_b\left(E\right)\right)\right)$$

for the detector signal,

$$P\left(\sigma_b; E, n\right) = \sqrt{np_b\left(1 - p_b\left(E, n\right)\right)}$$

for the standard deviation of this distribution and

$$P\left(S; E, n\right) = \mathcal{N}\left(np\left(E\right), np\left(1 - p\left(E\right)\right)\right)$$

for the detector signal of an area of equal size containing the detail. This leads to a probability distribution for the figure of merit which depends on the x-ray energy E as well as on the number of incident photons n which is given by

$$P\left(\mathrm{SDNR}^2/\mathrm{AGD}; E, n\right) = \left(\frac{P\left(S_b; E, n\right) - P\left(S; E, n\right)}{P\left(\sigma_b; E, n\right)}\right)^2 / P\left(\mathrm{AGD}; E, n\right) \tag{2.38}$$

Using $\mathbb{E}\left(\mathrm{AGD}\right) = En\left(1 - p\left(E\right)\right)$ and $\mathbb{E}\left(S; E, n\right) = np\left(E\right)$ the expectation value corresponding to this probability distribution is then given by

$$\mathbb{E}\left(\mathrm{SDNR}^2/\mathrm{AGD}\right) = \frac{\left(p_b\left(E\right) - p\left(E\right)\right)^2}{Ep_b\left(E\right)\left(1 - p_b\left(E\right)\right)\left(1 - p\left(E\right)\right)}$$

Neglecting scattering processes and using the approximation $\sigma_{\mathrm{phot}} \propto E^{-k}$ for the cross section of the photoelectric effect the exponent k is estimated by performing a least squares fit to the tabulated values for the cross sections corresponding to adipose and glandular tissue as found in [BHS10]. This leads to the approximation

$$k_a \approx 2.98$$

for adipose tissue and to

$$k_m \approx 2.96$$

for a mixture of glandular and adipose tissue. Using these approximations one obtains

$$p_b\left(E\right) \approx e^{-\alpha E^{-k_a}} \quad \text{and} \quad \mathrm{p\left(E\right) \approx e^{-\beta E^{-k_m}}}$$

for a thickness ratio of the background adipose tissue to the thickness of the adipose-glandular detail given by α/β. The expectation value of the figure of merit is then

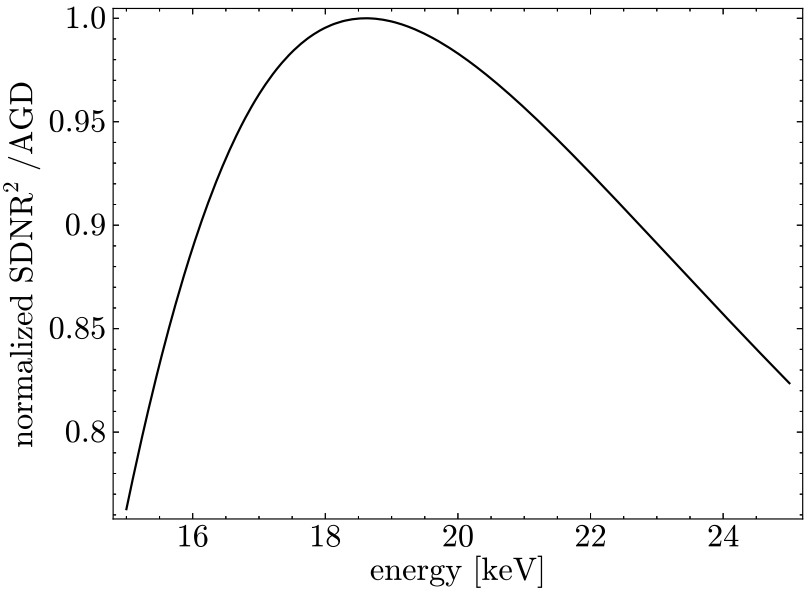

Figure 2.3: Plot of the expectation value of $\mathrm{SDNR}^2/\mathrm{AGD}$ given by equation 2.39 against the x-ray energy normalized to the maximum $\mathrm{SDNR}^2/\mathrm{AGD}$ value.

given by

$$\mathbb{E}\left(\mathrm{SDNR}^2/\mathrm{AGD}\right) = \frac{\left(e^{-\alpha E^{-k_a}} - e^{-\beta E^{-k_m}}\right)^2}{E e^{-\beta E^{-k_m}} \left(1 - e^{-\alpha E^{-k_a}}\right) \left(1 - e^{-\beta E^{-k_m}}\right)} \tag{2.39}$$

In equation 2.39 one can see that the figure of merit $\mathrm{SDNR}^2/\mathrm{AGD}$ possesses a characteristic energy dependence. In particular the energy dependence is given by a concave function which consequently attains a maximum at a certain energy which can be seen in figure 2.3. It is well known, that the image formation process in x-ray absorption imaging can be described as combination of point processes [BM04] and a model of the imaging task of detecting a contrast layer in a homogeneous background based on this description can be found in [SH10]. The main differences between the approach described in [SH10] and the approach presented in this work is that our approach gives an explicit analytical expression for a certain figure of merit instead of relying on a numeric evaluation of an expression derived directly from equation 2.35. However, while the approach presented in this work has the advantage of providing a simple analytical expression for a commonly used and easily measurable figure of merit and the advantage of making the dependence on the x-ray energy and on the parameters α, k_a, β and k_m manifest, it is only valid in the limit of a large number of photons. This follows from the use of the central limit theorem which however is also implicitly used in [SH10] for calculations involving a large number of photons.

3 Calculation of the x-ray beam creation with a laser-driven undulator x-ray source

In this chapter the imaging setup considered throughout this work and the laser-driven x-ray source used in that setup is presented together with calculations of the electron beam properties and the x-ray beam properties of this source. Section 3.1 begins with a schematic description of the components of the laser-driven x-ray source and provides a discussion of its advantages over conventional x-ray sources. This is followed in section 3.2 by a description of the electron beam optics used for creating a laminar electron beam. Calculations of the electron dynamics are presented showing that by using an optimized beam optic it is possible to create a laminar beam. Using these results in sections 3.3 and 3.4 calculations of various properties of the x-ray beam are presented and the influence of the undulator parameters and of the electron beam properties on the resulting x-ray beam is quantified. These calculations were performed by using two different methods. The first method used for the investigation of the x-ray beam properties described in section 3.3 deals with the calculation of the total spatio-spectral x-ray distribution in the detector plane resulting from the integrated contributions of all parts of the electron beam inside the undulator. In contrast to this the second method described in section 3.4 is more detailed and is based on sampling the phase space distribution describing the electron beam taking into account the calculation of the spatio-spectral x-ray distribution on the detector for each sampled filament electron beam.

The results of the calculations described in this chapter show that the proposed imaging setup using a laser-driven undulator x-ray source is capable of generating an x-ray beam suitable for mammography. These calculations allow for the analysis of the influence of the x-ray source parameters and of the detection geometry on the image quality which can be found in chapter 6.

3.1 Imaging setup using a laser-driven x-ray source

The purpose of this section is to give a detailed description of the laser-driven undulator x-ray source that is considered to be the reference x-ray source throughout the rest of this work. A first prototype of this type of x-ray source have been constructed by the free-electron laser group at the Ludwig Maximilian University of Munich and

its capability to produce soft x-rays has already been demonstrated [FWP09]. The experimental setup of this source is depicted in figure 3.1 and consists of several parts. The electron acceleration is done by an intense laser pulse, which ionizes the atoms of a gas target and produces a plasma wave that generates large longitudinal electrical fields by which the electrons get accelerated to relativistic energies. This process is called laser wake field acceleration [PMtV02, M04]. The electron optics part consists of two magnetic quadrupole lenses [EGB07] that ensure the collimation and focusing of the electron beam. Because, depending on their parameters, they focus only electrons of a specific energy they also act as energy-band-pass filter, which ensures a small spectral bandwidth and stability in terms of low shot-to-shot fluctuations [FWP09]. They also allow to generate a laminar beam that is spread out in the horizontal direction and highly collimated in the vertical direction. The accelerated electrons pass an undulator which consists of a periodic arrangement of permanent magnets [OMR10]. As described in section 2.1 x-rays are generated inside the undulator resulting from the electrons sinusoidal motion caused by the alternating magnetic field. The electrons thereby emit synchrotron radiation in a narrow cone in the forward direction. The x-ray beam then gets shaped by a slit which filters low-energetic off-axis x-rays and passes the object to be imaged. The purpose of the slit is to filter the low-energetic x-rays thereby ensuring a quasi-monochromatic spectrum, which is discussed in chapter 3.3. Finally the electrons get deflected by a magnetic field onto a beam dump. This type of x-ray source has a number of advantages over conventional x-ray tubes used in radiography today which are discussed in the following paragraphs.

Tunable quasi-monochromatic spectrum: As shown in the last chapter in section 2.1 for a reasonably high number of undulator periods and a small electron deflection parameter $K \ll 1$ the on-axis spectrum is sharply peaked around the fundamental energy as can be seen in equation 2.31. The specific influence of the number of undulator periods and of the remaining parameters on the spectrum are quantified in section 3.3. The fundamental energy of the undulator radiation can be selected by tuning the electron energy to the corresponding value given by the undulator equation 2.20. These two properties allow for the selection of the optimal energy that maximizes the image-quality-to-dose ratio for a specific imaging application. This is discussed for mammography in chapter 6 where the dose reduction opportunities are quantified in section 6.3.

Laminar x-ray beam profile: The second advantage is the precise control of the electron beam and consequently also of the generated x-ray beam. The quadrupole magnets can be used to defocus the electron beam in one direction leading to a horizontally spread out x-ray beam that is perfectly suitable for imaging applications. This laminar beam

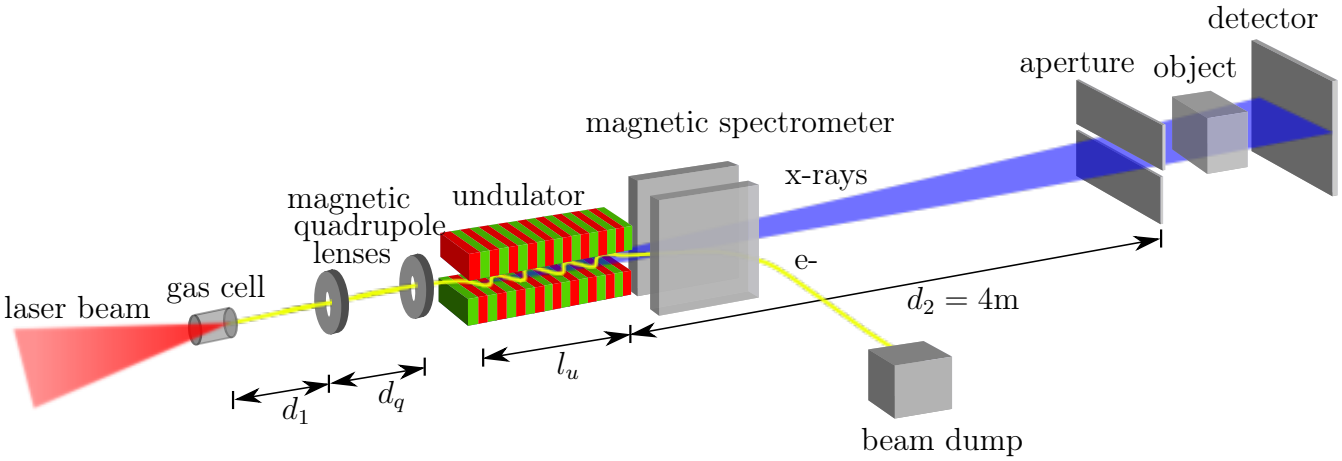

Figure 3.1: Experimental setup of the undulator radiation source: An intense laser beam is focused onto a cell containing hydrogen. Electrons in the gas cell are accelerated by the laser wake field process and are collimated by two miniature quadrupole lenses. The quadrupole lenses focus the electron beam in the vertical direction and defocus it in the horizontal direction thereby creating a laminar beam. Passing the undulator the electrons emit synchrotron radiation and are then deflected by a magnetic field onto a beam dump. The x-ray beam exits the undulator and is shaped by a slit that stops lower energetic x-rays. The remaining x-rays pass the object that is to be imaged and hit the detector.

profile allows the application of a scanning geometry in which the x-ray beam scans in one direction over the object thereby obtaining a full image. This scanning geometry has the advantage that scattered x-rays usually degrading the noise properties in the image are not detected. The impact of this scatter reduction on the image quality is discussed in sub-section 5.2.4. On the other hand, since the x-ray source operates in a pulsed way with a very short pulse length, artifacts caused by the objects movement are eliminated. The source parameters needed for the creation of this laminar beam profile are described in the the next section.

Compact dimensions: Another advantage of this type of source are its compact dimensions based on the fact that the electron acceleration is done on a very small scale using a laboratory sized laser setup and because of the small size of the miniature quadrupole magnets and the undulator consisting of permanent magnets. These source dimensions are in contrast to those of kilometer sized synchrotron x-ray sources. To reach the dimensions of typically used x-ray tubes however further advances in the construction of compact driving lasers would be needed.

Application to new x-ray imaging techniques: Based on the very small bandwidth, the tunability of the fundamental energy and the tightly focused beam there are a number of imaging techniques that can be done using this source. The tunable monochromatic spectrum is optimally suited to be applied to K-edge imaging techniques using contrast agents [DEG92, Gia96]. Another possibility is to apply the scanning geometry together with the focused and monochromatic x-ray beam to scatter imaging techniques. Especially the Rayleigh-to-Compton scatter method [DPB99, SK98] which can differentiate between materials based on their different atomic number could be conducted with this source. Potentially more sensitive imaging of contrast agents could be achieved using fluorescence techniques [YT12] which could even open up the opportunity to perform molecular imaging using high-Z contrast agents [HOD10].

3.2 Beam line setup for the creation of a laminar electron beam

In this section a description of realistic electron beams encountered in experiments is given followed by calculations of how the electron beam can be controlled by magnetic quadrupoles. Thereby it is show that using laser accelerated electrons it is possible to create a laminar electron beam that is spread out in one direction and tightly focused in the perpendicular direction. Also the dependence of the electron beam characteristics on the parameters of the beam optic and of the beam line is quantified.

3.2.1 Phase space description of the electron beam

The electron beam consists of a certain number of electrons each having a certain position and momentum as described by classical mechanics [TH03]. It is not necessary here to differentiate between all microscopic electron configurations but only between classes of electron configurations which belong to certain distributions in the phase space. Therefore it is suitable to describe the electron beam by an electron phase space density that gives the number of electrons per unit phase space volume. The mathematical description of this electron phase space density is given by a measure on phase space with a total measure equal to the number of electrons in the beam [TH03].

Motion of a single electron in an accelerator: In accelerator physics one is interested in controlling the motion of electrons in storage rings transverse to their flight path. This is accomplished by using quadrupole magnets which leads to transverse so called betatron oscillations as shown in [Wil96] (chapter 3.7) and [TH03] (chapter 5.4). The phase space coordinates corresponding to the electrons at a certain longitudinal position in the accelerator depend on the particular arrangement of the magnetic structures along

the flight path and on the electrons initial phase space coordinates. However it can be shown [Wil96] (chapter 3.8) that the phase space coordinates of one electron at a certain longitudinal position s always belong to a set of points in phase space described by an ellipse given by

$$\gamma_{\text{twiss}}(s)\, x^2(s) + 2\alpha_{\text{twiss}}(s)\, x(s)\, x'(s) + \beta_{\text{twiss}}(s)\, x'^2(s) = \varepsilon \tag{3.1}$$

This is the general equation of an ellipse enclosing an area of $\pi\varepsilon$. A plot of the ellipse defined by equation 3.1 is shown in figure 3.2. Here x and x' are the coordinates of one electron in phase space and the parameters α_{twiss}, β_{twiss} and γ_{twiss} depend on the particular structure of the magnetic elements of the accelerator as well as on the initial electron coordinates in phase space.

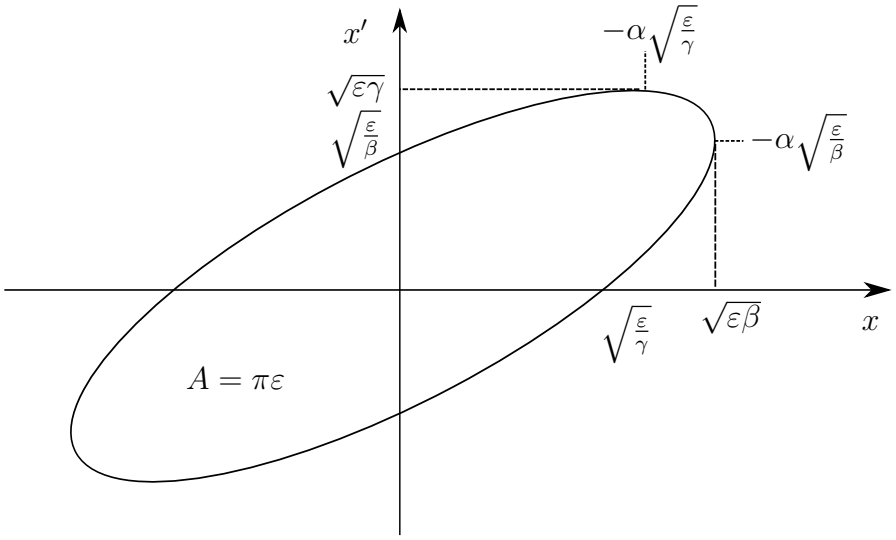

Figure 3.2: The ellipse in phase space described by equation 3.1.

Statistical description of the electron beam: By now only the motion of a single electron has been considered. In order to describe the transverse motion of a thick electron beam consisting of a large number of electrons it is assumed that the phase space distribution corresponding to this beam is of Gaussian shape with respect to both momentum and position in the transverse direction. This phase space distribution is described by a measure on phase space with a total measure normalized to the number of electrons N_e with an associated electron density function ρ. Assuming a Gaussian distribution in phase space and taking $\pi\varepsilon$ to be the area of the ellipse corresponding to the full width at half maximum of ρ one gets

$$\rho(x, x') = \frac{N_e}{2\pi\varepsilon} \exp\left(-\frac{\gamma_{\text{twiss}}}{2\varepsilon}x^2 + \frac{\alpha_{\text{twiss}}}{\varepsilon}xx' - \frac{\beta_{\text{twiss}}}{2\varepsilon}x'^2\right) \tag{3.2}$$

The Twiss parameters can therefore be identified with the moments and the correlation of the phase space distribution as follows

$$\beta_{\text{twiss}} = \sigma_x^2/\varepsilon$$
$$\gamma_{\text{twiss}} = \sigma_{x'}^2/\varepsilon$$

$$\alpha_{\text{twiss}} = -\sqrt{\frac{\sigma_x^2\sigma_{x'}^2}{\varepsilon^2} - 1}$$

where

$$\sigma_x = \sqrt{\langle x^2 \rangle}$$
$$\sigma_{x'} = \sqrt{\langle x'^2 \rangle}$$
$$\sigma_{xx'} = \sqrt{\langle xx' \rangle}$$

and $\langle \cdot \rangle$ denotes taking the expectation value. ε is the so called emittance which can be interpreted as a measure of the spread of the electron distribution in phase space and can be written as

$$\varepsilon = \sqrt{\sigma_x^2\sigma_{x'}^2 - \sigma_{xx'}^4}$$

In the case of a vanishing correlation $\sigma_{xx'}$ the phase space density then takes the simple form:

$$\rho\left(x, x'\right) = \frac{N_e}{2\pi\sigma_x\sigma_{x'}} \exp\left(-\frac{x^2}{2\sigma_x^2} - \frac{x'^2}{2\sigma_x'^2}\right)$$

The phase space coordinates corresponding to a certain electron density again are described by an ellipse as the argument of the exponential in equation 3.2 has the same form as the right side of equation 3.1. Note however that when using equation 3.1 for the FWHM electron density the interpretation of the Twiss parameters have changed from being associated to the motion of a single electron to describing the configuration of a thick electron beam consisting of a potentially large number of electrons.

3.2.2 Electron focusing with magnetic quadrupole lenses

In order to get an x-ray beam suitable for medical imaging applications the electron beam itself has to be controlled. Magnetic quadrupoles have the property of focusing an electron beam in one direction while defocusing in the perpendicular direction [Wil96] and are therefore ideally suited for this task. In this work an arrangement of two magnetic quadrupole lenses was chosen which are positioned accordingly in order to defocus the electrons in the horizontal direction while focusing them in the vertical direction onto the slit plane. The first task in designing a beam line suitable for imaging

applications is therefore to determine the optimal quadrupole parameters resulting in a laminar beam.

3.2.3 Optimization for a laminar beam

Depending on the characteristics of the laser-wake-field acceleration the electrons entering the beam line have a set of initial parameters. In this work the following electron source parameters are assumed.

Electron Source parameters:

- Source size: 1 µm
- Emittance (geometric, vertical and horizontal): 1 µm mrad

These electron source parameters can be estimated from experiments [FWP09] and were assumed to be fixed throughout this work. The electron energy however is assumed to be selectable in the range of 3.3 GeV up to 3.7 GeV. The other variable parameters that influence the electron beam are the beam line parameters described in the next paragraph.

Beam line parameters:

- Drift d_1 to the first quadrupole: During this drift the electron beam diverges because of its finite emittance.
- Length l_{q1} of the first quadrupole: The first quadrupole focuses the electron beam in the vertical direction while defocusing it in the horizontal direction.
- Drift d_q between quadrupoles: During this free drift the electrons converge in the vertical direction while diverging in the horizontal direction. This is needed in order to achieve a strong focusing of the beam in the second quadrupole lens.
- Length l_{q2} of the second quadrupole: The second quadrupole leads to the electron being slightly defocused in the vertical direction and horizontally focused on the undulator center.
- Quadrupole magnetic field gradients: The field gradient of the quadrupoles is assumed to be 500 T/m.
- Drift after undulator exit: The free drift after the undulator exit is assumed to be 4 m in order to ensure a horizontal beam size of a few cm.

As the goal is to create a laminar beam there are two conditions that have to be met. At first the beam should be horizontally focused on the undulator center which results in the electron beam being horizontally defocused after the drift to the detector. Secondly the electron beam should be vertically focused onto the slit plane as this enables the efficient filtering of the off-axis parts of the spectrum by the slit. The optimization problem of finding the beam line parameters that result in these conditions being fulfilled has to be solved while still respecting all boundary parameters as the quadrupole aperture size and the undulator gap size. In order to solve this problem the optimization algorithms provided by the beam physics code COSY Infinity [MB99] were used. As described in [Ber90] (section 7.1) there are a number of different optimization algorithms including an implementation of the simplex algorithm [Dan98], which has been chosen here in order to find the optimal beam line parameters. This was done by assuming a fixed length $l_{q_2,\max}$ of the second quadrupole lens together with setting all other parameters to reasonable initial values and then using the optimization algorithm for minimizing the cost function c defined by

$$c\left(x_h, x_v, l_{q_1}, r_{q_2}\right) = \frac{x_v^{\alpha}}{x_h} + b\left(l_{q_1}, l_{q_1,\max}\right) + b\left(r_{q_2}, r_{q_2,\max}\right) \tag{3.3}$$

where x_h and x_v are the horizontal and vertical r.m.s. beam dimensions in the slit plane, l_{q_1} is the length of the first quadrupole and r_{q_2} is the r.m.s. beam size in the second quadrupole. The boundary function b is defined as

$$b\left(x, x_{\max}\right) = \exp\left(\frac{x - x_{\max}}{x_{\max}}\right)$$

and ensures that the beam parameters stay below the boundary values given by

$$l_{q_1,\max} < l_{q_2,\max} \quad \text{and} \quad r_{q_2,\max} < 6 \text{ mm}$$

The quadrupole aperture width should then be several times $r_{q_2,\max}$ for being able to focus the whole beam. The free parameter $\alpha < 1$ in equation 3.3 is necessary in order to weight the vertical focusing less than the horizontal defocusing, as the vertical beam size needs only be sufficiently small for the filtering of the off-axis photons by the slit. Because of the $\frac{x_v}{x_h}$ term in equation 3.3 this cost function maximizes the ratio of the horizontal beam size to the vertical beam size in the slit plane leading to a laminar beam profile. The optimization algorithm was used to find the optimal values of the beam line parameters l_{q1}, d_1 and d_q which minimize the cost function. These beam line parameters are shown for different lengths of the first quadrupole in table 3.1 together with the resulting horizontal size of the beam in the slit plane. There it can be seen

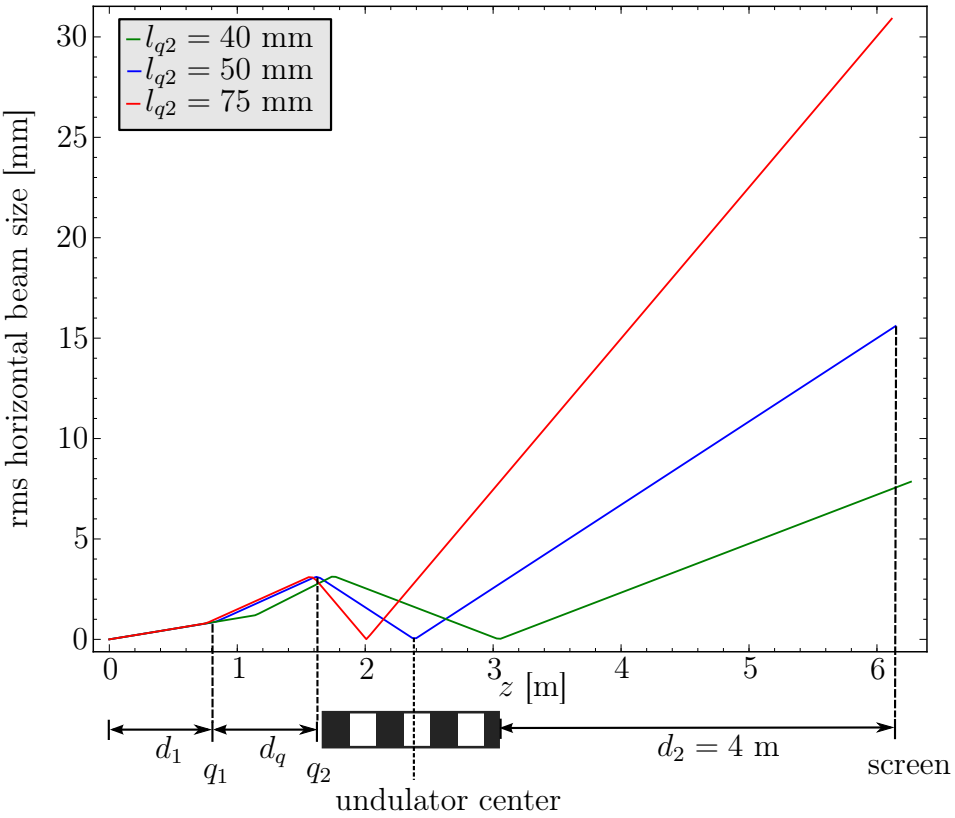

Figure 3.3: Horizontal r.m.s. beam envelope for different values of the length l_{q2} of the second quadrupole lens. The electron energy spread has been neglected and an electron energy of 3.3 GeV has been assumed.

that the length of the second quadrupole is the critical factor for obtaining a laminar beam. If the quadrupole length is too small the beam is only slightly defocused in the horizontal direction.

After the optimal beam line parameters were found, the electron motion was calculated with the beam line simulation tool GPT (General Particle Tracer)[vdGdL98] which is capable of tracking a large number of electrons through arbitrary electromagnetic fields and beam optic components. These calculations enabled us to determine the horizontal and vertical beam envelope which is shown in figure 3.3 and figure 3.4.

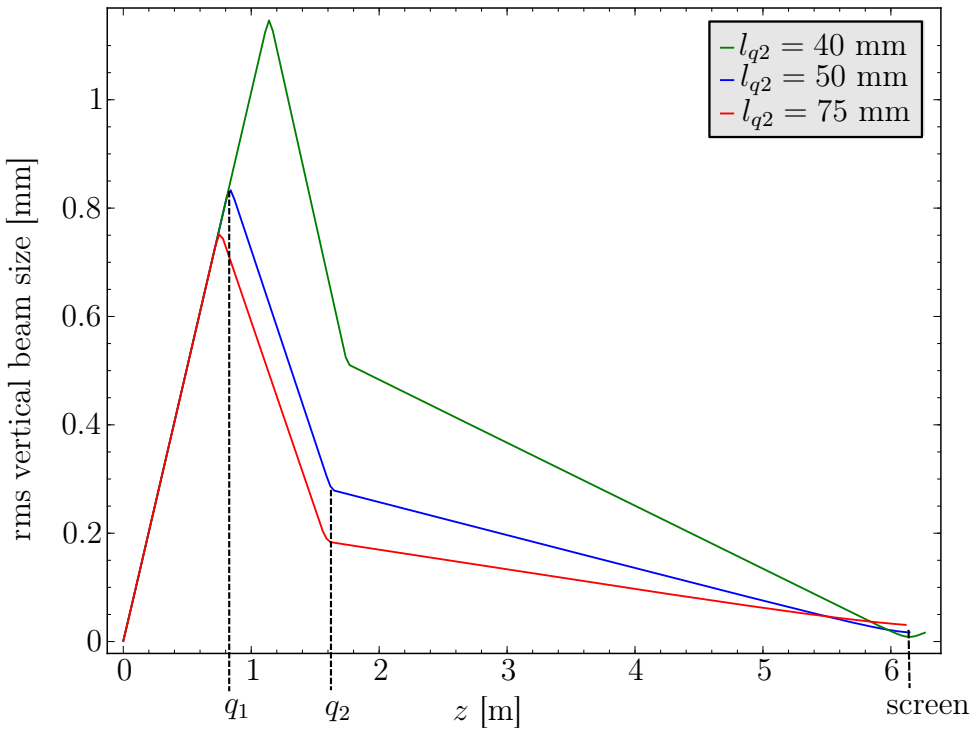

Figure 3.4: Vertical r.m.s. beam envelope for different values of the length l_{q2} of the second quadrupole lens. The electron energy spread has been neglected and an electron energy of 3.3 GeV has been assumed.

l_{q2} [mm]	l_{q1} [mm]	d_1 [m]	d_q [m]	r.m.s. hor. beam size [mm]
40	40	1.0	0.69	8.7
50	45	0.86	0.71	14
75	48	0.82	0.72	28
100	63	0.49	0.91	42

Table 3.1: Horizontal r.m.s. spot size for different values of the quadrupole lengths $l_{q1,2}$ and their corresponding positions.

3.2.4 Influence of the electron energy spread on the laminar beam

Although it has been demonstrated that laser-wakefield electron acceleration schemes can produce relatively high quality electron beams with respect to divergence and energy spread [FWP09, LNG06] it is still important to consider the effects of a small electron energy spread as this could prohibit the production of quasi-monochromatic x-ray beams. Therefore the electron motion through the beam optic was calculated for different energy offsets around the optimal focused energy. The effect of this energy offset on the electron focusing is shown in figure 3.5 and figure 3.6 where the r.m.s. horizontal and vertical electron beam size is plotted against the longitudinal position in the beam line for different energy offsets. As the electron beam is strongly defocused in the horizontal direction the effect of the energy spread is negligible there. However as the electron beam is focused in the vertical direction onto the detector plane even a small electron energy offset is important there. Owing to the focusing properties of the magnetic quadrupole lenses electrons with an energy offset from the optimal focused energy are strongly defocused which leads to the electron optic acting as a band pass filter with respect to the on-axis electron energy [FWP09]. Consequently when only the focused on-axis electrons are used for the x-ray generation in the undulator the electron energy spread should not prohibit the creation of a nearly monoenergetic x-ray beam. Nevertheless when considering the x-rays produced by the whole beam inside the undulator, the electron energy spread leads to a broadening of the x-ray spectrum even for the on-axis x-rays as shown in sub-section 3.3.4. From the calculations of the electron motion through the beam line one can easily obtain the Twiss parameters introduced in sub-section 3.2.1 for every longitudinal position of the electrons in the beam line. These parameters describing the statistical properties of the electron beam can then be used in order to calculate the undulator radiation which is shown in the next section.

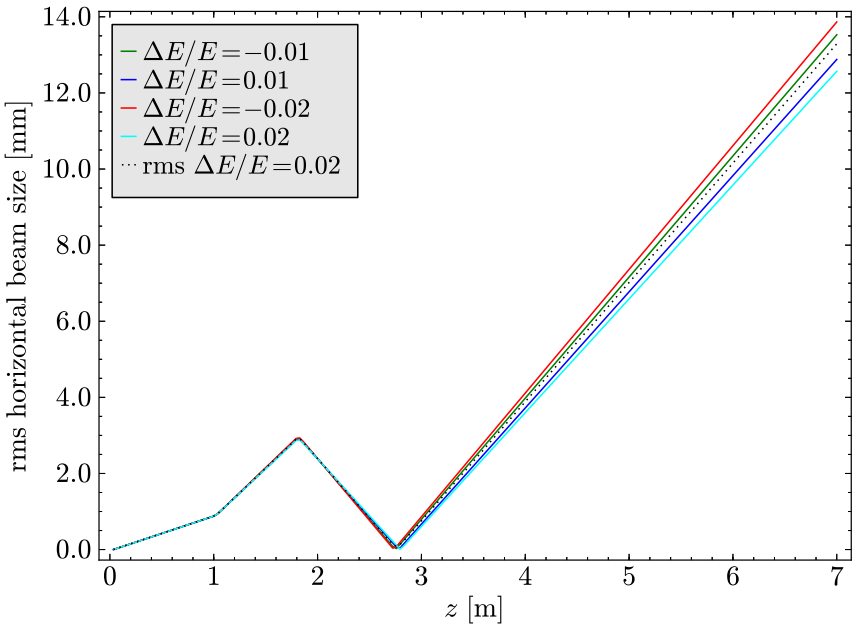

Figure 3.5: Plot of the horizontal r.m.s. beam size against the longitudinal position z for different values of the electron energy together with a plot of the horizontal r.m.s. beam size for a beam with a relative electron energy spread of 0.02. The length of the second quadrupole l_{q2} has been set to $l_{q2} = 50$ mm.

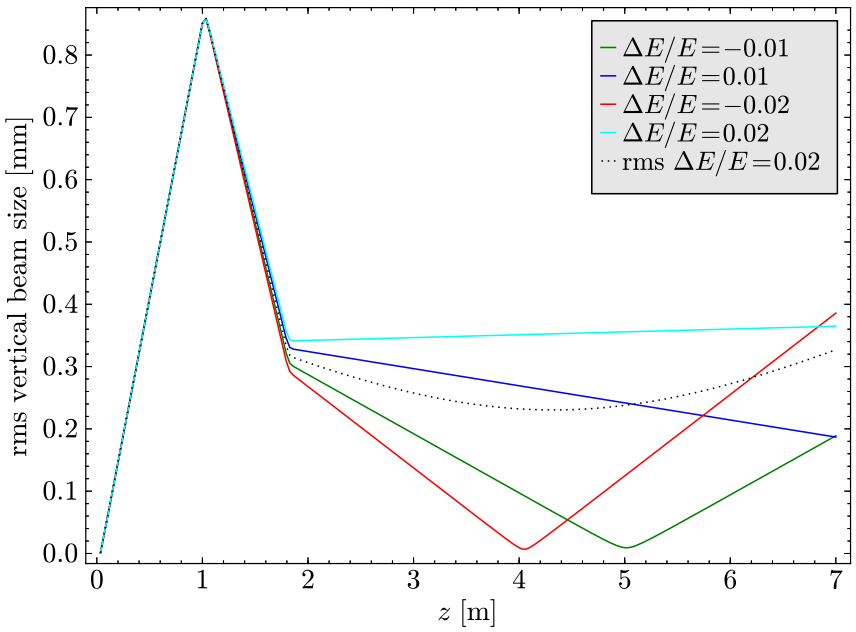

Figure 3.6: Plot of the vertical r.m.s. beam size against the longitudinal position z for different values of the electron energy together with a plot of the vertical r.m.s. beam size for a beam with a relative electron energy spread of 0.02. The length of the second quadrupole l_{q2} has been set to $l_{q2} = 50$ mm.

3.3 Influence of the x-ray source parameters on the spatio-spectral photon flux distribution

Before simulating the image formation and dose deposition process in x-ray imaging using a laser-driven undulator x-ray source is possible and for the optimization of the image quality to dose ratio the most basic prerequisite is the characterization of the spectral properties of this source. Therefore in this section the spatio-spectral x-ray distribution in the detector plane is investigated for different parameters of the undulator x-ray source. Specifically the influence of the undulator parameters, of the electron beam parameters and of the detection geometry on the spatio-spectral x-ray radiation distribution is quantified. The calculations of the undulator radiation described in this section were done using the well established Synchrotron Radiation Workshop (SRW) code [CE98]. This code numerically evaluates either the near-field equation 2.5 or alternatively the equation for the far-field approximation given by equations 2.7 and 2.25, which is less precise but computationally less expensive. The far-field approximation as implemented by this code was specifically used in this section in order to calculate the spatio-spectral distribution of the undulator radiation passing through a slit and being recorded on the detector. This was done by using the previously calculated properties of the electron beam described in section 3.2. Specifically the Twiss parameters describing the electron distribution in phase space as described in subsection 3.2.1 were used as an input for the SRW code.

3.3.1 On-axis spectrum for zero emittance and zero electron energy spread

As described in the previous chapter in section 2.1, neglecting emittance effects as well as the electron energy spread and assuming a reasonably high number of undulator periods, the on-axis spectrum is sharply peaked around the x-ray energy corresponding to the fundamental wavelength and with less intensity also at the higher harmonic wavelengths. The on-axis x-ray spectrum resulting from these idealized parameters is shown in figure 3.7. The fundamental x-ray energy is proportional to the square of the electron energy as can be seen in the fundamental undulator equation 2.20. As shown in section 2.1.7 the spectrum mainly consists of the fundamental and the contribution of the higher harmonics is very small if the deflection parameter is small ($K < 1$). Also one can see in figure 3.7 that the even harmonics do not contribute to the on-axis spectrum which is consistent with the explanation previously offered in sub-section 2.1.6. However when considering a less idealized model, there are several effects, governed by the source parameters, that have an influence on the x-ray spectrum most importantly leading to a widening of the peaked energy distribution. In order to quantify the influence of

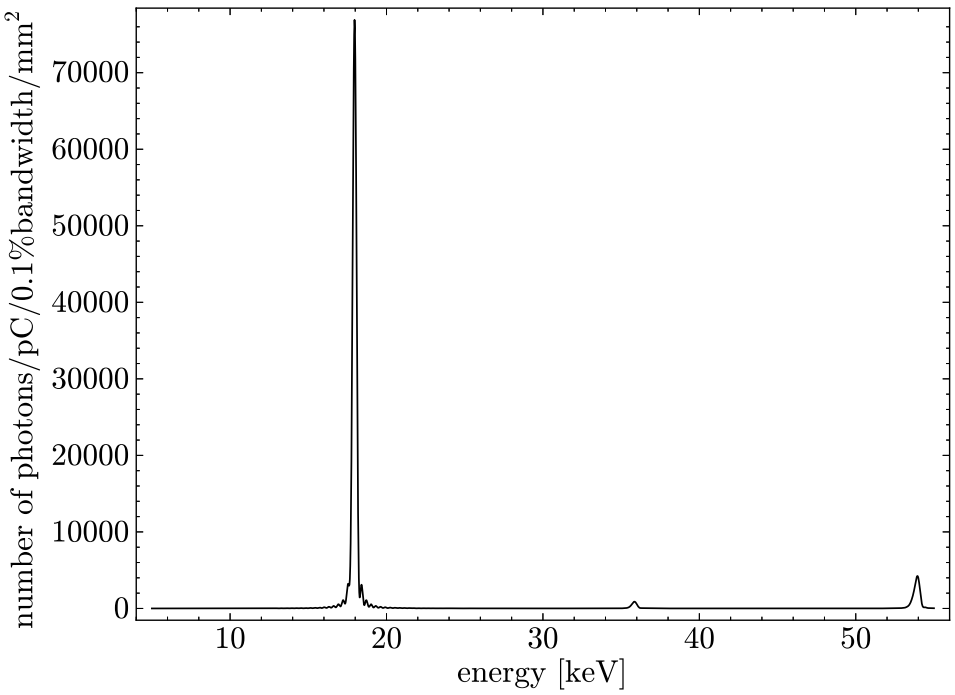

Figure 3.7: On-axis spectral photon flux density for a filament electron beam with an energy of 3.314 GeV without energy spread. The number of undulator periods is 60 at a period length of 5 mm and the magnetic field strength is assumed to be 1.2 T. The flux is collected over small area of 100×100 µm^2 in order to only have on-axis x-rays in the spectrum.

these parameters separately the spectrum of the undulator radiation was calculated for different values of each of these parameters while holding the other parameters fixed.

3.3.2 Influence of the number of undulator periods

The most basic influence of the number of undulator periods is the linear increase of the total number of photons in the beam with an increasing number of periods as can be seen in equation 2.33. However the number of undulator periods also influences the spectral bandwidth in two ways. At first the spectral on-axis bandwidth becomes smaller with an increasing number of periods due to the interference of photons generated in each period and as estimated by equation 2.21 is inversely proportional to the number of undulator periods. The on-axis spectrum around the fundamental photon energy is plotted in figure 3.8 for different values of the number of undulator periods. There it can be seen that for a reasonably high number of undulator periods the spectrum is quasi-monochromatic.

Additionally also the angular spectral distribution is influenced by the number of undulator periods. According to equation 2.24 for a higher number of periods more

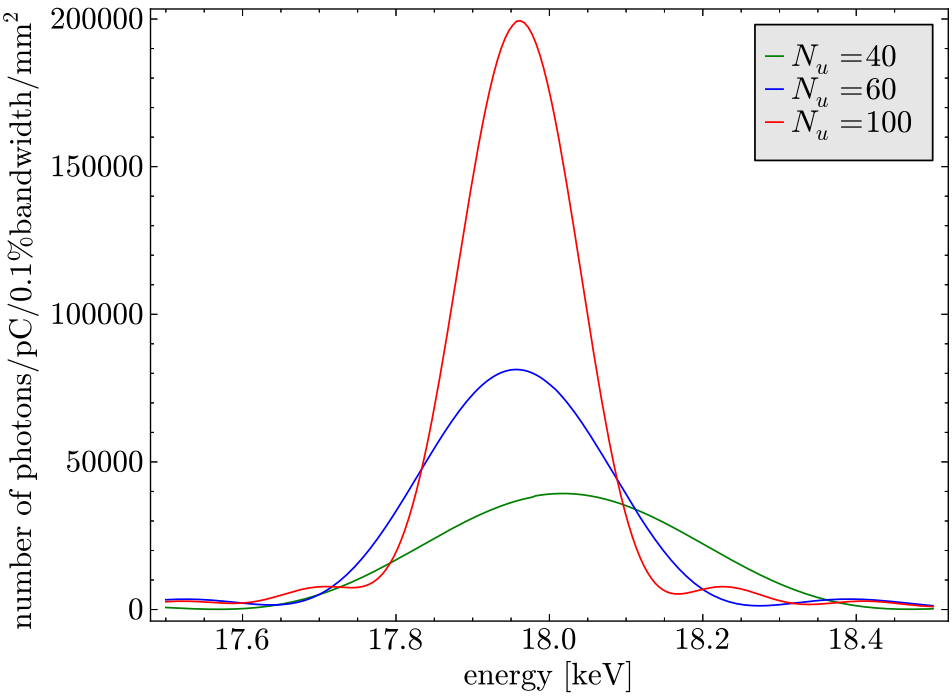

Figure 3.8: On-axis spectral photon flux density around the fundamental energy for different values of the number of undulator periods N_u resulting from a filament electron beam without energy spread. The flux is collected over an area of 100×100 µm^2 . An electron energy of 3.314 GeV was chosen in order to have a peak flux at 18 keV. The magnetic field is assumed to have a field strength of 1.2 T and a period length of 5 mm.

photons are emitted on-axis and the number of off-axis photons decreases. Together with the angular energy dependence of the photon energy described by the fundamental undulator equation 2.20 this also leads to a decreasing total spectral bandwidth with an increasing number of periods. This can be observed in figure 3.9 which shows two density plots of the photon flux against the transversal position on the detector and the photon energy. There it can be seen that the off-axis photon energy decreases according to equation 2.20 and it can also be seen that for a higher number of undulator periods this off-axis contributions are smaller and most photons are emitted on-axis.

3.3.3 Emittance effects: Influence of the slit width and of the off-axis contributions

As the angular dependence of the photon energy, shown in figure 3.9, already exists for a filament electron beam these off-axis contributions therefore are always present in a laminar beam that has a finite emittance. However for a finite emittance beam

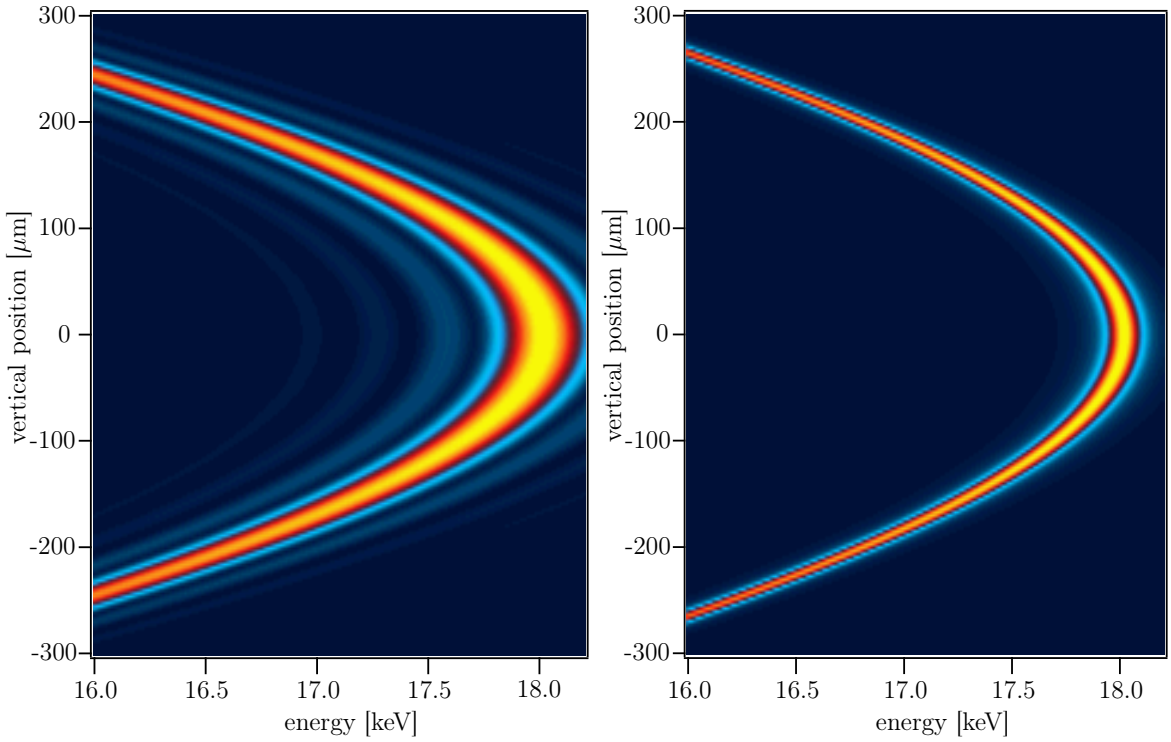

Figure 3.9: Density plot of the spectral photon flux plotted against the photon energy and the transversal detector position around the fundamental energy. (a) shows the flux plotted for 30 undulator periods while (b) shows the plot for 100 undulator periods. The electron energy was set to 3.314 GeV and the electron energy spread has been neglected.

the angular dependence, quantified by equation 2.20, gets smeared over a certain area depending on the value of the beam emittance as in this case the x-ray beam can be described by a convolution of the x-rays produced by a filament electron beam with the electron phase space distribution introduced in sub-section 3.2.1 and defined by equation 3.2.

As shown in the previous sub-section the number of lower energetic off-axis photons decreases with an increasing number of undulator periods. However for a moderate number of periods $N_u < 100$ there are still contributions of lower energetic x-rays in the spectrum and as a higher number of undulator periods becomes impractical it is reasonable to use a slit in order to filter out these x-rays. The slit is designed to block the lower energetic off-axis x-rays only in the vertical direction and is open in the horizontal direction because the laminar beam is spread out in the horizontal direction as can be seen in figure 3.10. This consequently allows x-rays that are horizontally off-axis to pass the slit under a higher angle and hence with lower energy. The contribution of x-rays that are only horizontally off axis is always present in the spectrum and independent

from the slit width as can be seen in the on-axis line-out in figure 3.12. Also these horizontally off-axis x-rays are relatively uniformly distributed as can be seen in figure 3.11 which is a result of the high horizontal divergence of the laminar beam. Therefore the spatio-spectral distribution does show a characteristic energy-to-position dependence only in the vertical direction.

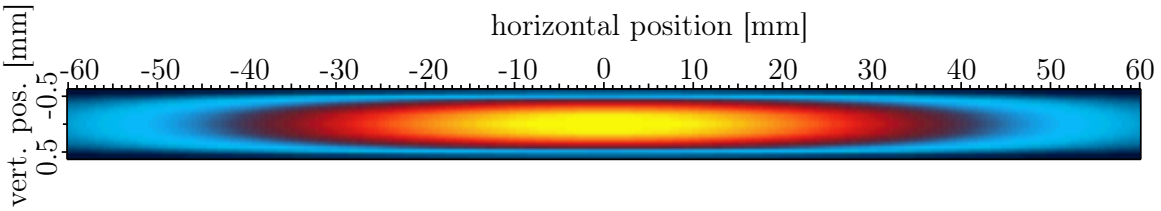

Figure 3.10: Beam profile: Density plot of the total integrated flux in the detector plane. Note the different scaling of the horizontal and vertical axis.

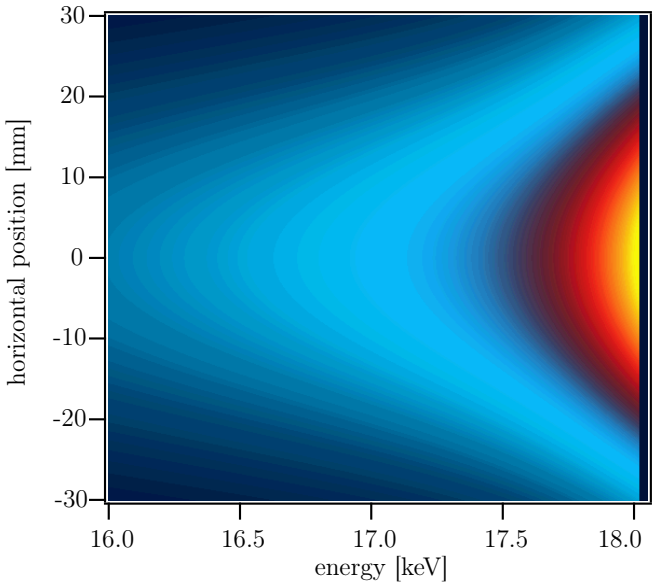

Figure 3.11: Density plot of the x-ray energy against the horizontal position in the detector plane at vertical position $x_v = 0$.

The contribution of horizontally off-axis x-rays passing the slit is small as one can see in the plot of the on-axis spectrum in figure 3.12 but as the width of the slit increases, also more x-rays that are detected vertically off-axis can pass. Because the off-axis x-rays have a lower energy due to the fundamental undulator equation 2.20 the bandwidth of the total spectrum increases as the slit width increases, as can be seen in figure 3.13.

The number of photons and the energy distribution of the off-axis x-rays that pass the slit is also governed by the Twiss parameters of the finite emittance beam and is

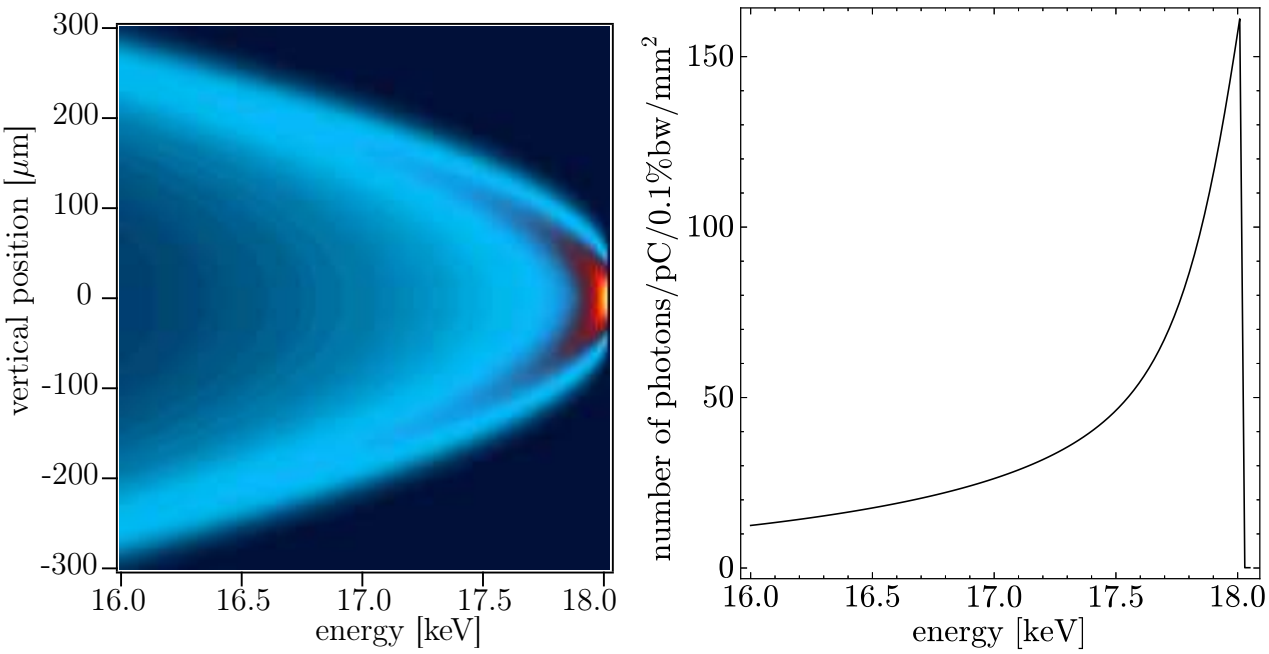

Figure 3.12: Left: Density plot of the spectral photon flux against the photon energy and the vertical position in the detector plane at the horizontal position $x_h = 0$. The number of undulator periods is 60 at period length of 5 mm and the magnetic field strength is assumed to be 1.2 T. The (geometric) emittance of the electron beam is set to a value of 1 µm mrad. The electron energy is assumed to be 3.314 GeV and the electron energy spread has been neglected here. Right: On-axis (x_v=0) line-out of the spectral photon flux density where the flux is collected over an area of 100×100 µm^2 at a distance of 4 m from the undulator exit.

optimized by choosing the right Twiss parameters leading to a laminar beam that is focused exactly on the slit-plane. This ensures that lower energetic x-rays that are vertically off-axis can be filtered by the slit. In order to estimate the influence of the slit width the spectrum around the fundamental energy was calculated and the results for different values of the slit width are shown in figure 3.13. There it can be seen that the slit width has to be below 0.5 mm in oder to obtain a quasi-monochromatic spectrum.

3.3.4 Influence of the electron energy spread

There is also the influence of the electron energy spread which influences the angular spectral x-ray distribution in a number of ways. At first the undulator equation 2.20 describing the fundamental x-ray energy depends on the electron energy which directly leads to a broadening of the x-ray spectrum at an increased energy spread. The on-axis spectrum for a filament electron beam, ignoring emittance effects, is shown in figure 3.14

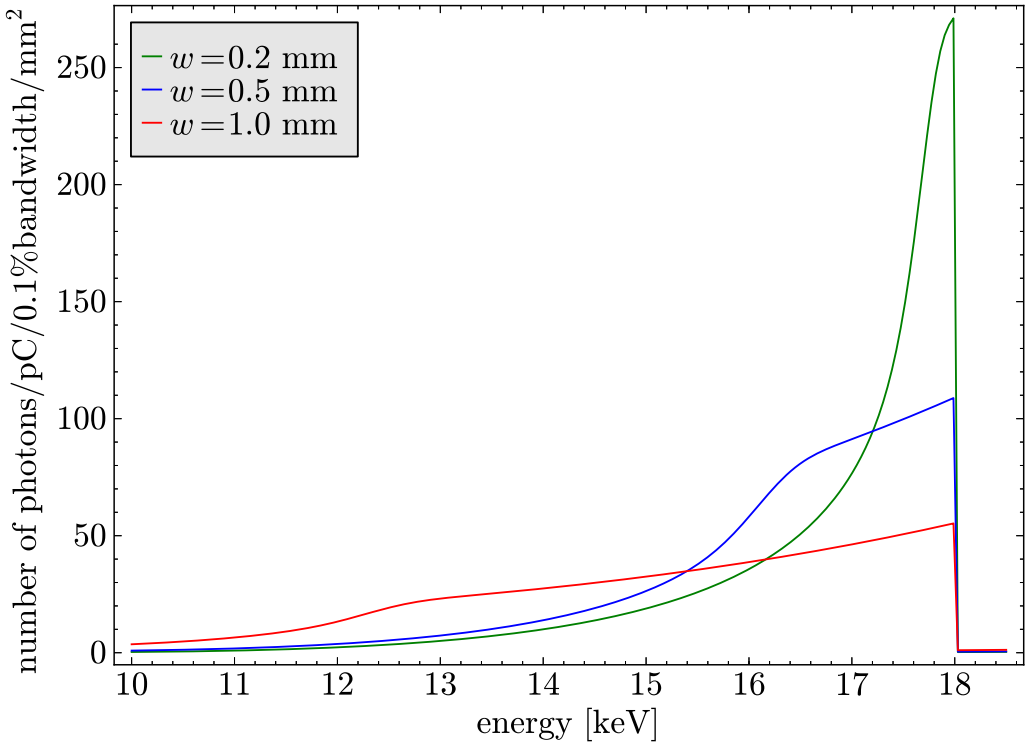

Figure 3.13: Photon flux density around the fundamental energy averaged over the whole slit area for different values of the slit width w. The (geometric) emittance of the electron beam is set to a value of 1 µm mrad. In order to quantify the influence of the slit width alone the energy spread of the electrons has been neglected here. Their energy is assumed to be 3.314 GeV. The flux density values in this plot correspond to an undulator length of 1 m at an undulator period of 5 mm and a magnetic field strength of 1.2 T. The flux is collected over 4 cm in the horizontal direction and over the whole slit width in the vertical direction at a distance of 4 m from the undulator exit.

for different values of the electron energy spread.

Secondly the angular spread of the beam is inversely proportional to the electron energy as can be seen in equation 2.24. As an increasing angular spread translates directly into an increasing spectral bandwidth lower electron energies contribute more to the spectral bandwidth due to more off-axis photons being present in the beam. More importantly however as the electron optic can only optimally focus a certain electron energy as described in sub-section 3.2.4 there is an additional angular spread due to electrons that are out of focus. For a laminar beam this effect has to be combined with the emittance effects described in the previous sub-section. As the laminar beam already is highly divergent in the horizontal direction the electron energy spread can be neglected there. However as the beam is focused in the vertical direction the electron energy spread

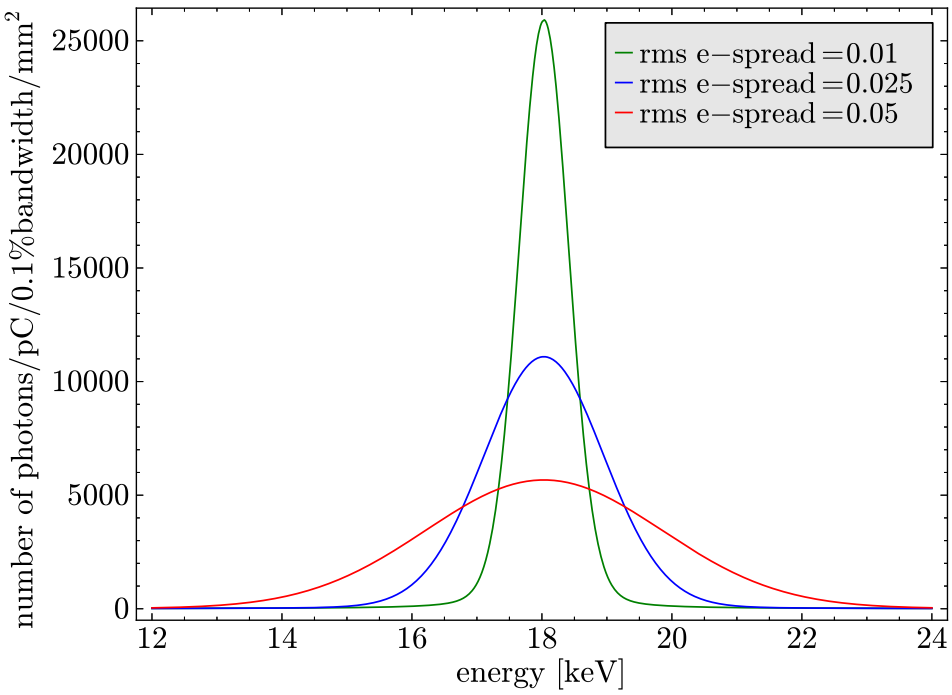

Figure 3.14: On-axis photon flux density for different values of the electron energy spread for a filament electron beam with a mean energy of 3.314 GeV. The number of undulator periods is 60 for a period length of 5 mm and the magnetic field strength is assumed to be 1.2 T. The flux is collected over an area of 100×100 µm^2 at a distance of 4 m from the undulator exit. All emittance effects have been neglected here.

is a critical factor that threatens the method of filtering the vertically off-axis photons described in the last sub-section. Taking into account the laminar beam geometry and the calculation of the electron focusing described in sub-section 3.2.4 the spatio-spectral x-ray distribution in the detector plane can be determined for a laminar beam with finite emittance and finite electron energy spread. In order to calculate this distribution the electron beam calculations described in sub-section 3.2.4 were used and a convolution of the x-ray distribution on the detector depending on the electron energy with the electron beam distribution corresponding to a certain r.m.s electron energy spread has been used. Figure 3.15 shows the spatio-spectral x-ray distribution on the detector with respect to the vertical detector position for an r.m.s. electron energy spread of 1% and together with figure 3.16 is the analogue for the plot shown in figure 3.12 corresponding to zero electron energy spread.

In summary there are three main parameters of the undulator x-ray source that influence the spectral width around the fundamental x-ray energy: the number of undulator

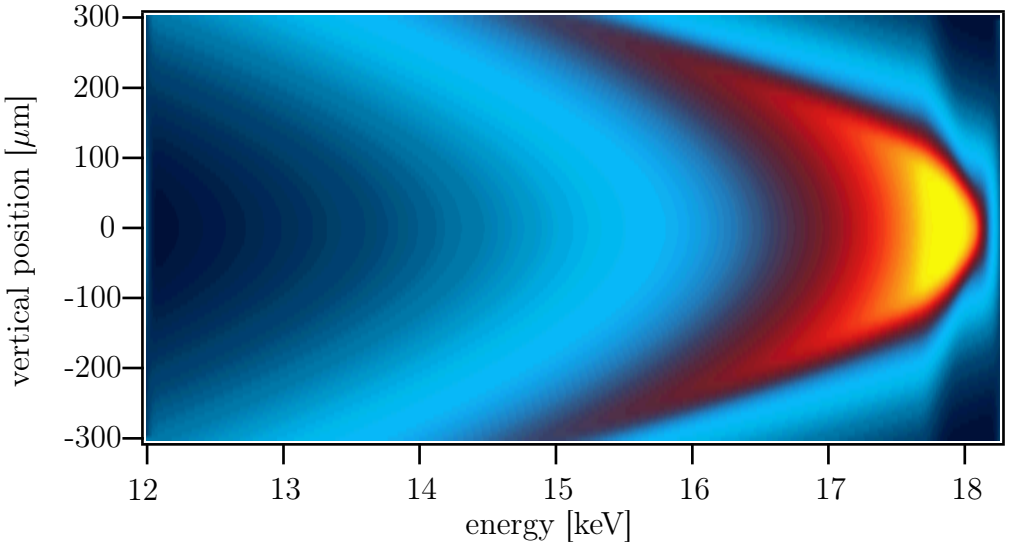

Figure 3.15: Density plot of the photon flux against the vertical detector position and against the photon energy for an r.m.s. electron energy spread of 1%. The number of undulator periods is 60 at period length of 5 mm and the magnetic field strength is assumed to be 1.2 T. The (geometric) emittance of the electron beam is set to a value of 1 µm mrad.

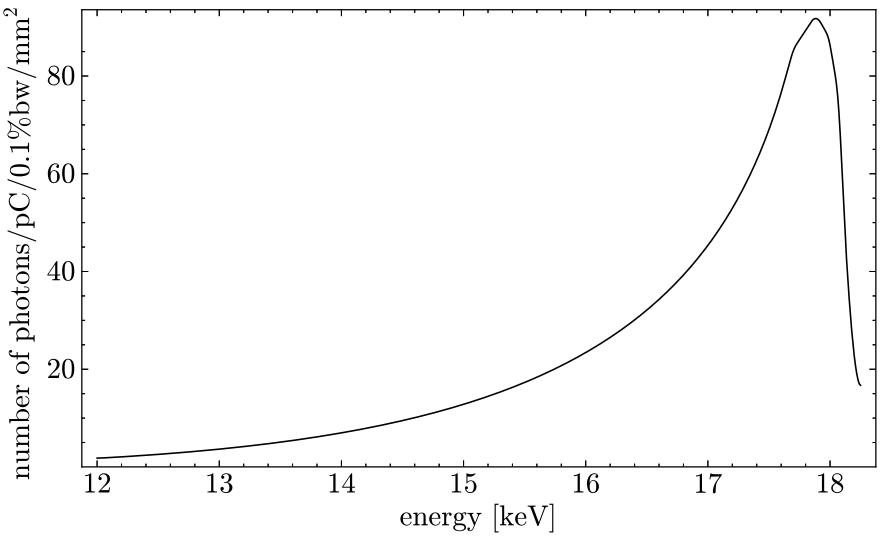

Figure 3.16: On-axis (x_v=0) line-out of the spectral photon flux density where the flux is collected over over an area of 100×100 µm^2 at a distance of 4 m from the undulator exit. The undulator parameters are the same as in figure 3.15.

periods the electron energy spread and the slit width. By comparing the influence of the number of undulator periods and of the slit width it is clear that if the number of undulator periods is reasonably high its influence on the total spectrum is negligible when

compared to the spectral widening due to the slit width, which is the critical factor. The impact of the number of undulator periods and of the slit width on the image-quality-to-dose ratio in x-ray absorption imaging is discussed later in the sub-sections 6.2.1 and 6.2.2.

3.3.5 Higher harmonics: Influence of the magnetic field strength

Another important parameter that influences the x-ray spectrum is the magnetic field strength inside the undulator. In equation 2.33 one can see that the total photon flux corresponding to the fundamental mode increases with increasing deflection parameter K and therefore with increasing magnetic field strength. Also the location of the peaks in the spectrum is influenced by the magnetic field strength, according to equation 2.20. These two effects can be seen in figure 3.17 where the spectrum is plotted for different values of the magnetic field strength. More importantly however, also the flux of the higher harmonics relative to the fundamental is influenced by the deflection parameter K and therefore by the magnetic field strength which is shown in figure 3.18. There it can be seen that the number of photons contained in the second and third harmonic relative to the number of photons contained in the fundamental rises rapidly with increasing magnetic field strength. This becomes a critical factor in x-ray imaging as the photons of the higher harmonics lead to a high level of noise without producing contrast in the image. The impact of the x-rays of the higher harmonics on the image quality to dose ratio is discussed later in sub-section 6.2.3.

3.4 A more detailed calculation of the x-ray beam

In the previous section only the integrated contributions of all parts of the electron beam to the spatio-spectral x-ray distribution in the detector plane have been taken into account. Therefore these calculations provide no information about the angular and spectral flux distribution of x-rays produced at individual points inside the undulator. However this information is needed in order to get a more complete picture of the x-ray beam and in order to investigate then influence of the beam geometry, of the source size and of the energy dependent beam divergence on the image quality in x-ray absorption imaging. There the energy dependent divergence together with the finite source size of the laminar x-ray beam is a critical factor for the spatial resolution one can achieve. Also the detailed calculation of the angular spectral x-ray distribution is a prerequisite for investigating the effect of angular filters on the spectrum as done in section 6.4.

In section 3.2 the electron beam has been described as a distribution in phase space parameterized by the Twiss parameters $\alpha_{h,v}$, $\beta_{h,v}$ and $\gamma_{h,v}$, as defined by equation 3.2, and the influence of the beam optic on this distribution has been discussed. In order to get as much information as possible about the x-ray beam generated by the electron

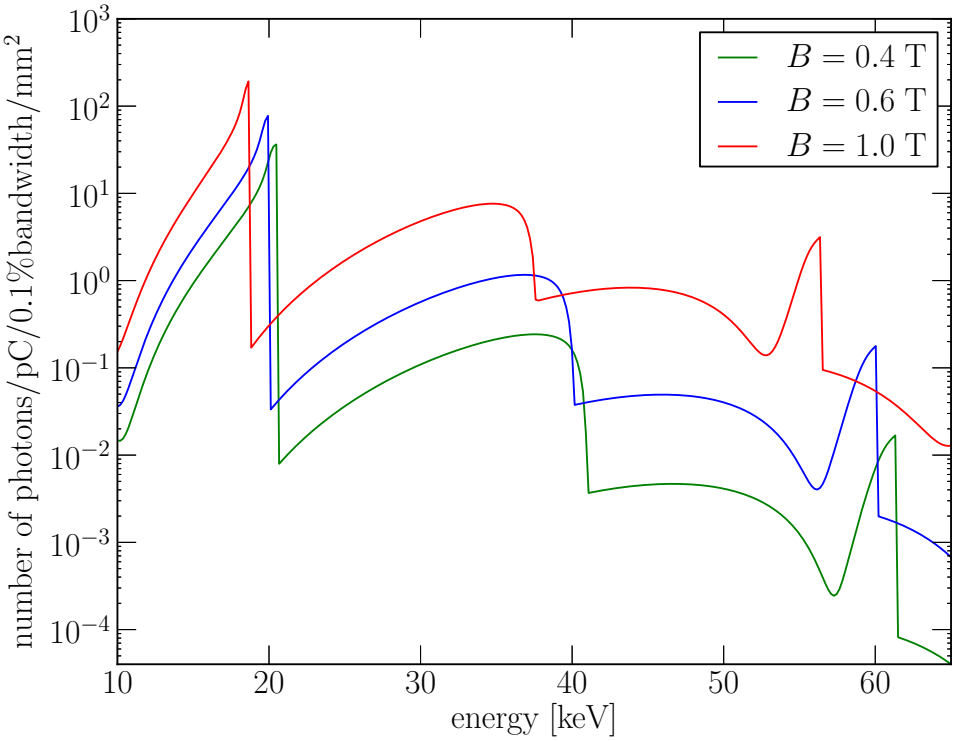

Figure 3.17: Logarithmic plot of the photon flux per bandwidth against the x-ray energy for three different values of the magnetic field strength B. A slit width of 0.2 mm and the limit of an infinite number of undulator periods is assumed, the energy spread of the electrons is neglected and their energy is assumed to be 3.314 GeV. The flux values in this plot correspond to an undulator length of 1 m with an undulator period length of 5 mm and an electron current of 1 A. The flux is collected over 4 cm in the horizontal direction.

beam inside the undulator a method is used that is based on sampling the phase space distribution of the thick electron beam inside the undulator and calculating the spatial and spectral x-ray distribution in the detector plane for each sampled filament part of the electron beam. The contributions from these filament electron beams to the total spatio-spectral x-ray distribution are then (incoherently) added neglecting any interference effects.

The sampling procedure is constructed as follows: At first the undulator is divided longitudinally in n_l parts and for each part the Twiss parameters of the previously calculated horizontal and vertical electron phase space distribution are determined. Then for each longitudinal part the horizontal as well as the vertical phase space distribution is sampled at $n_h = n_{\beta_h} \times n_{\gamma_h}$ and $n_v = n_{\beta_v} \times n_{\gamma_v}$ points respectively. In accordance with the description in sub-section 3.2.1 the phase space distribution describing the electron

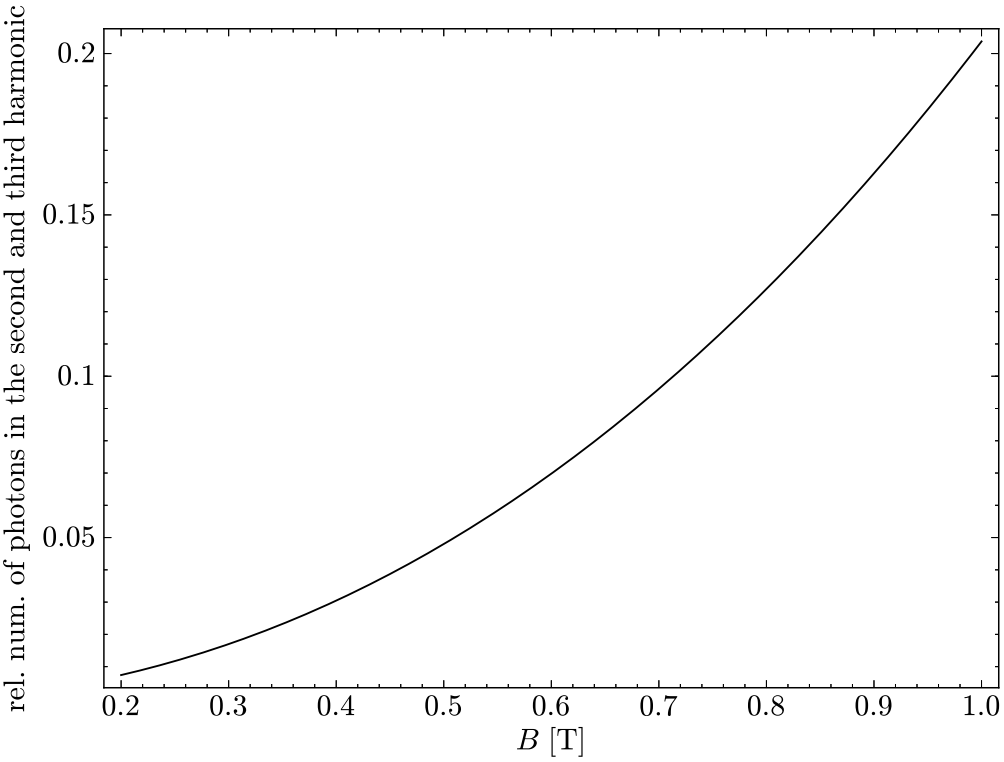

Figure 3.18: Ratio of the photon flux in the second and third harmonic to the photon flux in the fundamental.

beam here is assumed to be a Gaussian both in the horizontal as well as in the vertical phase space. Therefore the electron phase space density depending on the phase space coordinates x_h, x'_h, x_v, x'_v is given by

$$I\left(x_h, x'_h, x_v, x'_v\right) = I_h\left(x_h, x'_h\right) \times I_v\left(x_v, x'_v\right)$$

where

$$I_{h,v}\left(x_{h,v}, x'_{h,v}\right) = \exp\left(-\left(\frac{\gamma_{h,v}}{2\varepsilon}x_{h,v}^2 + \frac{\alpha_{h,v}}{\varepsilon}x_{h,v}x'_{h,v} + \frac{\beta_{h,v}}{2\varepsilon}x'^2_{h,v}\right)\right).$$

which follows from the ellipse equation 3.1. The position coordinates $x_{h,v}$ are sampled in the interval between

$$x_{h,v,\min} = 0 \text{ and } x_{h,v,\max} = 4.7\sqrt{\varepsilon\beta_{h,v}}$$

which corresponds to a distance of two times the full width at half maximum from the peak phase space density. The sampling has been done only for positive values of the horizontal and vertical position as the electron distribution is symmetric with respect to the horizontal and vertical axis. The velocity coordinates $x'_{h,v}$ are sampled between

$$x'_{h,v,\min,\max}(x_{h,v}) = \pm\frac{4.7}{\beta_{h,v}}\left(-\alpha x_{h,v} + \sqrt{\alpha_{h,v}^2 x_{h,v}^2 - \beta_{h,v}\left(\gamma_{h,v} x_{h,v}^2 - 2\varepsilon\right)}\right)$$

which follows from the fact that the electron phase space density corresponding to a distance of two times the full width at half maximum from the peak electron phase space density has the shape of an ellipse as can be seen in figure 3.19 (a) where the electron phase space distribution at a certain longitudinal position in the undulator is shown. Then for each of the $n_l \times n_h \times n_v$ sampled coordinates the spatial and spectral x-ray distribution in the detector plane is calculated for a filament electron beam whose current is proportional to the electron phase space intensity I and is sampled at n_E energies and $n_x \times n_y$ points on the detector. The contribution of a single filament electron beam to the spatial x-ray distribution on the detector for a certain energy interval can be seen in figure 3.19 (b) and in figure 3.19 (c) a density plot of the vertical-spectral flux distribution on the detector for the same filament electron beam corresponding to one sampled point of the phase space distribution is shown. The calculation was done using the SRW code [CE98] in the near field approximation. The number of sampled points inside the undulator influences the precision of the overall calculation and was adjusted accordingly by checking its convergence in the limit of a large number of sampled points.

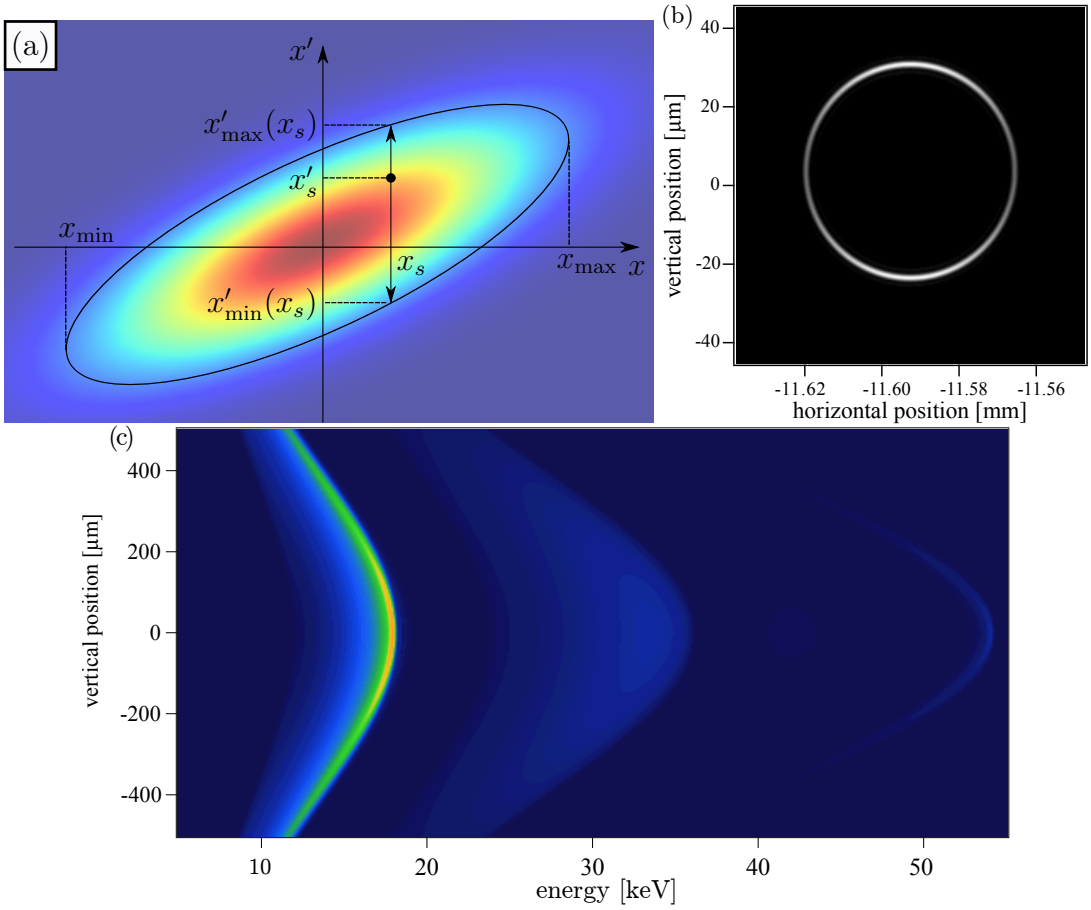

Figure 3.19: (a) shows a sketch of the vertical electron phase space density with one sampled phase space coordinate (x_s, x'_s) together with the FWHM coordinates $x'_{\min}(x_s)$ and $x'_{\max}(x_s)$ between which $x'(x_s)$ is sampled. (b) shows a density plot of the spatial x-ray flux distribution on the detector at an x-ray energy of 18 keV for a filament electron beam corresponding to the phase space coordinate (x_s, x'_s) while (c) shows a density plot of the x-ray flux against the vertical position on the detector and against the x-ray energy for the same filament electron beam.

4 Creation of a high resolution voxel model of the breast

In this chapter the process of creating a high resolution voxel model of the female breast is presented. This model is composed of cube shaped volume elements (voxels) with certain edge lengths and material properties. Together with the calculation of the x-ray beam properties of the laser-driven x-ray source described in the previous chapter this model is needed for the accurate simulation of the image formation and dose deposition in mammography. The use of voxel models created from CT scans of real breast specimen as done in this work provides a more realistic model when compared to analytical models based on certain assumptions [DHB05] that could possibly turn out to be very unrealistic [YBP09].

4.1 Preparation of specimens

In this work two specimens of the female breast that have been gathered from the corpses of two elderly women were used. These specimens have been fixated in a compressed state as done during mammography examinations by using a special procedure described in [HFBD00]. Before preforming a CT scan the specimens were imaged in a conventional mammography unit. Two projections resulting from this examination can be seen in figure 4.2. Unfortunately this revealed that the first of the two specimens has a slightly wrong compression as can be seen by the nipple part being located slightly on top instead of being located at the front side. In order to scan these two specimens at a high resolution it was decided to cut the larger, second specimen down in three pieces by using a special knife provided by the pathology department at the clinical center in Schwabing Munich. This ensured that the pieces fit into the field of view using a high magnification scan geometry. Those three pieces have then been fixated by immersing them into molten paraffin which solidifies after cooling down. Thereby it was prevented that the three individual pieces change their shape during scanning. As the smaller specimen was left in one piece which however was too big for enclosing it in paraffin another method of fixating it was devised using relatively low absorbing PU-foam enclosing the specimen in a PET-bottle which ensured a tight fixation.

(a)

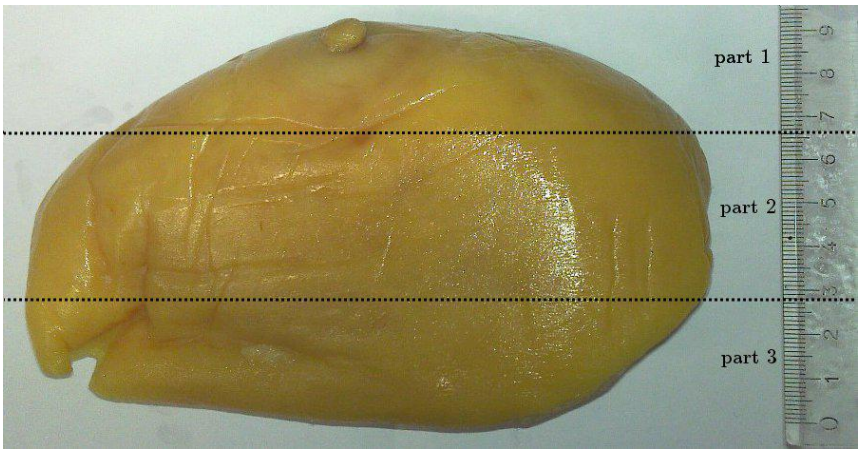

(b)

Figure 4.1: The first (a) and the second (b) breast specimen, fixated with polyethylene glycol in a compressed state. As the second specimen was too large for the field of view of the used magnification CT geometry it was cut in three pieces as indicated by the dashed lines.

4.2 High resolution CT scan

Following the specimen preparation the second step in constructing a realistic voxel model was to perform CT scans of the fixated breast specimens described in the last section. In order to capture the smaller glandular structures inside the breast it is necessary to perform the scan at a high voxel resolution well below 100 µm. As clinically used CT scanners could not provide the desired resolution at high magnification factors and long scan times an industrial microfocus CT installed at the IMETUM facility in Garching [IME12] was used which is shown in figure 4.3. The CT system is a GE vtomex micro focus CT [GE]. The three parts of the first specimen that have been fixated in paraffin blocks were separately mounted onto the rotating holder of the CT system while the second specimen fixated by PU-foam was scanned in one piece. The scan time of

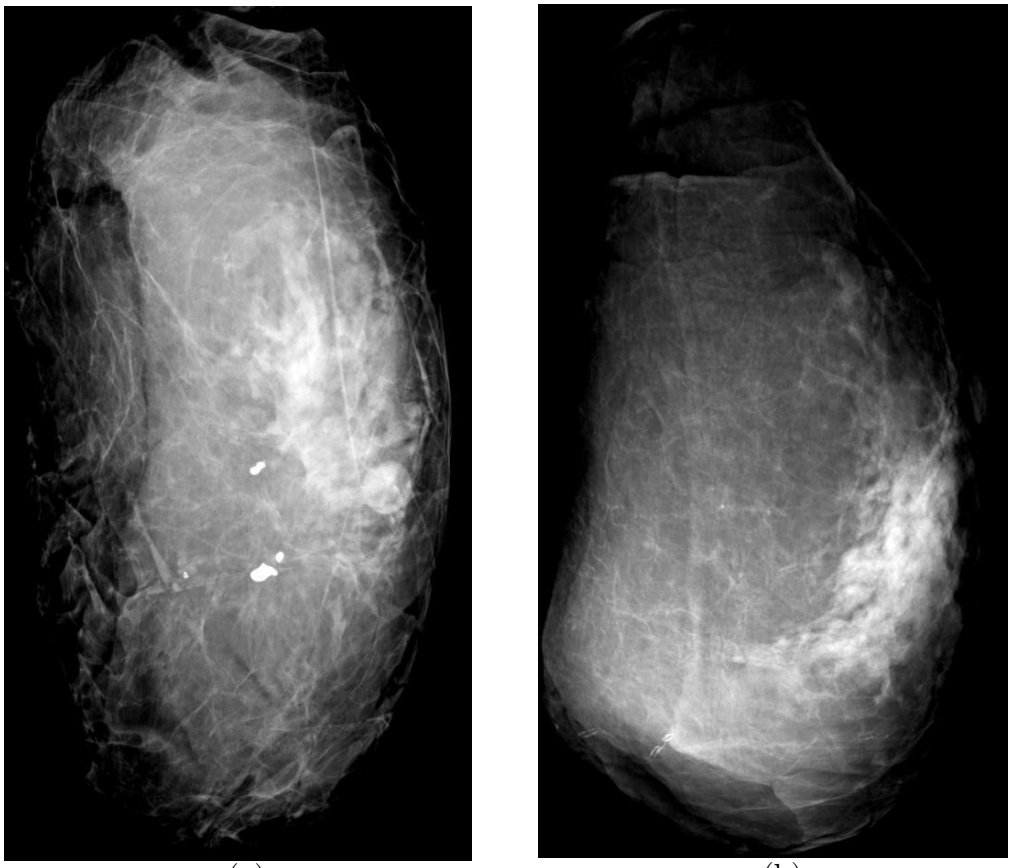

(a) (b)

Figure 4.2: Mammography of the first (a) and the second (b) specimen showed that they are in good shape and that all glandular structures are present. Also some calcifications are clearly visible in the first specimen. This specimen however is compressed in a slightly wrong direction.

the specimen parts were in the range of a few hours and the scans were conducted at magnification factors ranging from 2 to 4 as shown in table 4.1. The system uses an amorphous silicon GE DXR-500 flat panel detector [MB02] with the dimensions of 307 mm $\times$ 240 mm at a resolution of 3072 $\times$ 2400 pixels and a pixel pitch of 100 µm. The reconstruction was done using the GE veloCT software which resulted in 1000 slices per scan at a voxel resolution of 100 µm down to 50 µm as can be seen in table 4.1. However because of the high magnification factor the specimens did not fit completely inside the field of view and multiple scans of the specimens had to be done along the vertical axis. The resulting data from these scans then was combined and post-processed which is described in the next section.

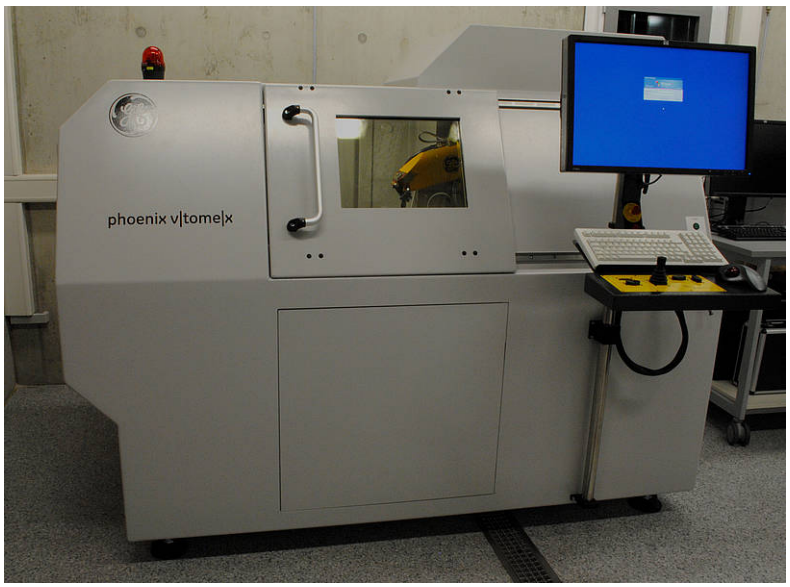

Figure 4.3: GE vtomex micro focus CT system installed at the IMETUM facility in Garching [IME12].

	magnification factor	voxel size
breast 1	3.1	65 µm
breast 2 (part 1)	2.1	95 µm
breast 2 (part 2)	2.3	88 µm
breast 2 (part 3)	2.3	86 µm
breast 2 (part 2) (zoom)	4.0	50 µm

Table 4.1: Magnification factor and voxel size corresponding to the scans of the specimen parts.

4.3 Combination and processing of the scan data

The third step in constructing the final voxel models is composed of the combination and processing of the data obtained during the individual scans. Because of the high magnification factors each part of the first specimen was scanned three times with a movement along the sagittal axis while the second specimen was scanned five times with shifting in this direction. Each scan was chosen in a way that the field-of-view has a considerable overlap with the previous and the following scan in order to make it possible to combine the scans and in order to achieve a higher contrast-to-noise ratio by averaging the overlap regions. The reconstructed slices of the scans were combined by identifying

the overlapping regions and subsequent averaging of the corresponding slices. In this process the different exposure times of the scans leading to different average gray values had to be taken into account together with the slightly different rotation offsets.

Joining together all slices of the non-overlapping regions together with the averaged slices of the overlapping regions resulted in a complete raw dataset corresponding to the first specimen and corresponding to the three parts of the second specimen respectively. It has to be mentioned, that the paraffin enclosing the first specimen and the PU-foam enclosing the second specimen were visible in each of the slices. Unfortunately as the paraffin the PU-foam showed gray values identical to those of some specimen parts a simple segmentation using gray value thresholds was not possible. Also the outer skin layers of the specimen contained regions with highly uneven skin which should not occur in a mammography setup with a compressed breast. Therefore a semi-automatic procedure using the software ImageJ [SRE12] was applied in order to remove the specimen enclosure from the actual specimen in the data and to straighten out uneven skin parts. This procedure is composed of the following steps:

1. Using transversal slices of the scan data a smooth path below the skin is drawn manually in ImageJ.

2. The gray values of the region outside this path is set to zero.

3. The path indicating this skin line is shrunk a few mm which removes artifacts from the fixation process.

4. The region outside the shrunken path is filtered with a Gaussian blur filter. This is needed for the segmentation process described in section 4.4.

5. Steps 1 to 4 are repeated for the next slice.

This procedure is half-automatic as steps 2 to 5 can be implemented as an ImageJ script. However the path corresponding to the skin line still had to be drawn manually for each slice. Step 3 and 4 are necessary for the creation of a smooth skin area during the segmentation as described in the next chapter. Using this procedure it was possible to separate the adipose and the glandular tissue inside the specimen from the enclosure and from the uneven skin parts. Selected transversal and sagittal slices of the specimens are shown in figure 4.4. There and in figure 4.5 it is also visible that cutting the second specimen in three parts unfortunately resulted in the formation of some cavities filled with air.

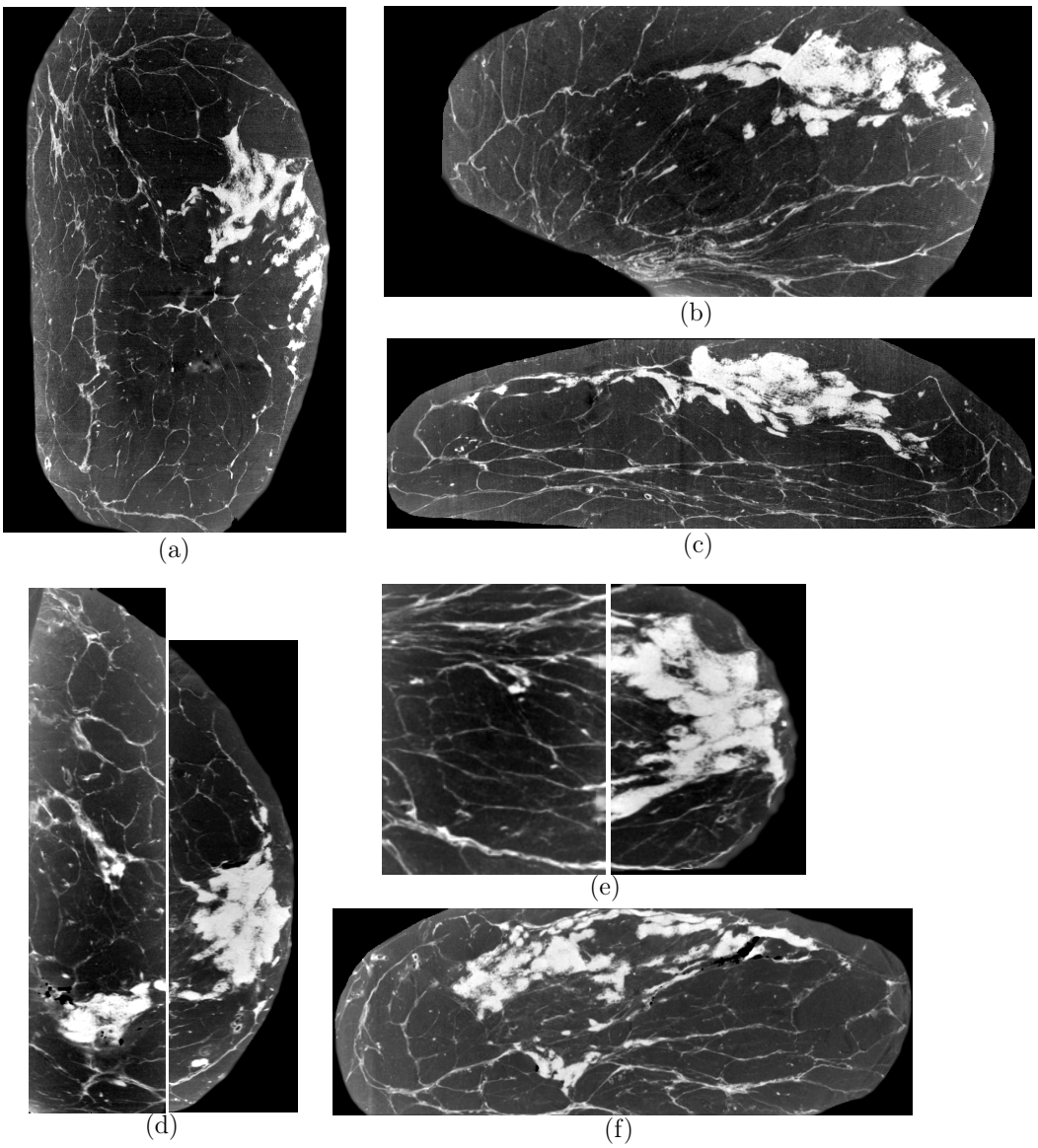

Figure 4.4: Transversal (a), sagittal (b) and coronal (c) slice of the first specimen. Transversal (d), sagittal (e) and coronal (f) slice of the first two parts of the second specimen.

4.4 Segmentation

The final step that remained to be done was the segmentation of the scan data in order to differentiate between the tissue types occurring in the specimens. It was chosen to segment the scan data by using a combination of gray value thresholds and continuous gray value to material assignments into the following regions:

1. Skin: As described in the last section the gray values outside of and including

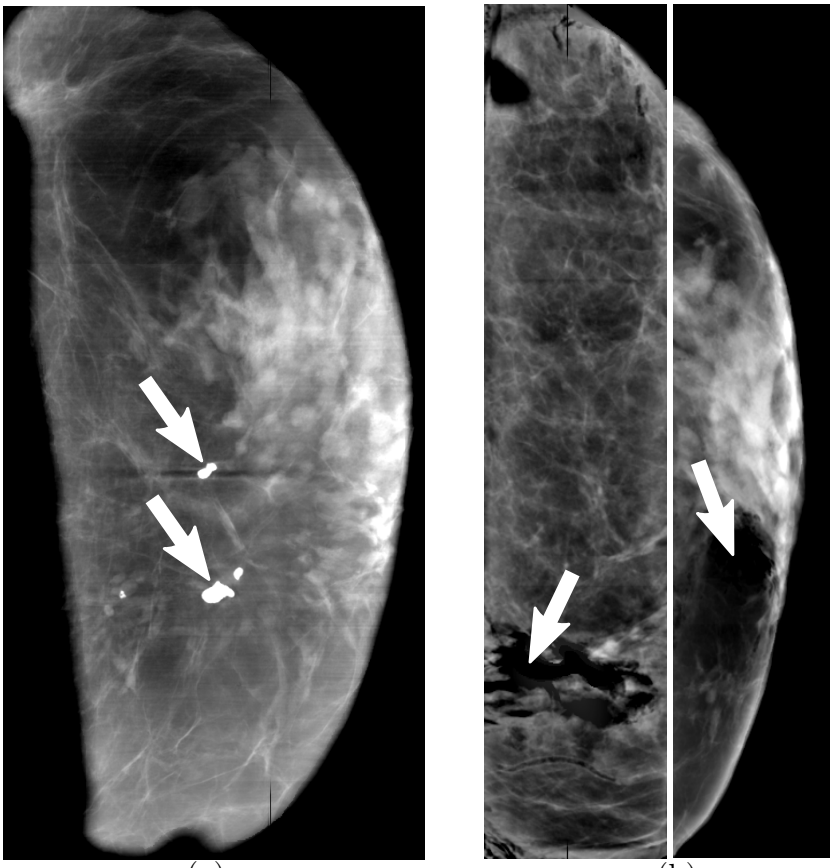

(a) (b)

Figure 4.5: Cranio-caudal projection of the first specimen (a) and of the first two parts of the second specimen (b) created by adding up all transversal slices. In the projection corresponding to the first specimen two calcifications were identified (arrows in (a)) whereas in the projections corresponding to the parts of the second specimen some air filled cavities (arrows in (b)) are visible which resulted from the cutting and transportation process.

the skin layer have been set so zero and the gray values along this line have been smoothened with a Gaussian filter. This makes it possible to select a smooth skin layer by using two lower gray values which is shown in figure 4.6 as a blue area. The method of constructing a smooth skin layer is important here because the uneven skin parts are artifacts from the fixation process which would not occur in the clinical setting with live patients and therefore should not be taken into account in a simulation.

2. Adipose tissue: The gray values between those of the skin layer and a manually selected higher value are identified with the adipose tissue as shown by the green area in figure 4.6.

3. Adipose-Glandular mixed tissue: By using a coarse segmentation between glandular and adipose tissue the smaller structures would have been lost, therefore it is necessary to identify a region containing an adipose-glandular mixture. The ratio between the fraction of adipose tissue and the fraction of glandular tissue of one voxel is determined by its gray value and is linearly scaled between an adipose-to-glandular ratio of 0 up to an adipose-to-glandular ratio of 1.

4. Glandular tissue: The volumes identified as consisting entirely of glandular tissue are also selected by using a higher gray value threshold which is indicated by the red area in figure 4.6.

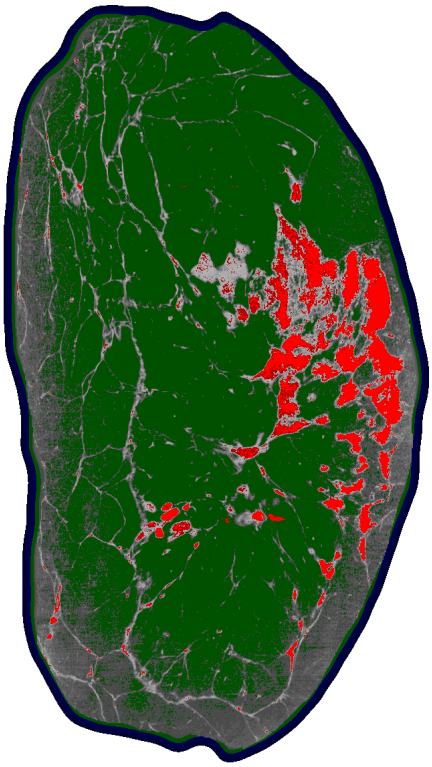

Figure 4.6: Segmented transversal section of the scan data of the first specimen. The regions containing skin tissue (dark blue), adipose tissue (green), glandular tissue (red) and a mixture of adipose and glandular tissue (gray values) are selected by using gray value thresholds. The segmentation has been done using the ImageJ software [SRE12].

The gray value thresholds corresponding to these regions were determined manually for each voxel model and were saved in a configuration file. As described in section 4.3 in order to segment the skin tissue the voxel data consisting of the gray values had to be manually preprocessed as the gray values of the skin tissue overlap the gray values

of the glandular tissue because of their similar attenuation coefficients. To resolve this problem the voxel data was preprocessed using the imaging program ImageJ [SRE12] whereby the regions corresponding to skin tissue were manually segmented and set to a specific gray value outside the gray value range of the glandular tissue. In this process also the segmented region corresponding to skin tissue was cleaned from scan artifacts and uneven parts in order to ensure a flat surface as present in real mammography examinations where the breast gets evenly compressed between two plates.

The gray values of all slices are then saved together in a raw data file together with a configuration file containing the gray value thresholds corresponding to the different tissue regions.

5 Monte Carlo simulation of x-ray absorption imaging using the Geant4 software toolkit

Monte Carlo simulations can be defined as computational models of specific physical or mathematical systems in which a large number of randomly drawn values are used for sampling a certain part of the system in order to determine the properties of the system. They have a wide range of applications and are particularly suitable to model complex systems that are hard to be described by analytical means or deterministic computations. The usefulness of these simulations is based on the fact that under certain conditions the combination of a repeated calculation using the randomly sampled input variables converges to a result accurately describing the system in the limit of an infinite number of repetitions due to the law of large numbers [KW08]. In this work Monte Carlo simulations have been used in order to calculate certain properties of the image formation and dose deposition process in x-ray absorption imaging. They are particularly applicable here because the imaging process consists of the interaction of a large number of photons with matter, where both the geometry as well as the different physics processes are complex and prohibit practical and accurate analytical computations.

Since Monte Carlo simulations have a long history of application in simulating x-ray imaging a number of codes have been written. Among the generally applicable simulation codes there are the well known MCNP [Bri93], EGS [KR03], FLUKA [FFR03] and Geant4 [A03] codes. While the EGS code system is capable of simulating the interaction of electrons and x-rays with matter the other three code systems encompass the simulation of a wide range of particle types together with their associated physics effects. In this work the code system Geant4 has been chosen and its structure is described in the following sub-section.

The Geant4 Software Toolkit is an open source, general purpose software package for the simulation of the passage of particles through matter. The name Geant is an acronym for "GEometry ANd Tracking". It uses Monte Carlo methods in order to track individual particles and to simulate the physics effects involved in the interaction of these particles with matter. The development of Geant started off at the European organization for nuclear research (CERN) in order to study the design and properties of detectors. The first version of Geant has been written in 1974 and continuously new

versions have been released. The code initially has been written in the FORTRAN [Bac98] programming language but a redesign of the code in C++ [Str00] has been done in the fourth version starting in 1993 leading to Geant4 [A03]. It is now developed and actively maintained by the international Geant4 collaboration established in 1999.

5.1 Structure and properties of the Geant4 Software Toolkit

The Geant4 software toolkit encompasses all necessary simulation steps for the simulation of the passage of particles through matter, consisting of:

- Definition of the geometry: A wide range of geometries from simple solids like cubes, cylinders and spheres up to complex parameterized solids as well as voxel models can be defined.
- Selection of particles: Owing to the development of Geant4 in the field of high energy physics a large number particle types can be defined.
- Selection of the physics processes: Geant4 implements over 100 different physics processes for photons, electrons, muons and hadrons. As this work deals with the simulation of x-ray imaging the relevant physics processes are Compton scattering, Rayleigh scattering and the Photoelectric effect which were described previously in section 2.2. For each particle type Geant4 also allows the selection of specific physics models. In this work the low-energy models for photons and electrons namely the Livermore model based on the data tabulated in [Per91, CHK97] and the PENELOPE model described in [SA01] were used.
- Generation of the primary events: The initial conditions of the particles and the geometry can be extensively defined.
- Tracking of the particles through matter: Geant4 tracks the passage of individual particles through the defined geometry with their associated materials taking into account all selected physics processes. In the context of x-ray imaging these consist of the photoelectric effect, Compton scattering and Rayleigh scattering. Each particle track consists of steps that are computed by Geant4 using the specified geometry and parameters governing the step length. Geant4 uses a number of algorithms adapted to the different geometries for efficiently determining these steps. In this work especially the algorithms for tracking the passage of particles through voxel models were used.
- Generation of events: Associated to each generated primary particle and its track are the secondary particles that are generated by its interaction with matter.

- Detection geometry: The tracked particles can be detected by various types of detectors, ranging from simple calorimeters to detectors capable of registering energy and position information of the particles.
- Visualization: Geant4 allows for the visualization of the geometry and the particles track structures using various methods.
- Storage and analysis of the event data: Geant4 provides data structures for the efficient handling and analysis of the data generated during the events.
- User interface: Geant4 provides a command line user interface capable of controlling many parts of the simulation.
- User handling routines: There are many pre-defined routines by which users can access almost every part of the simulation.

The Geant4 toolkit has been specifically chosen in this work for a number of reasons and because it has a number of advantages over other simulations codes:

- Object oriented design: Geant4 is written in the C++ [Str00] programming language which, in the opinion of the author, makes it extremely flexible and easy to maintain large projects when compared to other simulations written in the FORTRAN [Bac98] programming language. Also this allows the easy replacement of parts of the simulation as for example the list of selected physics processes.
- Extensive set of user handling routines: Almost every part of the simulation is equipped with certain user handling routines that allow to influence each simulation step. Thereby it is easy to write own code replacing parts of the simulation as it was done for the ray-tracing code described in sub-section 5.2.7.
- Physics models: The large number of physics models Geant4 provides allows the selection of a suitable model for a specific task and to compare the results of simulations using different physics models. The physics models are either analytical or based on tabulated data or a combination of both and are suitable to different energy ranges and have different computational speeds.
- Geometry definition: One of the strengths of Geant4 is the wide range of geometries that can be defined. This work made heavy use of the implementation of voxelized volumes in Geant4.
- Material definition: It is possible to define material mixtures and composite materials with a wide range of parameters.

- Geant4 is actively developed by a large community of physicists and is constantly improved. Also this made it easy to contact developers and users.

5.1.1 Simulation steps of a Geant4 run

As described in [Col09] before a simulation run with the Geant4 toolkit can be started the initial configuration of the simulation has to be specified. At first the geometry and the materials of the detector and of all other objects needs to be configured. Then the physics models for the different particles are selected and configured. After that the actual simulation of the passage of the particles through the initially defined materials and geometries is done during individual simulation runs. Each run produces a specified number of so called events. These events consist of the particle tracks which itself consist of individual steps. The process of a simulation run including the generation of events is summarized in the following list:

1. A simulation run starts with the initialization of the random number generator: Geant4 uses routines from the CLHEP library [STH10] implementing various pseudo random number generators. In this work the seeds for the random number generator are based on the current system time of the used operating system.

2. Generation of primary particles: The positions and velocities of the primary particles are then set to their initial values.

3. The interaction probability distribution along the path of the primary particle is calculated for each physics process based on the applied physics model. Using the output of the random number generator a certain free path is then chosen taking into account the probability distribution for each physics process. The physics process that gives the smallest distance is then selected. In contrast to most comparable simulation codes Geant4 implements a range cut off instead of an energy cut off for the production of secondary particles and computes tables of the energy to range dependence for each particle, material and physics process for each run. This has the advantage that the cut values for different settings are handled in a coherent manner and ensures a precision down to a certain spatial range instead of a certain energy which could lead to very different range cut offs depending on the particle type and material.

4. If the selected physics process invokes an interaction or decay defined by a discrete process, secondary particles are created with energies depending on the specific type of physics process. After that the energy of the primary particle is adjusted.

5. The energy of the primary particle is updated taking into account all continuous processes.

6. The tracking described in steps 3 to 5 is then repeated for all secondary particles and the primary particle until the step length reaches the predefined minimum range.

7. The steps 2 to 6 constitute one event. These steps are repeated until the maximum number of events is reached which completes the simulation run.

For each of these simulation steps there are user handling routines whereby own code can be inserted in order to influence the tracking or to get information about the particles. This conveniently allows for an extensive modification of the simulation procedures or for the addition of new user defined physics processes.

5.1.2 Parallelization

The accurate simulation of a large number of events can be computationally intensive and time consuming with limited resources. This work deals with the simulation of x-ray imaging where one realistic x-ray exposure consists of about 10^{11} photons. However the calculation of each simulation run is independent from other runs which offers the opportunity to compute multiple runs in parallel.

Unfortunately Geant4 itself implements no thread handling that could perform either runs or events in parallel. Therefore one has to write additional routines for the parallelization of the simulation. In this work the message passing interface standard (MPI) [Mes94] was chosen and based on the Geant4 code a parallelized run manager using the MPICH2 [LDS96] implementation was written. The MPI run manager allows to distribute several runs on a cluster of computers. In this work the Linux cluster of the Leibniz-Rechenzentrum in Munich was specifically used for running the parallelized simulation of x-ray imaging.

5.2 Simulation methods in mammography

In this work a Monte Carlo simulation utilizing the Geant4 software toolkit was developed which builds upon the beam calculations and on the created mammographic voxel models which are described in section 3 and 4 respectively. This simulation takes into account all relevant absorption and scattering processes and tries to model the different x-ray sources as accurately as it is possible with limited computational resources. In order to get quantitative results about the imaging performance of the laser-driven x-ray source considered in this work the simulation has to take into account in detail the parameters of the imaging setup as well as the various source parameters.

In the following at first the implementation of the voxel models based on the previously created CT-scan data is explained in sub-section 5.2.1 and the simulation methods that were developed in this work are described in sub-sections 5.2.2 to 5.2.7. After

describing the basic simulation methods the structure and process of the simulation is outlined in sub-section 5.2.8. This is then followed by a description of the image quality determination in sub-section 5.2.9.

5.2.1 Implementation of voxel models of the female breast

The simulation starts by loading all configuration options, stored in a single configuration file which is written in XML [BPSM08]. There it is specified which voxel model data is to be loaded and the values of the parameters governing the implementation of the voxel models in the simulation are specified.

Loading of the gray value data: In chapter 4 the creation of the voxel model data from two breast specimens has been described. This data consists of a 3-dimensional array of gray values where each value corresponds to a voxel which has a certain edge length that is specified in the configuration file. This gray value data is processed at the start of each simulation. The parameters of the different voxel models together with the corresponding breast thickness are shown in table 5.1.

dimension	columns	rows	slices	voxel size	thickness
breast 1	2464	636	1404	65 µm	41.3 mm
breast 2 (part 1)	1586	516	292	95 µm	49.2 mm
breast 2 (part 2)	1776	525	318	88 µm	46.3 mm
breast 2 (part 3)	826	529	132	86 µm	45.6 mm

Table 5.1: voxel model parameters

Assignment of the elemental composition to the voxels: In order to construct a voxelized model from the segmented data suitable for the simulation of x-ray absorption imaging using the Geant4 software toolkit the gray values corresponding to the different tissues have to be translated into elemental compositions. According to the segmentation described in section 4.4 each voxel is defined to have a certain tissue composition. As shown in figure 4.6 the gray value data corresponding to the voxel models has been segmented into the following four regions:

1. skin tissue
2. adipose tissue

3. mixture of adipose and glandular tissue
4. glandular tissue

Using this preprocessed gray value data and the threshold parameters resulting from the previously described segmentation procedure the first step in the simulation is to assign to each voxel an elemental composition. In this work the elemental compositions and densities of the different tissue types were set to the values found in [ICR88] which are shown in table 5.2. For the segmented regions of adipose tissue and glandular tissue a

tissue type	H	C	N	O	Na	P	S	Cl	K	density [g/l]
adipose	11.4	59.8	0.7	27.8	0.1	0.0	0.1	0.1	0.0	950
glandular	10.6	33.2	3.0	52.7	0.1	0.1	0.2	0.1	0.0	1020
skin	10	20.4	4.2	64.5	0.2	0.1	0.2	0.3	0.1	1090

Table 5.2: Elemental mass fractions in percent and densities of skin, adipose and glandular tissue [ICR88].

homogeneous material composition is assumed. For the region that has been identified as a mixture of adipose and glandular tissue however a more accurate assignment of material properties to the individual voxels has to be done. There the simulation defines for each voxel a mixture of adipose and glandular material whose mass fractions are linearly scaled according to the corresponding gray value of the voxel. This scaling is done between the threshold corresponding to the adipose tissue and the threshold corresponding to the glandular tissue. This method of scaling between the region corresponding to adipose tissue and glandular tissue is important in order to capture the smaller structures of the fibro-glandular tissue which would otherwise be discarded by a coarse segmentation. The previously described segmentation of the CT-scan data using a combination of thresholds and gray-value scaling provides for each breast a realistic voxel model. These voxel models are suitable for the accurate determination of the image contrast and the radiation dose deposited in the radiation sensitive glandular tissue for different exposures. However in order to precisely quantify the properties of the noise in the images due to the statistics of the primary and scattered photons the simulation employs a simpler homogeneous model described in the next sub-section.

5.2.2 Implementation of a homogeneous model of the female breast

As described in section 2.3 the image formation in x-ray absorption imaging is a statistical process in which a certain number of photons which are transmitted through the

imaged object hit a detector. In that section it is also shown that the image formation at the detector can be described by a point process whose probability distribution has a variance which is proportional to the number of incident photons. The fluctuations that are due to this statistical image formation process are called "quantum noise". The characteristics of the quantum noise present in mammography images depend on the material composition of the breast, the detection geometry and the x-ray beam quality. In order to determine the quantum noise for different beam qualities and detection geometries it is necessary to separate this noise from the intensity fluctuations that are due to the tissue structures inside the realistic voxel model. Therefore a simpler homogeneous phantom modeling the breast was created. It consists of a half-cylinder with a mixture of adipose tissue material and glandular tissue material assigned to it and an outer layer that is set to the material corresponding to skin tissue which is shown in figure 5.1. The mass fractions of the adipose and glandular material are set to the mean values found in the more detailed voxel model. This homogeneous model of the

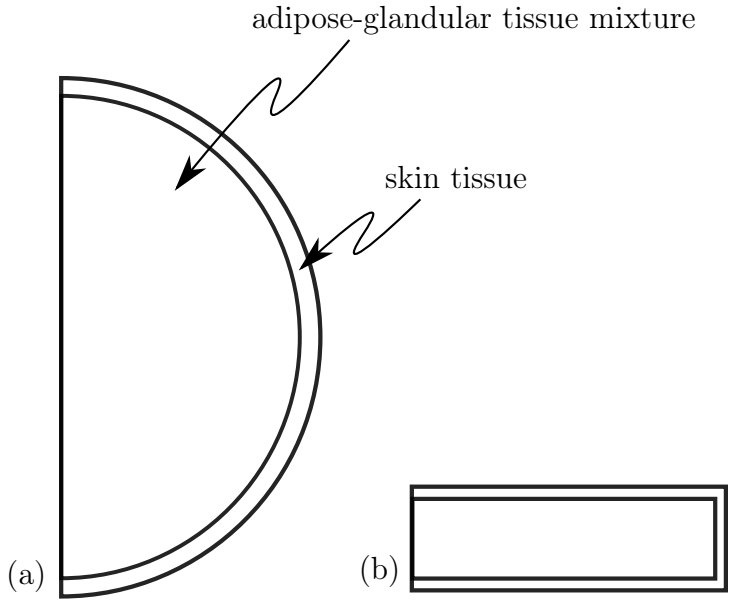

Figure 5.1: Transversal (a) and sagittal (b) section of the homogeneous breast phantom

compressed breast makes it possible to calculate the quantum noise for different x-ray beam qualities and detection geometries. After the creation of the specific model of the breast the simulation proceeds by loading the parameters and data of the different x-ray beams which is explained in detail in the next sub-section.

5.2.3 Implementation of x-ray beams

Undulator x-ray beam implementation: In section 3.3 two methods of calculating certain properties of the x-ray beam created by a laser-driven undulator x-ray source

were described. The first method results in a calculation of the total x-ray spectrum of the x-rays that pass a slit at a specific distance from the source while the second method is a more comprehensive calculation of the x-ray beam properties. There the electron phase space of the electrons inside the undulator is sampled at equidistant points and for each of these points the spectral and spatial x-ray distribution resulting from the electron motion at this point is calculated in the detector plane. This results in a more detailed characterization of the divergence properties and the angular spectral flux as well as of the source size of the x-ray beam. In order to implement the results of these beam calculations in our simulation a method was devised which is composed of three steps:

1. Loading of the sampled beam data: Before running the simulation the number of photons per sampled point, resulting from the calculation described in subsection 3.4, were normalized to a total electron charge of 1 C and have been saved as floating point values. The beam data therefore is given by a six-dimensional array N_{E,l,x_h,x_v,y_h,y_v} of floating point values consisting of $n_E \times n_l \times n_{x_h} \times n_{x_v} \times n_{y_h} \times n_{y_v}$ energy and position bins. The elements of this array give the number of photons emitted from the transversal position bins x_h, x_v and the longitudinal position bins l inside the undulator with an energy from the energy bin E which hit the detector at the detector position bins y_h, y_v. This array is loaded into memory at the beginning of the simulation.

2. As, according to equation 3.2, the phase space density of the electron beam inside the undulator has been assumed to be of Gaussian shape the spatial distribution of the number of photons created inside the undulator is also of Gaussian shape. Therefore for each of the $n_E \times n_l$ energy and longitudinal position bins indexed by E and l respectively the Gaussian

$$n_{E,l}\left(x_h, x_v\right) = A_{E,l} \exp\left(-\frac{x_h^2}{2\sigma_{h,E,l}^2} - \frac{x_v^2}{2\sigma_{v,E,l}^2}\right) \tag{5.1}$$

   is fitted to the discrete values $N_{E,l,x_h,x_v} = \sum_{y_h,y_v} N_{E,l,x_h,x_v,y_h,y_v}$ which correspond to the total number of photons originating from the source position bins x_h, x_v inside the undulator and which belong to the energy bin E and the longitudinal position bin l. The fit is done using an instance of the Levenberg–Marquardt algorithm which gives a numerical solution to the corresponding least-squares problem [Mor78]. This ensures a continuous distribution of x-rays on the detector free from sampling artifacts. The values of $\sigma_{h,E,l}$, $\sigma_{v,E,l}$ and $A_{E,l}$ are then stored in separate arrays.

3. In the second step of a simulation run using Geant4, which is described in subsection 5.1.1, the initial positions and momenta of the x-rays have to be specified. This is done by utilizing the previously initialized pseudo random number generator of Geant4 in a method consisting of the following steps:

   a) The longitudinal position l and the x-ray energy E are set to randomly chosen values with a probability

   $$P(E,l) = \frac{1}{N} \sum_{x_h,x_v} \sum_{y_h,y_v} N_{E,l,x_h,x_v,y_h,y_v}$$

   of selecting the energy bin E and the longitudinal position bin l where N is the total number of photons in the x-ray beam and a uniform probability distribution within each energy and position bin is assumed.

   b) Using the previously determined values of $\sigma_{h,E,l}$, $\sigma_{v,E,l}$ and $A_{E,l}$ the transversal x-ray source coordinates (x_h, x_v) are randomly chosen using the Gaussian probability density

   $$P(E,l,x_h,x_v) = \frac{1}{N} n_{E,l}(x_h,x_v)$$

   with $n_{E,l}$ defined in equation 5.1.

   c) The direction of the x-ray momentum is set in a way that it points from (x_h, x_v, l) to (y_h, y_v, d). While d corresponds to the detector position, the transversal coordinates (y_h, y_v) are randomly selected with a probability

   $$P(E,l,x_h,x_v,y_h,y_v) = \frac{1}{N} N_{E,l,x_h,x_v,y_h,y_v}$$

   for selecting the detector position bin corresponding to (y_h, y_v) and using a uniform probability distribution within each bin.

One important step in this undulator beam implementation is the fitting routine which leads to a continuous Gaussian x-ray distribution on the detector for each energy and source position inside the undulator. This beam implementation of the undulator x-ray source is used in this work to create a Monte Carlo simulation of x-ray absorption imaging while taking into account all relevant characteristics of this source as the finite source size due to the finite emittance and the angular spectral flux and divergence properties.

X-ray tube implementation: Since one of the goals of this work is to compare the performance of a novel x-ray source to conventional x-ray tubes also the spectra and

beam geometries of x-ray tubes have to be included in our simulation of the image formation and dose deposition in mammography. Here pre-calculated spectra that are applied clinically in mammography and which have been published in tabulated form in [CGFD97] were used. In accordance with [BMH06] it was found that the spectra resulting from either molybdenum anodes together with molybdenum filters or tungsten anodes with rhodium filters to deliver the best image quality per applied dose. One example of a typically used mammographic spectrum is shown in figure 5.2. The spectra were implemented in the simulation by calculating a probability density in the form of a step function corresponding to the number of photons at the energy bins found in the tabulated spectral data. In the simulation the x-ray energy was then randomly set according to the values of this probability density and their associated energies. Besides the x-ray spectrum also the beam geometry was implemented by including a parameter in the simulation for the size and shape of the focal spot. The focal spot shape is selectable to be either a uniform or Gaussian distribution. The distance of the focal spot is set to be 0.65 m from the detector while the field of view is set to enclose the whole detector.

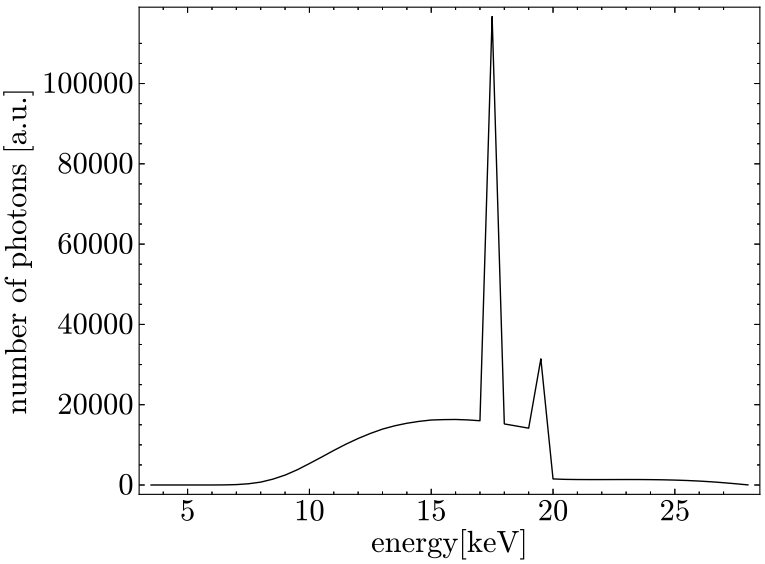

Figure 5.2: Spectrum of an x-ray tube with a molybdenum anode at 28 kVp and a molybdenum filter of 30 µm thickness.

Parallel beam implementation: In order to separate the effects of the spectrum on the image quality from the effects of the beam geometry also a parallel beam geometry was implemented. There all x-rays are emitted perpendicular to the detector plane at uniformly distributed random transversal coordinates.

5.2.4 Scanning geometry with a laminar undulator x-ray beam

Owing to the undulator x-ray beam described in section 3.2 having a laminar profile as shown in figure 3.10 the imaging procedure has to be done using a scanning geometry. There the horizontally spread out laminar beam scans vertically over the object. If the laser driving the undulator x-ray source is operated in a pulsed mode then after each pulse the source has to be moved one step in the vertical direction. The advantage of this scanning imaging procedure is that x-rays that are scattered inside the object, which usually degrade the image quality, can be discarded to a great extent which is quantified in sub-section 6.2.4.

5.2.5 Monte Carlo simulation of the x-ray-matter interaction

After the voxel models of the breast specimens and various models of x-ray sources were implemented in the simulation the interaction and transmission of x-rays with the material associated to the voxel models were modeled. In order to capture all relevant scattering and absorption processes and the effect of the finite number of photons on the image noise the Geant4 software toolkit [A03] was used which is based on the Monte Carlo methods described in sub-section 5.1. The methods of constructing the voxel model and implementing the x-ray sources described in the previous sub-section were then combined with the routines and data structures of the Geant4 toolkit and were inserted in appropriate user routines offered by Geant4.

Owing to the fact that our voxel models of the breast contain - excluding tissue mixtures - only three different materials, this work made use of certain routines of Geant4 that merge volumes with the same material so that the boundaries between voxels with the same material can be skipped during the x-ray tracking. Using the Monte Carlo methods described in subsection 5.1, the simulation takes into account the absorption of x-rays through the photoelectric effect and the scattering of x-rays due to Rayleigh- and Compton scattering. In this work the standard Geant4 x-ray tracking routines were supplemented with own routines separating between transmitted x-rays, Rayleigh scattered x-rays and Compton scattered x-rays, which is shown in figure 5.4. Furthermore own routines that make use of Geant4s detector classes were written and applied in this work that record the dose deposition during the x-ray exposure. There the radiation dose is recorded separately for the different tissue types also taking into account tissue mixtures by weighting the dose according to the corresponding mass fractions. This is especially important in the simulation of mammography as the dose of the radiation-sensitive glandular tissue is the relevant factor which strongly depends on the distribution and ratio of the tissues [YBP09] together with the applied x-ray spectrum [Boo02].

5.2.6 Detector implementation

In order to simulate energy resolved imaging techniques routines for the energy resolved detection of x-rays were written and implemented in the simulation. The detector itself is implemented in the simulation with a configurable pixel size and energy bin size. Furthermore the detector is assumed to have an ideal detection efficiency and to integrate the total energy within each particular energy bin. Also a configurable gap size between the detector and the object being imaged is implemented in order to simulate magnification imaging. The detector size is set to be identical with the object dimensions while the pixel size is set to the voxel size corresponding to the voxel model used in the simulation.

5.2.7 Ray-tracing

In principle the previously described Monte Carlo methods would be sufficient for simulating all relevant properties of the image formation with a high precision. However they are also computationally expensive and therefore creating images free from quantum noise is not feasible using these methods. For the accurate calculation of image quality properties like contrast and spatial frequencies, images without quantum noise are needed. Therefore a ray-tracing method was written supplementing the tracking procedures offered by Geant4. This method takes into account the same physics processes as the default Geant4 tracking prodecures but it is based on a deterministic and continuous implementation of the physics effects using a ray-tracing technique. While neglecting all scattering processes this method accounts for the image formation due to the different absorption of the x-rays in the glandular tissue structures inside the breast. The physics processes in this ray-tracing method are implemented by using pre-calculated cross sections for all relevant physics processes and element-energy combinations. For each ray hitting the detector the ray is divided into steps defined by the coordinates at which the ray enters and exits a volume or voxel and the step lengths as well as the material composition corresponding to the volume are determined. Then, following section 2.3, for each step the energy dependent attenuation coefficient $\mu_n(E)$ corresponding to the n-th step is calculated according to equation 2.34 which gives

$$\mu_n(E) = N_A \rho_n \sum_i \sum_j \frac{c_{i,n}}{M_i} \sigma_{i,j}(Z_i, E)$$

where N_A is the Avogadro constant, ρ_n is the density of the material encountered in the n-th step, i is the index corresponding to the i-th element in the material,j is the index corresponding to the j-th physics process, while $c_{i,n}$, M_i, $\sigma_{i,j}$ and Z_i are the mass fraction, the molar mass, the cross section per atom and the atomic number of the i-th element respectively and E is the x-ray energy. The attenuation corresponding to the

x-ray energy E for all steps is then given by

$$I(E) = I_0(E) \exp\left(-\sum_n \mu_n(E)\, d_n\right) \tag{5.2}$$

where d_n is the length of the n-th step and I_0 is the spectral flux density function corresponding to the x-ray source output. For an ideal energy integrating detector then the total detected flux is given by

$$I = \int_0^{E_{\max}} I(E)\, \mathrm{d}E \tag{5.3}$$

For a spectrum consisting of discrete energy bins the rays were weighted by $I_0(E_k)$ for the k-th energy bin. Then in order to get a complete image for each energy bin a family of rays is created consisting of rays pointing from the focal spot to each of the detector pixels. The ray-tracing method described in this subsection has been implemented as a custom physics effect replacing the default effects based on Monte Carlo methods. This has the advantage that all other parts of the simulation are left unchanged and the same simulation parameters can be used either with the ray-tracing method or with Monte Carlo methods. Moreover in this work new methods were developed for simulating finite focal spot sizes by combining the ray-tracing technique described in this subsection with the Monte Carlo based event generation. There the origin of the rays is selected randomly according to a Gaussian probability distribution with a standard deviation corresponding to the focal spot size and a simulation run then consists of a large number of ray tracing runs. The application of this method in the analysis of the dependence of the spatial resolution on the focal spot size is discussed in section 6.5.

5.2.8 Simulation sequence of mammography

In the last section all of the developed methods for the simulation of mammography have been presented. In this chapter it is described how these methods were combined in order to get a comprehensive picture of the image formation and dose deposition and of the resulting image quality. After selecting a model of the x-ray source that should be used in the simulation and selecting a voxel model of the breast together with the remaining detector parameters a sequence of simulation runs is started consisting of the following steps:

1. **Ray-tracing with voxel model:** As described in subsection 5.2.7 a full ray-tracing run of the simulation results in a mammogram that is free from quantum noise and contains no contribution from scattered x-rays. The resulting images are ideally suited for determining the contrast of specific structures inside the breast

and for investigating the effect of different x-ray spectra and beam parameters on the image contrast. The ray-tracing method is used here because the smaller structures and soft tissues found in breasts would get lost in the quantum noise present in Monte Carlo simulations. Figure 5.3 shows two mammograms created with the ray-tracing method using an x-ray tube spectrum.

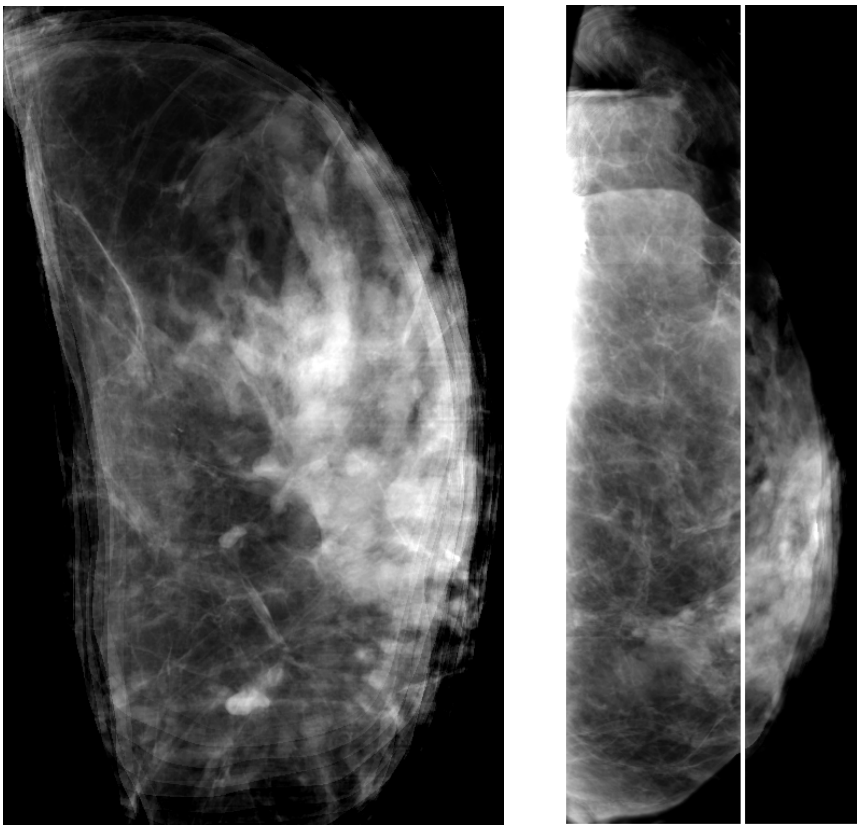

(a) (b) (c)

Figure 5.3: Mammograms generated using the ray-tracing method described in subsection 5.2.7 and using the voxel models corresponding to the two scanned breast specimens. (a) shows a mammogram of the first breast while (b) and (c) show two parts of the mammogram of the second breast. The images were generated with a monochromatic spectrum at 18 keV and a parallel beam geometry.

2. **Monte Carlo simulation with voxel model:** The Monte Carlo methods described in subsection 5.2.5 constitute a more complete model of the image formation and also give information about the dose deposition process. Using these methods allowed us to get information about the scattered x-rays and to determine the average glandular radiation dose (AGD) deposited in the glandular tissue. There the dose deposition is recorded for each absorbed or scattered x-ray and is

weighted by the ratio of the amount of glandular to the amount of adipose tissue present in the corresponding voxel volume. This calculation makes use of the attribution of material mixtures corresponding to mixtures of glandular and adipose tissue to the voxels as described in subsection 5.2.1. Figure 5.4 shows sample images of the transmitted primary x-rays as well as of the scattered x-rays resulting from this simulation run.

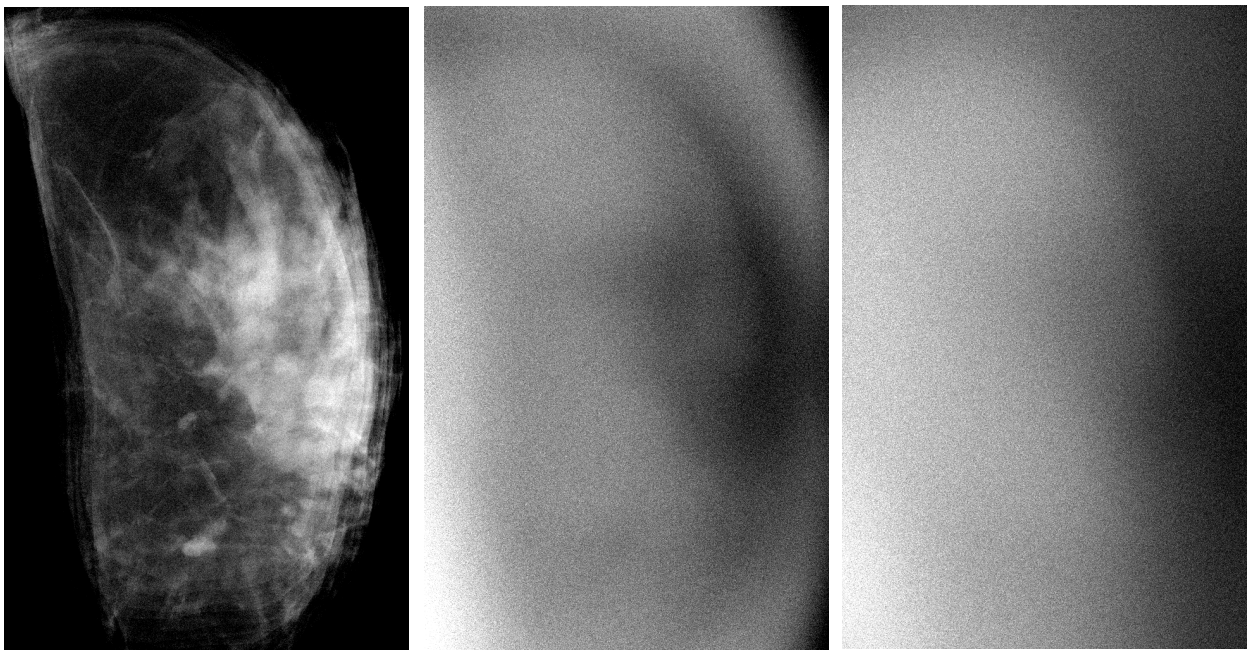

(a) (b) (c)

Figure 5.4: Mammogram generated with the Monte Carlo method described in subsection 5.2.5 applied to the first voxel model corresponding to one of the two scanned breast specimens. (a) shows a mammogram of the first breast containing the detector signal from transmitted an scattered x-rays while (b) and (c) show only the detector signal from the Rayleigh scattered and Compton scattered x-rays respectively. The images were generated with a monochromatic spectrum at 18 keV and a parallel beam geometry at a glandular dose of 0.186 mGy.

3. **Monte Carlo simulation with homogeneous phantom:** In order to estimate the quantum noise present in the images and its dependence on the beam properties the homogeneous phantom described in subsection 5.2.2 was selected for the simulation together with the previously mentioned Monte Carlo methods. Thereby it is possible to quantify the influence of the beam properties and the scattered radiation on the quantum noise, which would be obscured by the structures in the image of the voxel model simulation.

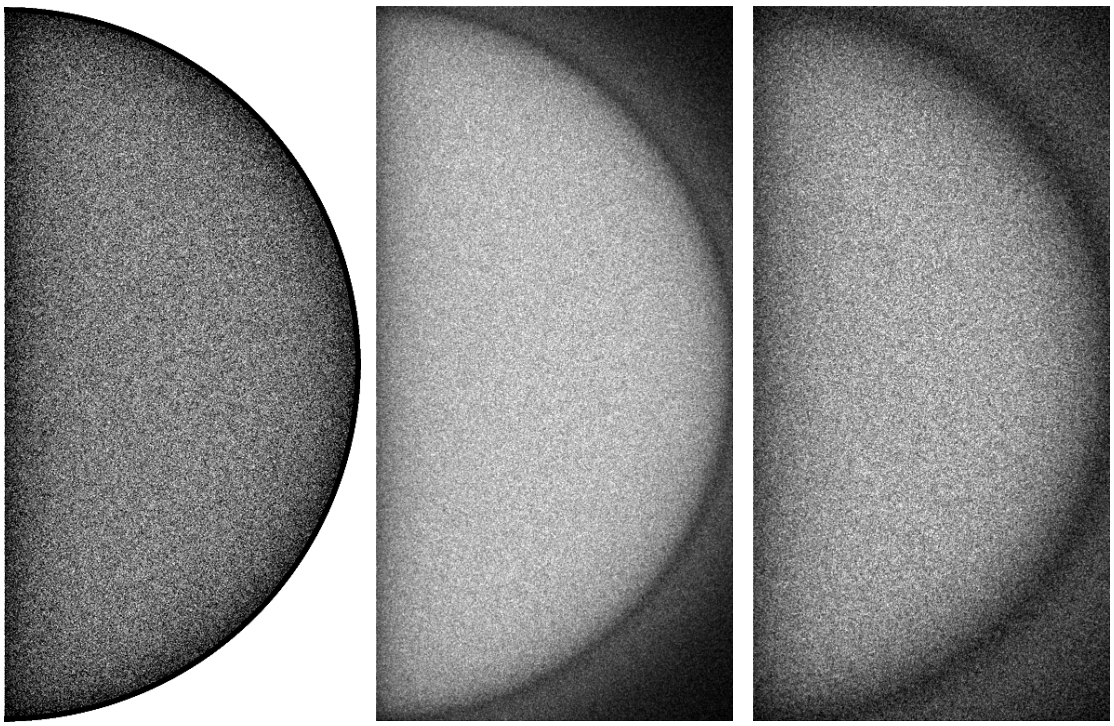

(a) (b) (c)

Figure 5.5: Images generated using the Monte Carlo method described in subsection 5.2.5 and using a homogeneous breast phantom. (a) shows the total detector image from transmitted and scattered x-rays while (b) and (c) show the detector images from the Rayleigh scattered and Compton scattered x-rays respectively. The images were generated with a monochromatic spectrum at 18 keV and a parallel beam geometry.

5.2.9 Quantification of the image-quality-to-dose relationship

Using the results from the simulation sequence described in the previous section allowed for an estimation of the image-quality-to-dose relationship in mammography for the considered x-ray sources and detection geometries. Here and in the next chapter the ratio of the squared signal-difference-to-noise ratio to the average glandular dose ($\mathrm{SDNR}^2/\mathrm{AGD}$), introduced in section 2.3, is used as a figure of merit. Following section 2.3 it is assumed that the signal-difference-to-noise ratio is defined by equation 2.38 which in this context gives

$$\mathrm{SDNR}^2/\mathrm{AGD} = \frac{\left(\Delta S_{\mathrm{mean}}/\sigma\right)^2}{\mathrm{AGD}} \tag{5.4}$$

where ΔS_{mean} is the mean signal difference in a region of interest with respect to a homogeneous background area whereas σ is the standard deviation of pixel values found

in the same homogeneous background due to quantum noise. AGD is the average dose deposited in the glandular tissue of the breast. The values of ΔS_{mean}, σ and AGD were calculated according to the following three procedures:

1. **Mean signal difference:** At first the signal difference of each pixel value within a suitable region of interest to the signal level of the corresponding background signal value was determined from the images resulting from the previously described ray-tracing step. Then the mean signal difference ΔS_{mean} with respect to the homogeneous background was calculated according to

$$\Delta S_{\text{mean}} = \frac{1}{N}\sum_{n=1}^{N}\Delta S_n$$

   where $\Delta S_n = S_n - S_b$ is the signal difference of the n-th pixel of the ray-tracing image with respect to the background signal.

2. **Average glandular dose:** Then the average radiation dose deposited in the glandular tissue structures per incident photon was determined by the application of the second step of the simulation sequence mentioned above. There a sufficiently large number of x-rays have to be generated with the simulation in order to ensure a reasonably low level of statistical error for the average glandular dose per photon.

3. **Quantum noise:** Finally the third step of the simulation sequence provides information about the quantum noise present in the image due to the finite number of photons that build up the image. In accordance with the definition of the signal-difference-to-noise ratio in equation 2.36 the standard deviation of the pixel values of the simulated energy integrating detector is used as a measure of the noise in the mammograms.

Using these calculations the figure of merit given by the squared signal-difference-to-noise ratio per average glandular dose was calculated according to equation 5.4 for all of the considered x-ray sources and detection geometries. The results of these simulation sequences and calculations of the image-quality-to-dose relationship are described in detail in the next chapter. There the influence of the x-ray source parameters on this figure of merit is analyzed by using the simulation methods described in this chapter.

6 Results – Monte Carlo simulation of image formation and dose deposition in mammography

Mammography is among the first imaging modalities where laser-driven x-ray sources could be applied, as relatively low energetic x-rays in the range of 17-25 keV are typically used and are indeed optimal as shown in section 6.1. Therefore the focus of the analysis of the image formation and dose deposition process in the present work lies on mammography. Also here it is crucial to limit the radiation exposure as radiation induced breast cancer is known to occur and becomes increasingly probable as a higher radiation doses accumulate during mammography screening programs [YM11].

The main optimization problem in mammography and in radiography in general is to maximize the amount of useful information per applied radiation dose. The useful information provided by the image contrast in x-ray absorption imaging is generated by the inhomogeneous absorption of x-rays due to the object being composed of different materials with varying elemental composition and density. Since the absorption and scattering processes of x-rays have a characteristic energy dependence, as shown in figure 2.2, the image contrast as well as the quantum noise in the image, due to the finite number of photons, depend on the spectrum of the radiation. As shown in section 2.3 depending on the material composition and thickness of the imaged object there exists an optimal x-ray energy which maximizes the image quality per applied dose estimated by the previously described figure of merit.

In todays clinical practice however, mammography is based entirely on the use of polychromatic x-ray tubes. Even with modern highly optimized x-ray tubes with K-edge filtration techniques the spectrum of the generated radiation remains polychromatic, which reduces the image contrast due to high energetic x-rays and leads to an increased radiation dose due to lower energetic x-rays being absorbed almost completely. In contrast to that, the laser-driven undulator x-ray source considered in this work generates a tunable nearly monochromatic x-ray spectrum that allows the selection of an optimal x-ray energy depending on the breast thickness, composition and other parameters of the chosen mammography setup. In the context of a personalized medicine approach this allows for the optimization of the diagnostic benefit per applied radiation dose for individual patients.

Before first experiments with new x-ray sources are possible, Monte Carlo simulations

provide valuable information about the image formation and dose deposition process and therefore help to find the x-ray source parameters leading to an optimized image quality to dose ratio. In the following section 6.1 a quantitative relation between the x-ray energy and the image-quality-to-dose ratio is established for two mammographic voxel models and the x-ray energy leading to a maximal figure of merit is found. In the second section 6.2 the results of simulations of the image formation and dose deposition in mammography using undulator radiation are presented and the influence of the undulator source parameters on the x-ray spectrum and consequently on the resulting image-quality-to-dose relationship is quantified. Also the impact of the scatter reducing scanning geometry is discussed there. This is followed in section 6.3 by a comparison of the performance of the the laser-driven x-ray source for various parameters with the performance of conventional polychromatic x-ray tubes together with a quantification of the dose reduction opportunities. This shows that using optimized parameters it is possible to significantly reduce the radiation dose in mammography with an appropriate imaging setup using a laser-driven x-ray source. However the quantification of the dependence of the dose reduction potential on the relative number of photons in the higher harmonics shows that it is necessary to filter these higher energetic x-rays. Finally in the last section 6.4 it is discussed how the x-rays of the second harmonic can be filtered and the passage of the undulator x-ray beam through an angular filter is simulated.

6.1 Monoenergetic x-ray radiation: Influence of the x-ray energy on the image-quality-to-dose ratio

In this section a quantitative analysis of the influence of the x-ray energy on the image-quality-to-dose relationship in mammography is presented for different voxel models of the breast. Thereby the optimal x-ray energy for imaging each of the voxel models is determined. This is helpful in order to understand the influence of the spectral characteristics of the undulator x-ray source on the image-quality-to-dose relationship. Also this is helps to find optimized parameters for the undulator x-ray source. Using the methods described in the last section mammograms at different x-ray energies were created for the different voxel models and the squared signal-difference-to-noise ratio per average glandular dose was determined. The results are plotted in figure 6.1 where it can be seen that the chosen figure of merit $\mathrm{SDNR}^2/\mathrm{AGD}$, defined in equation 5.4, is a concave function of the x-ray energy and has a maximum at a certain x-ray energy depending on the specific voxel model. The basic properties of these curves can be understood in terms of the simple statistical model described in section 2.3. There it can be seen that the optimal signal-difference-to-noise ratio per dose is attained at a certain level of transmission. However the particular shape of the curve also depends on the

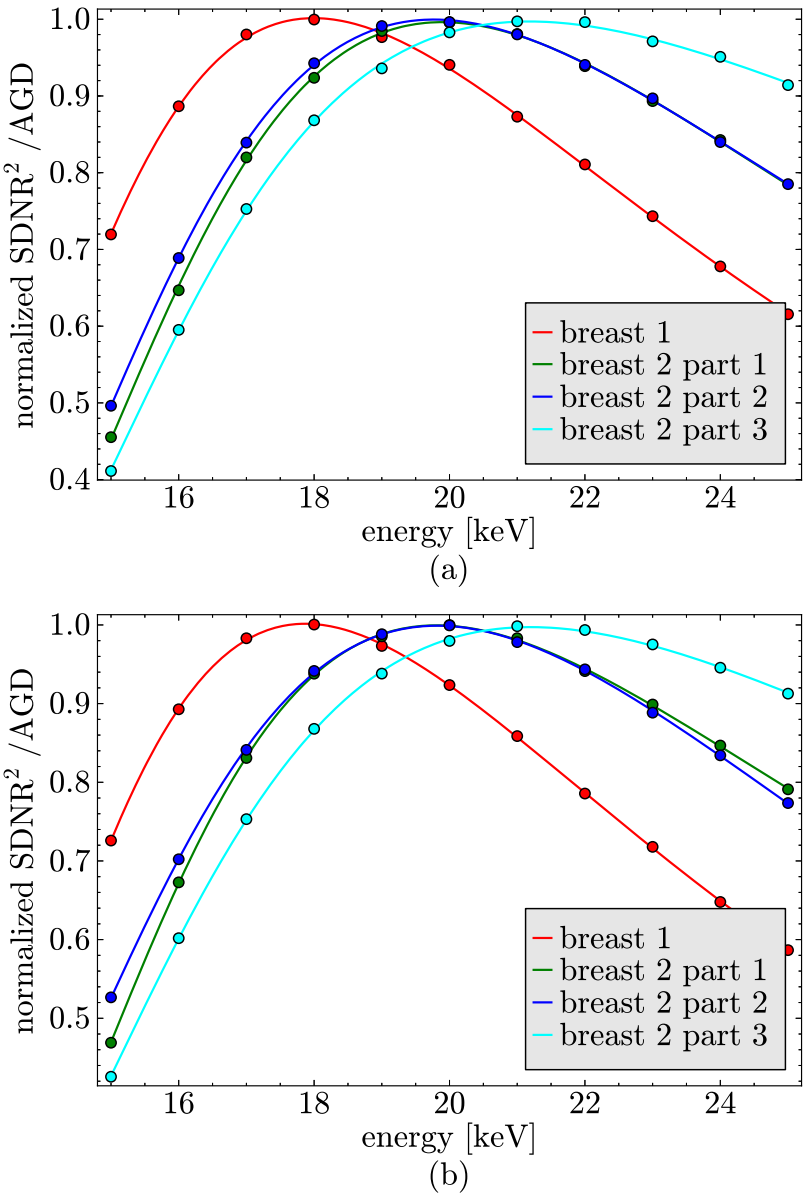

Figure 6.1: $SDNR^2/AGD$ normalized to the peak value for each voxel model plotted against the x-ray energy. Sub-figure (a) shows a plot of the normalized $SDNR^2/AGD$-energy function for primary and scattered x-rays combined while sub-figure (b) only takes into account the primary x-rays neglecting scattered radiation. These plots quantify both the influence of the breast thickness together with the glandularity and the influence of the x-ray energy on the image-quality-to-dose ratio.

elemental composition and amount of the contrast generating structures in the imaged object and also on the amount of scattered radiation. The influence of the scattered

radiation on the value of the optimal x-ray energy however is small as can be seen in table 6.1 where the energy values maximizing $\mathrm{SDNR}^2/\mathrm{AGD}$ are shown separately for the total detected x-ray radiation and for the primary transmitted radiation neglecting all scattered x-rays. While one could expect a different shape of these curves when taking into account scattered x-rays when compared to only considering primary transmitted x-rays because of the energy dependent scattering cross section the influence of this is negligible. In figure 6.1 for each plot the $\mathrm{SDNR}^2/\mathrm{AGD}$-to-energy curves corresponding to equation 2.39 are fitted to the energy dependent $\mathrm{SDNR}^2/\mathrm{AGD}$ values. These curves are in good agreement with the model developed in section 2.3. There one can also see that the steepness of these curves depends on the elemental composition of the imaged object which in the case of mammography corresponds to the ratio of glandular tissue to adipose tissue. Moreover it is also clear from equation 2.39 that the energy where the maximal $\mathrm{SDNR}^2/\mathrm{AGD}$ value is attained depends on the attenuation properties of the breast which is mainly caused by the breast thickness and to a lesser extent by the tissue composition. As can be seen in the undulator equation 2.20 the fundamental x-ray energy of the undulator x-ray source depends on the energy of the electrons in the undulator. However the resulting x-ray spectrum is not perfectly monoenergetic and its bandwidth is influenced by a number of parameters. If the electron energy is held fixed in order to get a certain fundamental x-ray energy one has two parameters left to control the bandwidth of each harmonic in the spectrum. The number of undulator periods and the slit width. Consequently in the following section the influence of these two parameters on the image-quality-to-dose ratio is discussed.

breast nr.	1	2 (part 1)	2 (part 2)	2 (part 3)
$E_{\mathrm{opt,total}}$	18.00 keV (65.80)	19.95 keV (193.3)	19.90 keV (27.00)	21.25 keV (0.9241)
$E_{\mathrm{opt,primary}}$	17.89 keV (93.08)	19.94 keV (294.4)	19.92 keV (39.88)	21.25 keV (1.363)

Table 6.1: Optimal energy E_{opt} maximizing $\mathrm{SDNR}^2/\mathrm{AGD}$ which is shown in brackets after the energy in units of 1/mGy. The numbered columns correspond to the different voxel models. The values have been obtained by calculating the maximum of the fitted curves plotted in figure 6.1.

6.2 Influence of the undulator x-ray source parameters on the image-quality-to-dose ratio

In this section the results of various imaging simulations of mammography with the undulator x-ray source using the previously described simulation methods are presented. Thereby the influence of the different parameters of the undulator x-ray source on the image-quality-to-dose relationship is quantified in relation to those images and dose values obtained by using an optimal monoenergetic spectrum. At first a quantification of the dependence of the image-quality-to-dose ratio on the slit width and on the number of undulator periods is given. Then the influence of the higher harmonics in the spectrum of the undulator x-ray source on the image-quality-to-dose ration is discussed and the influence of the undulator magnetic field strength resulting in the production of x-rays in the higher harmonics on the image-quality-to-dose ratio is quantified. Then in the final sub-section a quantification the impact of the scatter reducing scanning geometry on the resulting image quality and dose values is given.

6.2.1 Influence of the number of undulator periods

As discussed in chapter 2 the spectral bandwidth depends on certain parameters of the x-ray source. At first there is the on-axis spectral bandwidth which is influenced by the number of undulator periods as shown in subsection 3.3.2 and as can be seen easily in figure 3.8. As the spectral width quickly drops well below a few percent for the number of undulator periods being above 20 the influence of the number of undulator periods on the resulting image-quality-to-dose ratio is very small as can be seen in figure 6.2. For a reasonably high number of undulator periods this parameter of the x-ray source is therefore only important because of its influence on the total number of x-rays that are generated inside the undulator.

6.2.2 Off-axis contributions: Influence of the slit width

In order to model the image formation process resulting from the the setup described in section 3.1 also the influence of the slit has to be considered and consequently the total spectrum of the x-rays that pass through a slit with a certain width is of interest here. Therefore the off-axis part of the x-ray beam together with the angular dependence of the x-ray energy as described by the fundamental undulator equation 2.20 has to be taken into account. This results in an increased spectral width as the width of the slit is increased because the off-axis contributions become relevant and also leads to a slightly lower mean x-ray energy as shown in subsection 3.3.3. Consequently also the image-quality-to-dose relationship strongly depends on the slit width. This was quantified by simulating mammography with the undulator x-ray source at different slit widths and

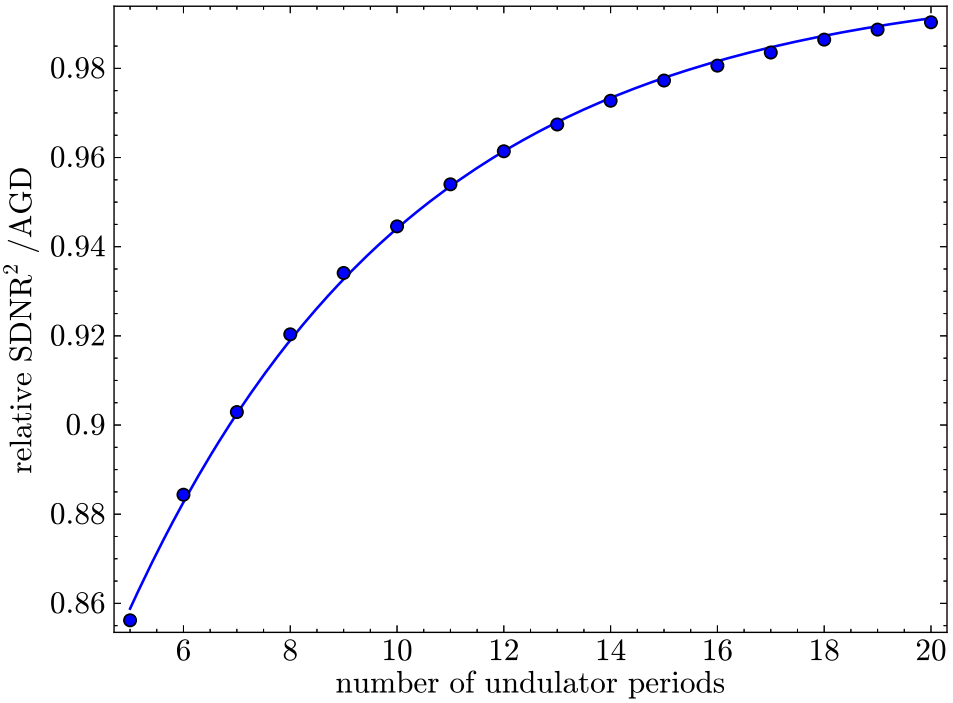

Figure 6.2: SDNR^2/AGD relative to the SDNR^2/AGD for an infinite number of undulator periods plotted against the number of undulator periods for the first breast and a mean x-ray energy of 18 keV. Here an slit width of 0.1 mm has been assumed in order to only take into account on-axis x-rays. Also the higher harmonics in the spectrum have been neglected.

the results can be seen in figure 6.3. There it can also be seen that the effectivity of the slit blocking vertically off-axis photons decreases as the slit width approaches zero. This is due to the laminar beam geometry whereby x-rays that are only horizontally off-axis can always pass the slit and only the vertically off-axis x-rays can be filtered by the slit. In the opposite limit of a large slit width the signal-difference-to-noise ratio per average glandular dose converges to the value obtained when using the full undulator spectrum without any angular restriction.

This shows that in order to obtain a good image quality per applied dose using the considered laser-driven x-ray source it is critical to filter the off-axis contributions of the x-ray beam. The most simple way to achieve this is by using a slit blocking vertically off-axis x-rays and as shown in figure 6.3 does this effectively for widths smaller than 0.5 mm. However the angular dependence of the undulator spectrum is not the only part that deviates from the fundamental x-ray energy. Also the higher harmonic contributions influence are far away from the optimal x-ray energy and consequently have a negative impact on the image-quality-to-dose relationship as discussed in the next sub-section.

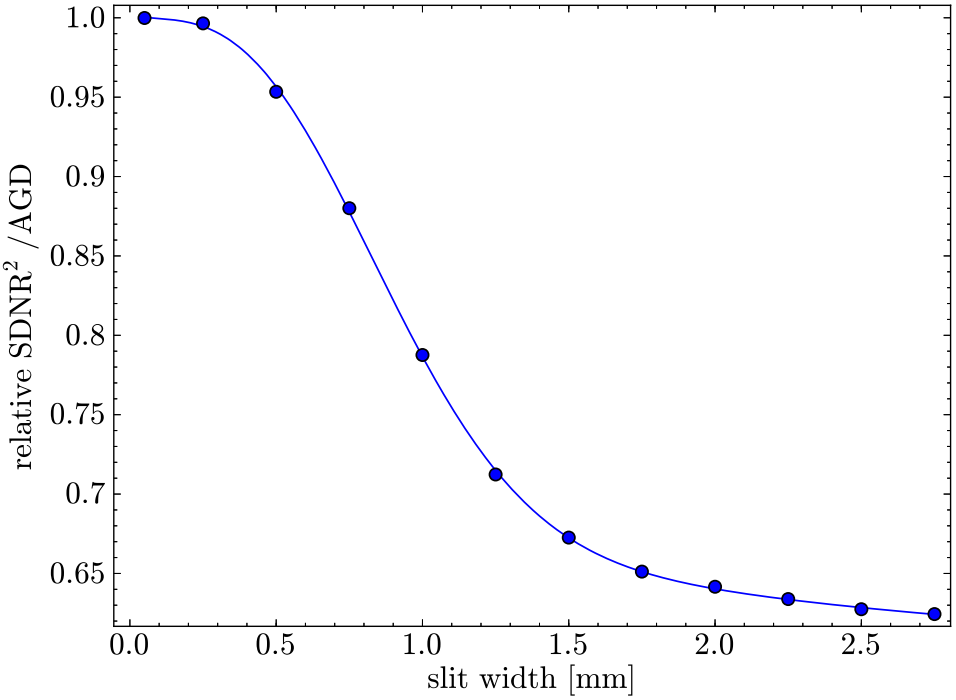

Figure 6.3: SDNR^2/AGD relative to the SDNR^2/AGD in the limit where only vertically on-axis radiation is present plotted against the slit width. The position of the slit is assumed to be at 4 m after the undulator exit. The specific SDNR^2/AGD values were obtained for the first breast model by calculating the spectrum of the undulator x-ray source for the respective slit widths while adjusting the electron energy in order to get an optimal mean x-ray energy in the fundamental of 18 keV. The sum of a Gaussian and of a decaying exponential has been fitted to the values in order to model the system.

6.2.3 Higher harmonics: Influence of the magnetic field strength

In subsection 3.3.5 it is shown that the number of photons in the higher harmonic modes relative to the fundamental mode depends on the magnetic field strength inside the undulator. As can already be seen in figure 6.1 these higher x-ray energies are far from the energy optimal for mammography. This is caused by the fact that the attenuation coefficient of the soft tissues in the breast at these energies is much lower than at the optimal energy and therefore also the difference in the attenuation coefficients for different materials gets very small. Despite the fact that the absorption probability of these photons and therefore the probability to deposit dose in the glandular tissue is lower at these energies, when compared to the fundamental energy, the dose per photon is higher. More importantly however the noise at the detector side caused by these transmitted photons is the critical factor and reduces the image quality drastically.

This can also be understood in terms of the model described in section 2.3 and can easily be seen in figure 2.3. The impact of the x-rays of the higher harmonics and the dependence on the magnetic field strength were quantified by simulating mammography with different undulator spectra corresponding to different values of the magnetic field strength. The results are plotted in figure 6.4. This shows that it is absolutely crucial

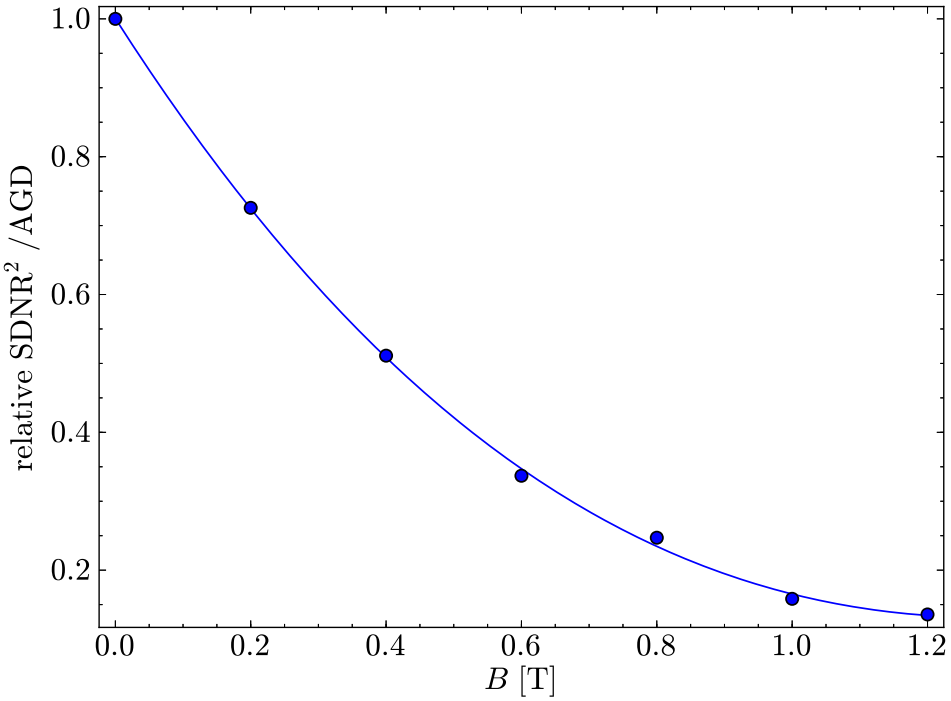

Figure 6.4: SDNR^2/AGD relative to the SDNR^2/AGD obtained in the limit of vanishing magnetic field strength plotted against the magnetic field strength. The plot corresponds to simulations with the first breast voxel model and an undulator spectrum with a mean x-ray energy of the fundamental of 18 keV at a slit width of 0.1 mm. The electron energy leading to a mean energy of 18 keV in the fundamental had to be adjusted for each value of the magnetic field strength as the fundamental x-ray energy depends on the magnetic field strength according to equation 2.20.

to minimize the influence of the higher harmonics in order to obtain a good image-quality-to-dose ratio in mammography. This can either be done by filtering the higher x-ray energies by using a monochromator as discussed in sub-section 6.4 or by using an energy-sensitive detector capable of setting an energy cut-off which however would not eliminate the dose caused by these higher energetic x-rays.

6.2.4 Influence of the scanning geometry

One advantage of the type of laser-driven x-ray source considered in this work is the low divergence of the produced x-rays which are emitted in forward direction. Using the electron optics setup described in sub-section 3.2.3 it is possible to create a laminar beam which is ideally suited to perform x-ray imaging using a scanning geometry in which the horizontally spread beam scans the breast in the vertical direction. It is also conceivable that the scanning could be done by adjusting the electron optic leading to a deflection of the electron beam and consequently also of the x-ray beam with hardly any mechanical movement involved. This scanning geometry has the advantage that a considerable amount of scattered x-ray is separated spatially from the transmitted x-rays in the vertical direction and can therefore be discarded. This leads to significantly less noise in the resulting images and consequently to a higher image-quality-to-dose ratio. The suppression of scattered x-rays in the recorded image created by using a scanning geometry was simulated by using the previously described methods, together with a modified detection process where all scattered x-rays hitting the detector at a position greater than the scan width are discarded. In figure 6.5 the dependence of the image-quality per average glandular dose on the scan width is shown. There one can

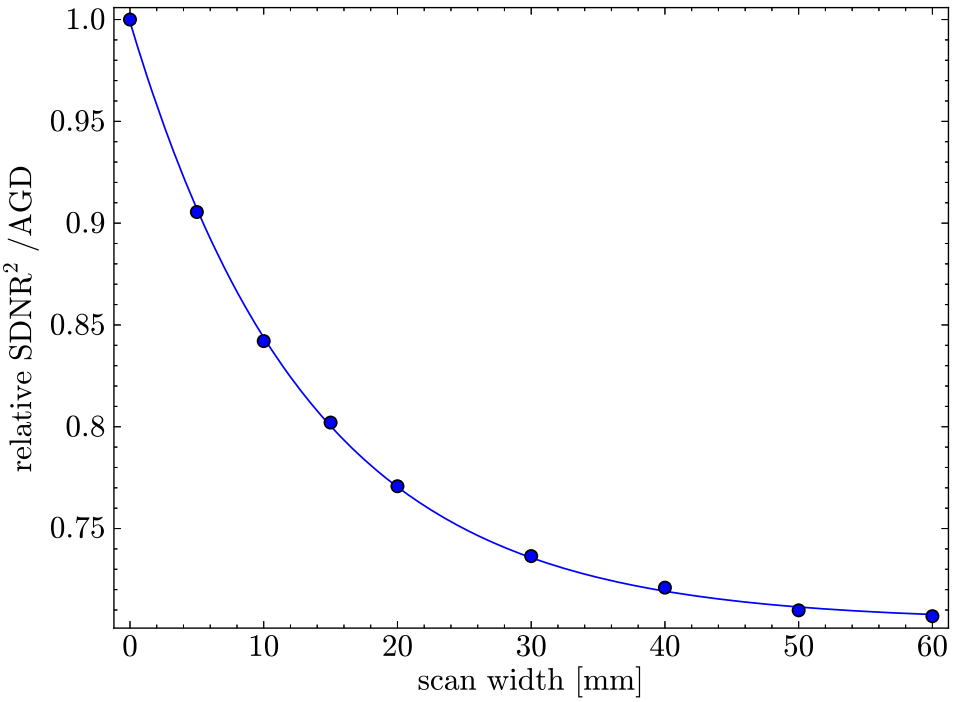

Figure 6.5: SDNR^2/AGD relative to the SDNR^2/AGD obtained in the limit where only primary x-rays contribute to the image formation and all scattered x-rays are discarded plotted against the scan width.

see that for a scan width below 5 mm the image-quality per average glandular dose approaches the limit where all scattered x-rays are discarded. In the opposite limit of a large scan width the image-quality per average glandular dose naturally converges to the case where no scattered x-rays are filtered out.

It has to mentioned here that there are methods of reducing the scattered radiation which are already clinically applied in radiography [Bar91, BM04]. One method is to use an anti-scatter grid composed of a radio-opaque material e.g. lead strips that are aligned towards the x-ray tubes focal spot. However there are difficulties involved in aligning the lead strips and a signal reduction that is caused by the attenuation of x-rays by the grid spacing material. It has also been suggested that for thin breasts where the scatter-to-primary ratio and the optimal x-ray energy is lower the usage of an anti-scatter grid may actually be disadvantageous because of the signal loss caused by the grid [BMH06, DD84]. In contrast to this the scanning geometry presented here does not have this disadvantage. Another method of reducing scattered radiation is by using an air gap between the breast and the detector. The air gap as well as anti-scatter grids however only effectively reduce Compton scattering as Rayleigh scattering, which in mammography is a considerable factor, occurs at relatively low scattering angles [JY83]. Also the use of an air gap introduces magnification and therefore leads to blur because of the finite focal spot size of x-ray tubes as discussed in section 6.5. In contrast to this a large air gap is no problem for an imaging setup using an the undulator x-ray source because of its low divergent x-ray beam. Yet another method of reducing the scattered radiation in mammography is to use a so called slot scanning geometry [Bar77] which has been proposed very early [Pas03] and has been successfully applied to mammography [YBK81]. This however has the disadvantage that high tube loads and increased exposure times have to be used because much of the tubes output is discarded. This in contrast is not the case for the undulator x-ray source considered in this work as the beam is naturally collimated.

6.3 Dose reduction potential of quasi-monochromatic x-rays relative to x-ray tube radiation

In the previous sections of this work the influence of the x-ray energy of a monochromatic x-ray source was discussed and a quantification of the different parameters of the quasi-monochromatic undulator x-ray source on the image-quality-to-dose ratio in mammography was given. Based on this analysis a comparison of the imaging performance of these sources to the performance of x-ray tubes typically used in mammography is presented in this section.

6.3.1 Image-quality-to-dose ratio for undulator x-rays and x-ray tube radiation relative to monoenergetic x-rays

At first mammography was simulated with a monochromatic x-ray source set to the previously determined optimal x-ray energies shown in table 6.1. The results of these simulations were then used as reference for the simulations using the quasi-monochromatic undulator x-ray source and for the simulations using various x-ray tube spectra. The values of the figure of merit $SDNR^2/AGD$ corresponding to the different x-ray sources and voxel models relative to the $SDNR^2/AGD$ obtained with the optimal monochromatic x-ray source can be found in table 6.2. The relative $SDNR^2/AGD$ of the laser-driven undulator x-ray source reaching up to 0.94 indicates that the quasi-monochromatic spectrum leads to an image-quality-to-dose ratio close to that of an ideal monoenergetic x-ray source. The small remaining difference results from the laminar beam geometry where a small amount of lower energetic photons being horizontally off-axis can pass the slit which discussed in detail in sub-section 3.3.3. Also, as described in the last section optimized parameters of the undulator x-ray source have to be chosen in order to reach an image-quality-to-dose ratio comparable to mono-energetic x-ray sources.

In contrast to the undulator x-ray source the spectrum of an x-ray tube can not be extensively tuned to become quasi-monochromatic. The working principle of x-ray tubes basically only allows tuning the spectrum by selecting the anode material together with the voltage and additionally by using a filtration of the generated x-rays with a material of a certain thickness. In table 6.2 also the relative $SDNR^2/AGD$ values for different x-ray tube parameters are shown.

While the relative $SDNR^2/AGD$ value for the undulator x-ray source always lies at about 0.93 the $SDNR^2/AGD$ value corresponding to the different x-ray tube spectra depends on the specific voxel model. The different thicknesses and glandularities of the voxel models results in different x-ray spectra being optimal. For the first breast which has the smallest thickness for example a spectrum resulting from choosing a molybdenum anode at a peak kilovoltage of 28 kVp together with a molybdenum filter with a thickness of 30 µm is optimal while for the thicker voxel models either the spectrum corresponding to a tungsten or molybdenum anode together with a rhodium filter is optimal.

For all of the different voxel models the optimal x-ray tube spectrum leads to a relative $SDNR^2/AGD$ value of about 0.6. Using these values it is possible to estimate the dose reduction potential in mammography when using an undulator x-ray source when compared to standard mammography using x-ray tubes which is done in the next sub-section.

breast 1	mono	undulator	Mo28/Mo30	Mo32/Mo30	W34/Rh50	W42/Rh50	Mo28/Rh25
total	1 (65.9)	0.922 (60.7)	0.603 (39.7)	0.520 (34.3)	0.579 (38.1)	0.359 (23.7)	0.419 (27.6)
primary	1 (94.9)	0.921 (87.4)	0.602 (57.1)	0.518 (49.2)	0.581 (55.2)	0.356 (33.8)	0.419 (39.8)

breast 2/1	mono	undulator	Mo28/Mo30	Mo32/Mo30	W34/Rh50	W42/Rh50	Mo28/Rh25
total	1 (193)	0.928 (179)	0.570 (110)	0.466 (90.0)	0.603 (116)	0.376 (72.6)	0.623 (120)
primary	1 (294)	0.938 (276)	0.572 (168)	0.469 (138)	0.608 (179)	0.377 (111)	0.628 (185)

breast 2/2	mono	undulator	Mo28/Mo30	Mo32/Mo30	W34/Rh50	W42/Rh50	Mo28/Rh25
total	1 (27.0)	0.935 (25.3)	0.551 (14.9)	0.467 (12.6)	0.605 (16.3)	0.382 (10.3)	0.599 (16.2)
primary	1 (39.9)	0.943 (37.6)	0.554 (22.1)	0.471 (18.8)	0.604 (24.1)	0.377 (15.0)	0.605 (24.1)

breast 2/3	mono	undulator	Mo28/Mo30	Mo32/Mo30	W34/Rh50	W42/Rh50	Mo28/Rh25
total	1 (0.92)	0.939 (0.87)	0.498 (0.46)	0.447 (0.41)	0.601 (0.56)	0.430 (0.34)	0.562 (0.52)
primary	1 (1.4)	0.944 (1.3)	0.499 (0.68)	0.447 (0.61)	0.609 (0.83)	0.433 (0.59)	0.561 (0.76)

Table 6.2: $SDNR^2/AGD$ for an optimized undulator spectrum and for various typical tube spectra used in mammography relative to the $SDNR^2/AGD$ obtained with the optimal monoenergetic spectrum. (The absolute values of $SDNR^2/AGD$ are shown in brackets.) The values for the undulator x-ray source correspond to a setup with a 0.1 mm slit width which results in a quasi-monochromatic spectrum with a standard deviation from the fundamental energy of about 1.3 keV. Also it has been assumed that the higher harmonics have been suppressed. The values of the last five columns correspond to different x-ray tube spectra where Mo28/Mo30 for example is an abbreviation for a Molybdenum anode at a peak kilovoltage of 28 kVp and a Molybdenum filter of 30 µm thickness while W34/Rh50 is an abbreviation for a tungsten anode at a peak kilovoltage of 34 kVp together with a Rhodium filter of 50 µm thickness. The filter thicknesses have been chosen to yield a comparable flux between the different considered spectra whereby the tungsten spectra have been selected with a larger filter thickness than the molybdenum spectra.

6.3.2 Quantification of the dose reduction potential of undulator radiation relative to x-ray tube radiation

The average glandular dose needed for a certain signal-difference-to-noise ratio can be directly calculated from the figure of merit $SDNR^2/AGD$, introduced in sub-section 5.2.9. Consequently the ratio of the average glandular dose needed for this signal-difference-to-noise ratio when using the x-ray undulator to the average glandular dose needed when using an x-ray tube can be determined from the values found in table 6.2.

breast 1	Mo28/Mo30	W34/Rh50
no scanning	0.654	0.629
scanning	0.455	0.345

breast 2/1	Mo28/Rh25	W34/Rh50
no scanning	0.671	0.650
scanning	0.437	0.422

breast 2/2	W34/Rh50	Mo28/Rh25
no scanning	0.650	0.641
scanning	0.435	0.430

breast 2/3	W34/Rh50	Mo28/Rh25
no scanning	0.641	0.599
scanning	0.431	0.403

Table 6.3: Ratio of the average glandular dose resulting from mammography with the undulator x-ray source to the average glandular dose resulting from mammography with different optimized x-ray tube spectra. The sub-tables correspond to the different voxel models. The first row contains values for the dose ratio obtained for using the undulator x-ray source without the scanning geometry while the second row contains values obtained for taking into account the scatter reduction of the scanning geometry.

In table 6.3 the ratio of the average glandular dose corresponding to an exposure with the x-ray undulator source to the average glandular dose resulting from an x-ray tube exposure resulting in an image with the same signal-difference-to-noise ratio is shown. There the x-ray tube spectrum which is optimal for each of the different voxel models is chosen in order to obtain a meaningful comparison. From the values shown in table 6.3 it can be seen that the average glandular dose in mammography can be reduced by a factor of about 2.3 when using an undulator x-ray source instead of an x-ray tube. It can also be seen that for the thicker voxel models the impact of the scanning geometry is more pronounced as there the scatter-to-primary ratio is higher [BLIS00] and the filtering of the scattered x-rays provides an increased signal-to-noise ratio. As discussed already in sub-section 6.2.4 this has to be compared with the efficiency of existing methods of reducing the scattered radiation. The use of anti-scatter grids commonly used in todays mammography for example can be ineffective for thin breasts and lead to a higher dose

as shown in [BMH06].

6.3.3 Off-axis contributions: Influence of the slit width on the dose reduction potential

As the dose reduction gained by using quasi-monochromatic x-rays depends on the bandwidth of the quasi-monochromatic spectrum it is interesting to quantify the influence of the lower energetic off-axis x-rays which are present in the spectrum of the undulator x-ray source. As shown in the previous section of this work these x-rays can be filtered by using a slit. In figure 6.6 it can be seen that the dose reduction gained from using an undulator x-ray source instead of a conventional x-ray tube strongly depends on the ability to filter the off-axis x-rays.

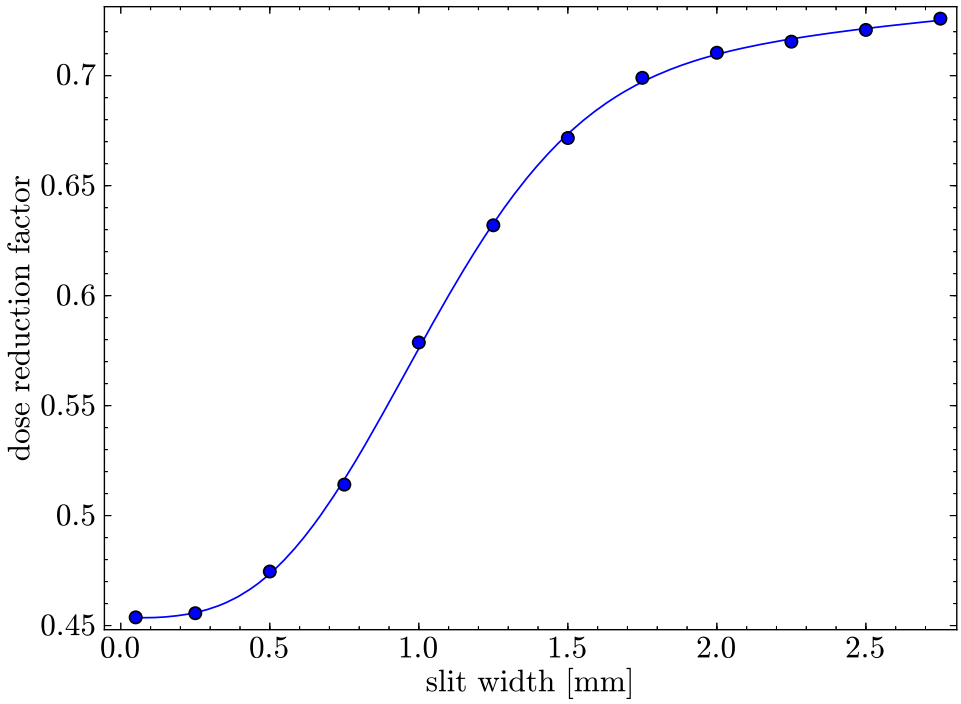

Figure 6.6: Dose reduction factor relative to the optimized tube spectrum plotted against the slit width for the first breast. The scatter reducing scanning geometry for the undulator x-ray source has been taken into account here.

6.3.4 Higher harmonics: Influence of the magnetic field strength on the dose reduction potential

Besides the influence of the off-axis x-rays the influence of the x-rays in the higher harmonics is also critical. As shown in sub-section 3.3.5 the amount of x-rays in the higher harmonics relative to the fundamental increases with increasing magnetic field

strength and as can be seen in 6.7 the dose reduction factor for the undulator x-ray source becomes worse for a higher magnetic field strength. As discussed in sub-section 6.2.3 this is due to the higher energetic x-rays producing almost no contrast while greatly increasing the noise at the detector. Therefore for a value of the magnetic field strength above approximately 0.5 T the dose required to produce a certain image quality is even higher than the dose deposited during a conventional mammography. Therefore it is obvious that it is crucial to filter the higher energetic x-rays.

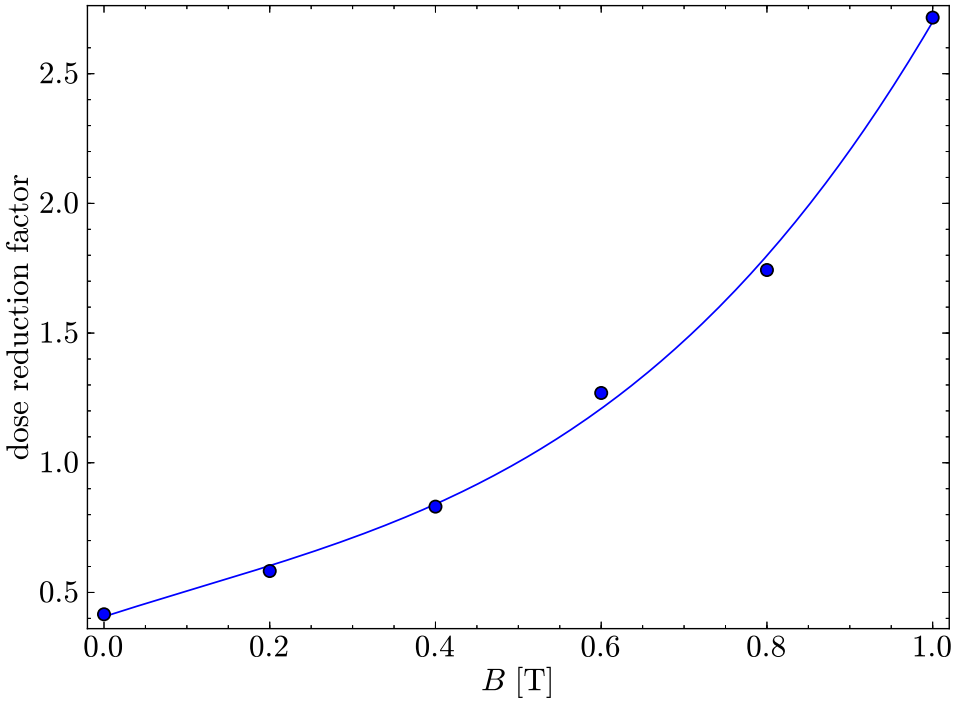

Figure 6.7: Dose reduction factor relative to the optimized tube spectrum plotted against the magnetic field strength for the first breast. The scatter reducing scanning geometry for the undulator x-ray source has been taken into account here.

6.4 Reduction of the second harmonic: Monte Carlo simulation of an angular filter

In the previous section it was shown that the higher energetic x-rays in the second harmonic are absolutely detrimental to the image quality and that it would be necessary to filter these x-rays in oder to obtain any dose reduction in mammography when compared to polychromatic x-ray tubes. Therefore it is worthwhile investigating methods of reducing the number of x-rays in the beam which belong to the higher harmonics.

As can be observed in figure 3.7 and as explained in section 2.1.6 the second harmonic

and all other even harmonics only contain off-axis x-rays. This opens up the possibility to apply an angular filter in order to filter out all x-rays in the higher energetic second harmonic which are emitted at higher angles. Additionally this would also reduce the number of lower energetic x-rays in the fundamental mode which are emitted at higher angles too. In a laminar beam these off-axis x-rays are always present even for an infinitesimal vertical slit width because these x-rays can pass the slit in the horizontal direction.

There are a number of conceivable methods for the angular filtering of x-rays. One option would be to use an analyzer crystal as used in the so called analyzer based imaging [Bra03] with a certain angular acceptance with respect to a certain Bragg reflection tuned to the fundamental energy. This would only reflect the on-axis component of the fundamental. Another option would be to use polycapillary x-ray optics which filters x-rays by total external reflection [GHN01] and would reject all x-rays emitted at higher angles.

However as both of these methods can be problematic for higher energetic x-rays, a more simple method of angular filtering would be to use a so called Soller slit collimator [Sol24] consisting of slats of an absorber material which are precisely aligned in the direction of the x-ray beam. Those slats would then absorb all off-axis x-rays while the on-axis part of the spectrum is not affected. The comprehensive calculation of the properties of the undulator x-ray beam described in section 3.4 and its implementation in a simulation using the Geant4 software toolkit as described in sub-section 5.2.3 is ideally suited for investigating the passage of the x-rays through such an angular filter. A simulation of this was done by using the same undulator beam data as applied to the mammography simulations described in the previous sections together with an implementation of a Soller slit collimator in the simulation. Figure 6.8 shows a section of the beam and filter geometry where it can be seen that the collimator slats were implemented with an angular dependence which is tuned to the beam divergence in the horizontal direction so that for each horizontal position the collimator slats are parallel to the mean x-ray path at this position. As the x-rays of the even harmonics still are produced at very small angles in the order of 50 µrad the distance between the collimator slats has to be in the order of 1 µm and the length of the slits has to be in the order of several cm in order to be effective. While the production of Soller slit collimators with such small openings is in no way straight forward it has been shown that micro fabrication processes can reach such small dimensions [ACKH98]. The passage of the undulator x-ray beam through a Soller slit collimator with such dimensions was simulated and the total spectrum of the filtered beam was calculated as can be seen in figure 6.9 for a collimator slat spacing of 1 µm. There it can be seen that this collimator effectively rejects most of the x-rays from the second harmonic and also reduces the bandwidth of the fundamental.

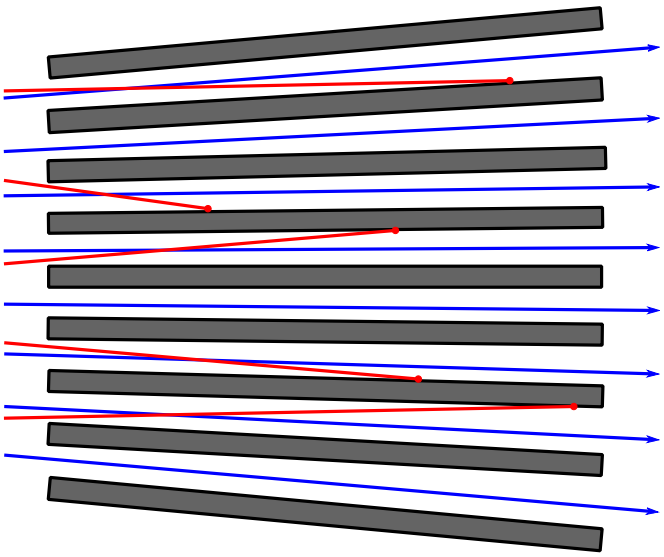

Figure 6.8: Passage of x-rays of the beam exiting the undulator through a Soller slit collimator. The collimator slats have an angular dependence adjusted to the beam geometry which results in the transmission of on-axis x-rays (blue) and the rejection of off-axis x-rays (red).

Unfortunately however the simulations have shown that the collimator not only reduces the flux of the unwanted off-axis x-rays but also of the on-axis x-rays in the fundamental. This results from the finite width of the collimator slats and potentially also from the angular alignment of the slats being not optimally adjusted to the x-ray beam geometry in the horizontal direction.

6.5 Spatial resolution properties

In the previous sections the image quality analysis was done using a figure of merit based on the signal-to-noise ratio. For medical imaging however also the spatial resolution that can be achieved by the imaging setup is of importance. This is especially the case in mammography were radiologists need to see fine structures as well as microcalcifications in order to differentiate between pathological and healthy tissue [PYK03].

For imaging with x-ray tubes the spatial resolution is essentially determined by the focal spot size and the magnification factor. In the case of the undulator x-ray imaging setup described in this work the spatial resolution that can be achieved depends on the divergence of the x-ray beam and on the magnification factor too. The divergence of the undulator x-ray beam is caused by two effects. On the one hand the divergence and the energy spread of the initial electron beam resulting from the laser-wake-field acceleration process combined with the energy dependent electron focusing directly leads to a divergent x-ray beam and on the other hand the angular spread of the undulator

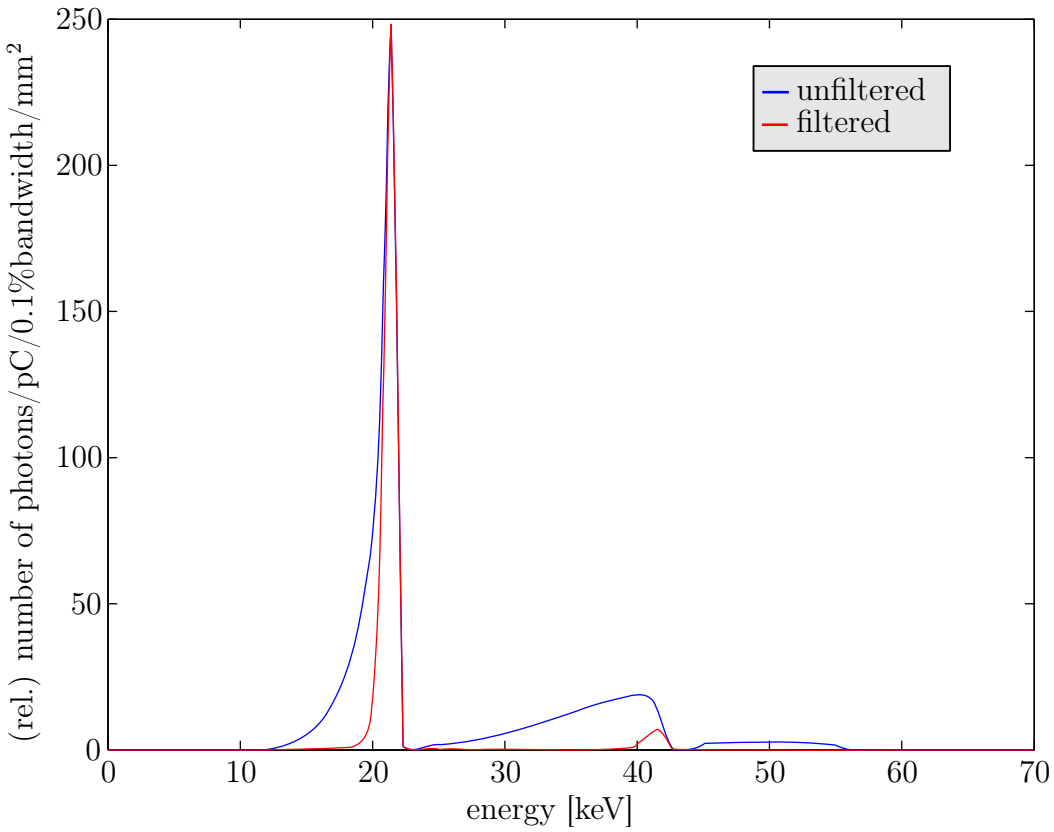

Figure 6.9: Spectrum of the unfiltered and filtered x-ray spectrum of the total x-ray beam reaching the detector. The collimator slat spacing is 1 µm and the spectrum is collected over 20 mm^2. Note that the values of the spectral flux corresponding to the unfiltered spectrum are the absolute values recorded by the detector while the values corresponding to the filtered spectrum are scaled relative to the unfiltered spectrum by a factor of about 5.

radiation estimated by equation 2.24 contributes to the divergence of the x-ray beam.

The methods used for simulating the imaging process with x-ray tubes and the implementation of the undulator x-ray beam described in sub-section 5.2.3 take into account both the effect of a finite focal spot size as well as the beam divergence for the undulator x-ray source and therefore allow for the analysis of these factors on the achievable spatial resolution. For a small distance of the breast to the detector and hence a low magnification factor no blur and no reduction in the visibility of small structures could be seen in the images resulting from simulations with the undulator x-ray source, at least for a voxel size of about 50 µm. This can be understood in terms of the assumption of a sufficiently low electron divergence and from the estimate of the angular spread

provided by equation 2.24 which shows that for large electron energies over 1 GeV and a sufficiently high number of undulator periods this angular spread becomes negligible.

In contrast to this simulations using the x-ray tube implementation with a focal spot size of over 0.3 mm showed a reduced visibility of small structures. An analysis of the spatial resolution properties using the simulation developed in this work can be found in [MSGH11] where a different voxel model [HFZ05] was used in order to apply an image quality analysis method based on the methods developed in [Hoe02].

While currently available x-ray tubes provide a sufficiently small focal spot size for non-magnified imaging setups in mammography the situation is different for a higher magnification factors. In this case the simulations clearly showed a difference between the images simulated with the x-ray tube implementation and the images simulated with the undulator x-ray beam implementation. The improved detectability of fine structures when imaging with a low-divergent undulator x-ray beam would also benefit from the improved contrast generation and scatter reduction which is quantified in section 6.2. In order to quantify this however a generalized figure of merit such as a frequency dependent signal-difference-to-noise ratio as described in [Hoe02, BBRH05] should be used.

7 Conclusion and Outlook

In this work the application of a novel table-top sized laser-driven undulator x-ray source to mammography was investigated. As first experiments demonstrated already that this type of x-ray source is capable of producing soft x-rays [FWP09] it is reasonable to assume that with further advances in the field of laser-driven electron acceleration higher x-rays could be reached. Therefore the focus in this work lies on mammography as one of the first imaging modalities that are feasible at a relatively moderate x-ray energy range. Before first experiments in the field of medical imaging with these sources come into reach the analysis of the x-ray beam creation and the simulation of the image formation and dose deposition process for these x-ray sources as done in this work provides insight into the requirements for an optimized application in the field of mammography and give a quantitative analysis of the benefits.

The calculation of the electron dynamics influenced by the electron optic and of the x-ray beam creation in the undulator shows that using an optimized beam line setup it is possible to create a laminar quasi-monoenergetic x-ray beam suitable for mammography. The difficulties involved in optimizing this beam for a narrow spectral bandwidth and for imaging a relatively large area in a practicable time is discussed and the influence of the x-ray source parameters on these requirements is quantified. It is shown that using a double quadrupole configuration the length of the second quadrupole is the critical factor in achieving a laminar beam profile and the dependence of the beam profile width on the quadrupole length is quantified. Based on this, a detailed calculation of the x-ray creation in the undulator was done which gives information about the spatio-spectral x-ray distribution and of the beam geometry.

Building upon these calculations a Monte Carlo simulation of the image formation and dose deposition process in mammography was developed in order to quantify the performance of the undulator x-ray source in mammography. Already a simple analytical model of the relationship between the image-quality-to-dose ratio and the x-ray energy developed in this work shows that there exists an optimal energy for a certain imaging task and provides an estimate of the dose reduction opportunities for using an optimized quasi-monoenergetic x-ray source when compared to polychromatic x-ray tube spectra. In order to quantify the performance of the undulator x-ray source and the influence of its parameters on the image-quality-to-dose relationship in mammography in detail a simulation implementing a realistic model of the breast and of the x-ray beam characteristics was developed. Two specimens of female breasts from anatomical courses were scanned in a high resolution CT and the resulting data was segmented in order to create

voxel models containing all relevant glandular structures present in the breast at a high level of detail. These voxel models were implemented in the simulation using a method of translating the gray values of the voxel model to the corresponding tissue and elemental composition. Using the calculations of the x-ray beam creation and implementing a model of the undulator x-ray source allowed for a detailed simulation of mammography using this source. Thereby all characteristic features of this quasi-monoenergetic x-ray source such as the spatio-spectral x-ray distribution, divergence properties and beam geometry and their influence on the resulting image quality properties and dose levels were simulated. The influence of the number of undulator periods, of the slit width and of the higher harmonics in the spectrum on the resulting image-quality-to-dose ratio is quantified and thereby provides an analysis of the requirements for achieving a high image-quality-to-dose ratio when using an undulator x-ray source.

It is shown that using optimized parameters of the undulator x-ray source, thereby controlling the number of the off-axis photons and minimizing the number of photons in the second harmonic, leads to a quasi-monochromatic spectrum which together with the scatter reducing scanning geometry allows for a reduction of the glandular dose in mammography by a factor of about 2.3 even when compared to highly optimized x-ray tube spectra. With further advances in the construction of table-top sized brilliant x-ray sources this would provide for the first time the opportunity to bring the advantages as seen for synchrotron radiation at large research facilities into the clinical practice and would be an important step towards a reduction of the patients' radiation dose from radiological examinations in the future.

Low-dose imaging will also just be the starting point as those sources open up the opportunity to do a number of more advanced imaging techniques that are also applicable in other fields besides breast imaging like dual energy and perfusion imaging. Using our approach of simulating x-ray absorption imaging in detail using a Monte Carlo simulation without further approximations provides a valuable foundation for the investigation of these imaging techniques using brilliant x-ray sources. The simulation developed in this work has already been extensively used in order to simulate novel spectral imaging techniques using contrast agents and will be further developed for more advanced energy resolved detection geometries. The analysis of scatter imaging techniques and K-edge imaging with the contrast agents iodine and gold nanoparticles making use of the energy-to-angle dependence of the undulator x-ray source shows great promise and will be the subject of further studies.

Bibliography

[A03] S. Agostinelli et al. Geant4: a simulation toolkit. *Nuclear Instruments and Methods in Physics Research A*, 506:250–303, 2003.

[ACKH98] Brendan E. Allman, Alberto Cimmino, Anthony G. Klein, and William A. Hamilton. Metal microarrays for collimating neutrons and x rays. *Proc. SPIE, X-Ray Microfocusing: Applications and Techniques, 175*, 3449:175–184, 1998.

[Ang04] W. Angerstein, editor. *Grundlagen der Strahlenphysik und der radiologischen Technik in der Medizin.* H. Hoffmann Verlag, 2004.

[Bac98] John Backus. The History of Fortran I, II, and III. *IEEE Ann. Hist. Comput.*, 20(4):68–78, October 1998.

[Bar77] G. T. Barnes. Reduction of scatter in diagnostic radiology by means of a scanning slit assembly. *Japanese Journal of Radiological Technology*, 32(6):636, March 1977.

[Bar91] G. T. Barnes. Contrast and scatter in x-ray imaging. *Radiographics*, 11(2):307–323, 1991.

[BBRH05] P. Bernhardt, L. Bätz, E.-P. Rührnschopf, and M. Hoheisel. Spatial frequency-dependent signal-to-noise ratio as a generalized measure of image quality. *Proceedings of SPIE*, 5745:407–418, 2005.

[BCDM95] E. Burattini, E. Cossu, C. Di Maggio, M. Gambaccini, P. Indovina, M. Marziani, M. Pocek, S. Simeoni, and G. Simonetti. Mammography with synchrotron radiation. *Radiology*, 195:239–244, 1995.

[BEI06] BEIR. *Committee to Assess Health Risks from Exposure to Low Levels of Ionizing Radiation, National Research Council. Health Risks from Exposure to Low Levels of Ionizing Radiation: BEIR VII Phase 2.* The National Academies Press, 2006.

[Ber90] M. Berz. *COSY INFINITY Reference Manual.* Lawrence Berkeley Laboratory, University of California, Accelerator & Fusion Research Division, 1990.

[BHS10] M. J. Berger, J. H. Hubbell, S. M. Seltzer, J. Chang, J. S. Coursey, R. Sukumar, D. S. Zucker, and Olsen. XCOM: Photon Cross Sections Database. *NIST Standard Reference Database 8 (XGAM)*, 2010.

[BLIS00] John M. Boone, Karen K. Lindfors, Virgil N. Cooper III, and J. Anthony Seibert. Scatter/primary in mammography: Comprehensive results. *Medical Physics*, 27(10):2408–2416, 2000.

[BM04] H. H. Barrett and K. J. Myers. *Foundations of image science*. Wiley series in pure and applied optics. Wiley-Interscience, 2004.

[BMH06] Philipp Bernhardt, Thomas Mertelmeier, and Martin Hoheisel. X-ray spectrum optimization of full-field digital mammography: Simulation and phantom study. *Medical Physics*, 33:4337, 2006.

[Boo02] John M. Boone. Normalized glandular dose (DgN) coefficients for arbitrary X-ray spectra in mammography: computer-fit values of Monte Carlo derived data. *Medical Physics*, 29(5):869–875, 2002.

[BPSM08] Tim Bray, Jean Paoli, C. Michael Sperberg-McQueen, Eve Maler, and François Yergeau. Extensible Markup Language (XML) 1.0 (Fifth Edition). World Wide Web Consortium, Recommendation REC-xml-20081126, November 2008.

[Bra03] Alberto Bravin. Exploiting the x-ray refraction contrast with an analyser: the state of the art. *Journal of Physics D: Applied Physics*, 36(10A):A24, 2003.

[Bre10] D. J. Brenner. Medical imaging in the 21st century – getting the best bang for the rad. *New England Journal of Medicine*, 362:943–945, 2010.

[Bri93] J. F. Briesmeister. MCNP–a general Monte Carlo n-particle transport code, version 4 A. Technical Report LA-12625, Los Alamos National Laboratory, Los Alamos, NM, 1993.

[BS89] K. F. Baverstock and J. W. Stather. *Low dose radiation: biological bases of risk assessment*. Taylor & Francis, 1989.

[Bur99] A. E. Burgess. The rose model, revisited. *Journal of the Optical Society of America A*, 16(3):633–646, 1999.

[CE98] O. Chubar and P. Elleaume. Accurate and efficient computation of synchrotron radiation in the near field region. *Proc. EPAC98*, pages 1177–1179, 1998.

[CGFD97] K. Cranley, B. Gilmore, G. Fogarty, and L. Desponds. Catalogue of diagnostic x-ray spectra and other data. *IPEM Report*, 78, 1997.

[CHK97] Dermott E. Cullen, John H. Hubbell, and Lynn Kissel. Epdl97: the evaluated photon data library, '97 version. *Accessed*, 1997.

[Cla04] J. A. Clarke. *The Science and Technology of Undulators and Wigglers*. Oxford Univ. Press, 2004.

[CMT03] Frank E. Carroll, Marcus H. Mendenhall, Robert H. Traeger, Charles Brau, and James W. Waters. Pulsed tunable monochromatic x-ray beams from a compact source: new opportunities. *Am. J. Roentgenol.*, 181(5):1197–202, 2003.

[Col09] Geant4 Collaboration. Geant4 user's guide for application developers, Dezember 2009. `http://geant4.web.cern.ch/geant4/UserDocumentation/UsersGuides/ForApplicationDeveloper/html/`.

[CTA11] E. Castelli, M. Tonutti, F. Arfelli, R. Longo, E. Quaia, L. Rigon, D. Sanabor, F. Zanconati, D. Dreossi, A. Abrami, E. Quai, P. Bregant, K. Casarin, V. Chenda, R. H. Menk, T. Rokvic, A. Vascotto, G. Tromba, and M. A. Cova. Mammography with synchrotron radiation: First clinical experience with phase-detection technique. *Radiology*, 259:684–694, Jun 2011.

[Dan98] George Dantzig. *Linear Programming and Extensions*. Princeton University Press, August 1998.

[DD84] D. R. Dance and G. J. Day. The computation of scatter in mammography by monte carlo methods. *Physics in Medicine and Biology*, 29(3):237, 1984.

[DD07] F. J. Dyson and D. Derbes. *Advanced Quantum Mechanics*. World Scientific, 2007.

[DDR04] Felix Diekmann, S. Diekmann, K. Richter, U. Bick, T. Fischer, R. Lawaczeck, W.-R. Press, K. Schön, H.-J. Weinmann, V. Arkadiev, A. Bjeoumikhov, N. Langhoff, J. Rabe, P. Roth, J. Tilgner, R. Wedell, M. Krumrey, U. Linke, G. Ulm, and B. Hamm. Near monochromatic x-rays for digital slot-scan mammography: initial findings. *Eur Radiol*, 14(9):1641–6, 2004.

[DEG92] W.-R. Dix, K. Engelke, W. Graeff, C. Hamm, J. Heuer, B. Kaempf, W. Kupper, M. Lohmann, B. Reime, and R. Reumann. Coronary angiography using synchrotron radiation studies in human subjects with the system NIKOS II. *Nuclear Instruments and Methods in Physics Research Section A: Accelerators, Spectrometers, Detectors and Associated Equipment*, 314(2):307 – 315, 1992.

[DHB05] D. R. Dance, R. A. Hunt, P. R. Bakic, A. D. A. Maidment, M. Sandborg, G. Ullman, and G. Alm Carlsson. Breast dosimetry using high-resolution voxel phantoms. *Radiation Protection Dosimetry*, 114(1-3):359–363, 17 May 2005.

[DPB99] P. Duvauchelle, G. Peix, and D. Babot. Effective atomic number in the Rayleigh to Compton scattering ratio. *Nuclear Instruments and Methods in Physics Research B*, 155:221–228, 1999.

[EGB07] T. Eichner, F. Grüner, S. Becker, M. Fuchs, D. Habs, R. Weingartner, U. Schramm, H. Backe, P. Kunz, and W. Lauth. Miniature magnetic devices for laser-based, table-top free-electron lasers. *Phys. Rev. ST Accel. Beams*, 10:082401, 2007.

[F04] J. Faure et al. A laser-plasma accelerator producing monoenergetic electron beams. *Nature*, 431:541–544, 2004.

[FE03] S. W. Fletcher and J. G. Elmore. Mammographic screening for breast cancer. *N. Engl. J. Med.*, 348:1672–1680, 2003.

[Fel68] William Feller. *An Introduction to Probability Theory and Its Applications, Vol. 1, 3rd Edition.* Wiley, 3rd edition, January 1968.

[FFR03] A Fassò, A Ferrari, S Roesler, J Ranft, P R Sala, G Battistoni, M Campanella, F Cerutti, L D Biaggi, E Gadioli, M V Garzelli, F Ballarini, A Ottolenghi, D A Scannicchio, M Carboni, M Pelliccioni, R Villari, V Andersen, A Empl, K Lee, L Pinsky, T N Wilson, and N Zapp. The fluka code: present applications and future developments. Technical Report physics/0306162, Milano Univ. INFN, Milano, Jun 2003.

[FSB10] Jacques Ferlay, Hai-Rim Shin, Freddie Bray, David Forman, Colin Mathers, and Donald M. Parkin. Estimates of worldwide burden of cancer in 2008: GLOBOCAN 2008. *Int. J. Cancer*, 127(12):2893–2917, December 2010.

[FWP09] M. Fuchs, R. Weingartner, A. Popp, Zs. Major, S. Becker, J. Osterhoff, I. Cortrie, B. Zeitler, R. Hörlein, G. D. Tsakiris, U. Schramm, T. P. Rowlands-Rees, S. M. Hooker, D. Habs, F. Krausz, S. Karsch, and F. Grüner. Laser-driven soft-x-ray undulator source. *Nature Physics*, 5, 2009.

[G04] C. G. R. Geddes et al. High quality electron beams form a laser wakefield accelerator using plasma-channel guiding. *Nature*, 431:538–541, 2004.

[GBS07] F. Grüner, S. Becker, U. Schramm, T. Eichner, M. Fuchs, R. Weingartner, D. Habs, J. Meyer-Ter-Vehn, M. Geissler, M. Ferrario, L. Serafini, B. van der Geer, H. Backe, W. Lauth, and S. Reiche. Design considerations for table-top, laser-based VUV and X-ray free electron lasers. *Applied Physics B*, 86(3):431–435, February 2007.

[GE] GE Measurement & Control Solutions. *vtomex-s Brochure*. `http://www.ge-mcs.com/download/x-ray/phoenix-x-ray/GEIT-31204EN\_vtomex-s.pdf`.

[GHN01] W. M. Gibson, H. Huang, J. Nicolich, P. Klein, and C. A. MacDonald. Polycapillary optics for angular filtering of x rays in two dimensions. *Advances in X-ray analysis, volume 45: proceedings of the 50th Annual Conference on Applications of X-ray Analysis (Denver X-ray Conference)*, 2001.

[Gia96] J. C. Giacomini. K-edge subtraction angiography with synchrotron x-rays. Technical Report INIS-US-0173, Int. At. Energy Agency, Wien, Dec 1996.

[GP91] A. Galindo and P. Pascual. *Quantum mechanics II*. Quantum Mechanics. Springer-Verlag, 1991.

[H08] N. A. M. Hafz et al. Stable generation of gev-class electron beams from self-guided laser-plasma channels. *Nature Photon.*, 2:571–577, 2008.

[HFBD00] Christoph Hoeschen, Andreas Fessel, Egbert Buhr, and Wilfried Döhring. Determination of the x-ray intensity pattern in mammography with very high-spatial resolution. volume 3977, pages 220–230. SPIE, 2000.

[HFZ05] C. Hoeschen, U. Fill, M. Zankl, W. Panzer, D. Regulla, and W. Döhring. A high-resolution voxel phantom of the breast for dose calculations in mammography. *Radiation Protection Dosimetry*, 114:406–409, 2005.

[HOD10] J. F. Hainfeld, M. J. O'connor, F. A. Dilmanian, D. N. Slatkin, D. J. Adams, and H. M. Smilowitz. Micro-ct enables microlocalisation and quantification of her2-targeted gold nanoparticles within tumour regions. *The British journal of radiology*, 2010 Nov 16 2010.

[Hoe02] Christoph Hoeschen. *Das reale Strahlenbild bei einer Röntgenthoraxaufnahme*, volume 67 of *PTB-Berichte. Optik.* N. W. Verlag für neue Wissenschaft, 2002.

[HRS11] Christoph Hoeschen, Dieter Regulla, Helmut Schlattl, Nina Petoussi-Henss, Wei Bo Li, and Maria Zankl. How do we measure dose and estimate risk? *Proceedings of SPIE*, 7961, 2011.

[ICR77] ICRP: International Commission on Radiological Protection. *Recommendations of the International Commission on Radiological Protection*, volume 26 of *ICRP publication.* Pergamon Press, 1977.

[ICR88] ICRU: International Commission on Radiation Units and Measurements and International Commission on Radiological Units and Measurements. *ICRU report.* Number Bd. 44 in ICRU Report. International Commission on Radioation Units and Measurements, 1988.

[ICR95] ICRU: International Commission on Radiation Units and Measurements. *Medical Imaging–the Assessment of Image Quality.* ICRU Report. International Commission on Radiation Units and Measurements, 1995.

[ICR07] ICRP: International Commission on Radiological Protection. *Recommendations of the International Commission on Radiological Protection*, volume 103 of *ICRP publication.* Pergamon Press, 2007.

[IME12] IMETUM. Institute of Medical Engineering, Technische Universität München, 2012.
`http://www.imetum.tum.de/`.

[Jac75] J. D. Jackson. *Classical electrodynamics.* J.Wiley and sons, New York, 1975.

[JY83] P. C. Johns and M. J. Yaffe. Coherent scatter in diagnostic radiology. *Medical Physics*, 10(1):40–50, 1983.

[KCS94] K.-J. Kim, S. Chattopadhyay, and C.V. Shank. Generation of femtosecond x-rays by 90° thomson scattering. *Nuclear Instruments and Methods in Physics Research Section A: Accelerators, Spectrometers, Detectors and Associated Equipment*, 341(1-3):351 – 354, 1994.

[KR03] I. Kawrakow and D. W. O. Rogers. The egsnrc code system : Monte carlo simulation of electron and photon transport. *System*, (PIRS-701):2001–2003, 2003.

[KW08] M. H. Kalos and P. A. Whitlock. *Monte Carlo Methods*. Wiley, 2008.

[LADK05] Rüdiger Lawaczeck, Vladimir Arkadiev, Felix Diekmann, and Michael Krumrey. Monochromatic x-rays in digital mammography. *Invest Radiol*, 40(1):33–9, 2005.

[LDS96] Ewing Lusk, Nathan Doss, and Anthony Skjellum. A high-performance, portable implementation of the mpi message passing interface standard. *Parallel Computing*, 22:789–828, 1996.

[LNG06] W. P. Leemans, B. Nagler, A. J. Gonsalves, Cs Toth, K. Nakamura, C. G. R. Geddes, E. Esarey, C. B. Schroeder, and S. M. Hooker. GeV electron beams from a centimetre-scale accelerator. *Nature Physics*, 2(10):696–699, September 2006.

[M04] S. P. D. Mangles et al. Monoenergetic beams of relativistic electrons from intense laser plasma interactions. *Nature*, 431:535–538, 2004.

[MB99] Kyoko Makino and Martin Berz. Cosy infinity version 8. *Nuclear Instruments and Methods in Physics Research A*, 427:338–343, 1999.

[MB02] Gregory A. Mohr and Clifford Bueno. GE a-Si flat panel detector performance in industrial digital radiography. European Conference on Nondestructive Testing, June 2002.

[Mes94] Message Passing Forum. MPI: A Message-Passing Interface Standard. Technical report, Knoxville, TN, USA, 1994.

[MGMH69] W. H. McMaster, N. Kerr-Del Grande, J. H. Mallett, and J. H. Hubbell. *Compilation of X-ray Cross Sections. Lawrence Radiation Laboratory Report UCRL-50174*. National Bureau of Standards, Springfield, VA, 1969.

[Mor78] Jorge Moré. The levenberg-marquardt algorithm: Implementation and theory. In G. Watson, editor, *Numerical Analysis*, volume 630 of *Lecture Notes in Mathematics*, pages 105–116. Springer Berlin / Heidelberg, 1978.

[MR94] K. Mabuchi and E. Ron. *Cancer Incidence in Atomic Bomb Survivors*, volume 137 of *Radiation research*. 1994.

[MSGH11] Bernhard H. Müller, Helmut Schlattl, Florian Grüner, and Christoph Hoeschen. A laser-driven undulator x-ray source: simulation of image formation and dose deposition in mammography. *Proceedings of SPIE*, 7961(6), 2011.

[MVF00] R. Moeckli, F. R. Verdun, S. Fiedler, M. Pachoud, P. Schnyder, and J. F. Valley. Objective comparison of image quality and dose between conventional and synchrotron radiation mammography. *Phys. Med. Biol.*, 45:3509–3523, 2000.

[MVF03] R. Moeckli, F. R. Verdun, S. Fiedler, M. Pachoud, S. Bulling, P. Schnyder, and J. F. Valley. Influence of scatter reduction method and monochromatic beams on image quality and dose in mammography. *Med. Phys.*, 30:3156–3164, 2003.

[MYS11] Angela B. Mariotto, K. Robin Yabroff, Yongwu Shao, Eric J. Feuer, and Martin L. Brown. Projections of the cost of cancer care in the united states: 2010-2020. *J Natl Cancer Inst*, 103(2):117–28, 2011.

[ŌE03] H. Ōnuki and P. Elleaume. *Undulators, Wigglers and Their Applications*. Taylor & Francis, 2003.

[OGS09] P. Oliva, P. Golosio, S. Stumbo, A. Bravin, and P. Tomassini. Compact x-ray sources for mammographic applications: Monte carlo simulations of image quality. *Med. Phys.*, 36:5149, 2009.

[OMR10] F. H. O'Shea, G. Marcus, J. B. Rosenzweig, M. Scheer, J. Bahrdt, R. Weingartner, A. Gaupp2, and F. Grüner. Short period, high field cryogenic undulator for extreme performance x-ray free electron lasers. *Phys. Rev. ST Accel. Beams*, 13:070702, 2010.

[OPM08] J. Osterhoff, A. Popp, Zs. Major, B. Marx, T. P. Rowlands-Rees, M. Fuchs, M. Geissler, R. Hörlein, B. Hidding, S. Becker, E. A. Peralta, U. Schramm, F. Grüner, D. Habs, F. Krausz, S. M. Hooker, and S. Karsch. Generation of stable, low-divergence electron beams by laser-wakefield acceleration in a steady-state-flow gas cell. *Phys. Rev. Lett.*, 101:085002, 2008.

[Pas03] O. Pasche. Über eine neue Blendvorrichtung in der Röntgentechnik. *Deutsche Med. Wochenschr.*, 29:266,267, 1903.

[Per91] S. T. Perkins. *Tables and Graphs of Electron-interaction Cross Sections from 10 EV to 100 GeV Derived from the LLNL Evaluated Electron Data*

Library (EEDL), Z. Lawrence Livermore National Laboratory, University of California, 1991.

[PGH05] E. D. Pisano, C. Gatsonis, E. Hendrick, M. Yaffe, J. K. Baum, S. Acharyya, E. F. Conant, L. L. Fajardo, L. Basset, C. D'Orsi, R. Jong, and M. Rebner. Diagnostic performance of digital versus film mammography for breast-cancer screening. *New England Journal of Medicine*, 353:1773–1783, 2005.

[PH01] N. Peinsipp and O. Hinrichs. *Verordnung über den Schutz vor Schäden durch Röntgenstrahlen (Röntgenverordnung RöV) vom 8. Januar 1987.: Textausgabe mit amtlicher Begründung und Erläuterungen.* Praxis Technikrecht. Forkel, 2001.

[PMtV02] A. Pukhov and J. Meyer-ter Vehn. Laser wake field acceleration: The highly non-linear broken-wave regime. *Appl. Phys. B: Lasers Opt.*, 74:355–361, 2002.

[PW09] A. H. Partridge and E. P. Winer. On mammography – more agreement than disagreement. *New England Journal of Medicine*, 361:2499–2501, 2009.

[PYK03] E. D. Pisano, M. J. Yaffe, and C. M. Kuzmiak. *Digital Mammography.* LWW medical book collection. Lippincott Williams & Wilkins, 2003.

[SA01] F. Salvat and Nuclear Energy Agency. *Penelope: A Code System for Monte Carlo Simulation of Electron and Photon Transport.* Data bank. OECD Nuclear Energy Agency, 2001.

[SBD04] Valentin A. Stezhko, Elena E. Buglova, Larissa I. Danilova, Valentina M. Drozd, Nikolaj A. Krysenko, Nadia R. Lesnikova, Victor F. Minenko, Vladislav A. Ostapenko, Sergey V. Petrenko, Olga N. Polyanskaya, Valery A. Rzheutski, Mykola D. Tronko, Olga O. Bobylyova, Tetyana I. Bogdanova, Ovsiy V. Ephstein, Iryna A. Kairo, Olexander V. Kostin, Ilya A. Likhtarev, Valentin V. Markov, Valery A. Oliynik, Viktor M. Shpak, Valeriy P. Tereshchenko, Galina A. Zamotayeva, Gilbert W. Beebe, Andre C. Bouville, Aaron B. Brill, John D. Burch, Daniel J. Fink, Ellen Greenebaum, Geoffrey R. Howe, Nickolas K. Luckyanov, Ihor J. Masnyk, Robert J. McConnell, Jacob Robbins, Terry L. Thomas, Paul G. Voillequeo, and Lydia B. Zablotskak. A Cohort Study of Thyroid Cancer and Other Thyroid Diseases after the Chornobyl Accident: Objectives, Design and Methods. *Radiation Research*, 161:481–492, 2004.

[SH10] F. H. Schöfer and C. Hoeschen. Exact calculation of the minimal exposure for the secure detection of a transmission contrast signal. *Radiation Protection Dosimetry*, 139(1-3):81–85, 2010.

[SK98] C. Schulze and U. Kleuker. A bent laue analyser crystal for rayleigh-to-compton computed tomography. *J. Synchrotron Radiat.*, 5(Pt 3):1085–7, 1998.

[Sol24] Walter Soller. A new precision x-ray spectrometer. *Phys. Rev.*, 24:158–167, Aug 1924.

[SRE12] Caroline A. Schneider, Wayne S. Rasband, and Kevin W Eliceiri. NIH Image to ImageJ: 25 years of image analysis. *Nat. Meth.*, 9:671–675, 2012.

[SSA92] T. Sugahara, L.A. Sagan, and T. Aoyama. *Low dose irradiation and biological defense mechanisms: proceedings of the International Conference on Low Dose Irradiation and Biological Defense Mechanisms, Kyoto, Japan, 12-16 July 1992*. International congress series. Excerpta Medica, 1992.

[STEF92] P. Sprangle, A. Ting, E. Esarey, and A. Fisher. Tunable, short pulse hard x-rays from a compact laser synchrotron source. *Journal of Applied Physics*, 72(11):5032–5038, 1992.

[STH10] L. M. Surhone, M. T. Tennoe, and S. F. Henssonow. *Clhep*. VDM Publishing, 2010.

[Str00] Bjarne Stroustrup. *The C++ Programming Language*. Addison-Wesley Longman Publishing Co., Inc., Boston, MA, USA, 3rd edition, 2000.

[TD79] T. Tajima and J. M. Dawson. Laser electron accelerator. *Phys. Rev. Lett.*, 43:267–270, Jul 1979.

[TH03] W. Thirring and E. M. Harrell. *Classical Mathematical Physics: Dynamical Systems and Field Theories*. Springer, 2003.

[Tur08] J. E. Turner. *Atoms, Radiation, and Radiation Protection*. Physics textbook. John Wiley & Sons, 2008.

[vdGdL98] S. B. van der Geer and M. J. de Loos. General Particle Tracer: A 3D code for accelerator and beamline design. *Proc. EPAC98*, page 1245, 1998.

[Wei96] S. Weinberg. *The Quantum Theory of Fields*. Number Bd. 1. Cambridge University Press, 1996.

[Wel10] H. G. Welch. Screening mammography – a long run for a short slide? *N. Engl. J. Med.*, 363:1276–1278, 2010.

[WHO08] WHO. The global burden of disease: 2004 update, 2008. `http://www.who.int/healthinfo/global\_burden\_disease/2004\_report\_update/en/index.html`.

[Wil96] K. Wille. *Physik der Teilchenbeschleuniger und Synchrotronstrahlungsquellen: Eine Einführung.* Teubner, 1996.

[WKE06] B. F. Wall, G. M. Kendall, A. A. Edwards, S. Bouffler, C. R. Muirhead, and J. R. Meara. What are the risks from medical X-rays and other low dose radiation? *Br J Radiol*, 79(940):285–294, April 2006.

[YBK81] Michael V. Yester, Gary T. Barnes, and Michael A. King. Experimental measurements of the scatter reduction obtained in mammography with a scanning multiple slit assembly. *Medical Physics*, 8(2):158–162, 1981.

[YBP09] M. J. Yaffe, J. M. Boone, N. Packard, O. Alonzo-Proulx, S. Y. Huang, C. L. Peressotti, A. Al-Mayah, and K. Brock. The myth of the 50-50 breast. *Medical Physics*, 36(12):5437, 2009.

[YM11] Martin J. Yaffe and James G. Mainprize. Risk of radiation-induced breast cancer from mammographic screening. *Radiology*, 258(1):98–105, 2011.

[YT12] Tetsuya Yuasa and Tohoru Takeda. *Fluorescent X-Ray Computed Tomography Using Synchrotron Radiation Towards Molecular Imaging, Molecular Imaging.* InTech, 2012.

Acknowledgments

It would not have been possible for me to complete this work without the support of many people some of whom I want to thank here:

- Prof. Dr. Florian Grüner for giving me the opportunity to work in an interesting field of research, for always creating a good atmosphere in his group, for stimulating new ideas and for his continuing support.
- Prof. Dr. Christoph Hoeschen for his scientific guidance for the fruitful discussions and for always opening up new collaborations.
- Dr. Helmut Schlattl for many helpful discussions and for helping with all kinds of problems.
- The whole Department of Medical Radiation Physics and Diagnostics at the HMGU for providing an environment that is both productive and pleasurable.
- The FEL group at the Ludwig–Maximilians–Universität for their initial support and for the welcoming experience whenever I visited them.
- Prof. Dr. Franz Pfeiffer and especially Dr. Julia Herzen for extensively offering me the opportunity to scan our breast specimens in their CT system at the Institute of Medical Engineering of the Technical University of Munich.
- Jared Moore Ph.D. and Prof. Harrisson Barrett for the opportunity to scan our breast specimens with their adaptive CT system at the Arizona university radiology department and for my short but interesting visit there.
- Sebastian Rothlauf and Rainer Ruder of the mathematical physics group at the university of Erlangen–Nürnberg for their "lovely" postcards.
- Annemarie Holleczek for commuting between Oxford and Munich and for the low frequency of mole attacks in the final stages of this work.
- My family for the moral support and much more.